The development of Compton imaging techniques for the GammaKEV project using the AGATA A006 detector

Thesis submitted in accordance with the requirements of the
University of Liverpool for the degree of
Doctor in Philosophy

by

Michael John Slee

Oliver Lodge Laboratory

October 2012

Acknowledgements

This is the part of my thesis everyone has been looking forward to, so I'd like to take this opportunity to thank everyone who has made this journey possible and worked with me over my time as a PhD student at the University of Liverpool.

Firstly I would like to thank Dr Andy Boston, Prof Paul Nolan and BAE Systems for providing me with this fantastic opportunity to study within the Nuclear Physics group. I would especially like to thank Dr Andy Boston for his guidance and patience proof reading large chunks of my thesis and Dr Helen Boston for her support in the lab.

I would also like to thank all of the support staff within the department especially Dr John Cresswell for fixing numerous computing issues.

A special mention needs to go Dr Dan Judson who over the past couple of years has kept me on the straight and narrow. We've spent many an hour in the lab together, spent a week in Barrow together and spent 48 hours in a car going to Cologne and back without killing each other. Without him my time at the department would have been dull and uneventful.

I would like to thank students past and present for keeping me amused and any help they've given me. Particular mention should go to Fay who has dragged me out to the pub and listened to me whine about my PhD and vice versa. I'd also like to thank Rob for splitting the rent with me and also listening to me talk about how my work is going all the time when he's probably not really bothered.
Thank you also to Laura, Jamie, Sam, Martin, Anthony, Heidi, Jon R, Liam, Dave O and anyone else who thinks they deserve a special mention. To you guys and gals thank you for being there over the past couple of years and making the experience even better with trips to UnI and the pub.

Most importantly I would like to thank my family and Shona for always being there without question when I have needed them and for their continual support.

Thank you one and all for your support I couldn't have done it without you, cheers.

Abstract

This thesis presents the methods and results different position analysis techniques provide for Compton image reconstruction. The AGATA A006 detector a highly segmented large volume detector has been utilised for the analysis of data presented in this thesis.

This data contained within the thesis was part of the GammaKEV project, which aimed to develop a portable gamma-ray spectrometer for use on a nuclear submarine, with this work focusing on how the improvement of position determination can improve the reconstructed image FWHM. The AGATA A006 detector is a 80x80x90 mm^3 HPGe, 36 segment and one core, coaxial detector. The average energy resolution over all the segments and core was found to be 2.7 keV. This work shows the improvement that parametric pulse shape analysis can make in large detector segments to Compton image reconstruction.

Two 1332 keV ^{60}Co sources have been placed in front of the AGATA A006 detector at 100 mm and have been imaged using a simple back projection Compton image reconstruction code developed at the University of Liverpool. A method has been developed to apply parametric PSA to improve the precision of locating the position of interaction within the segments.

A GEANT4 simulation has been adapted to replicate the experimental setup utilising a Gaussian smearing function applied to the simulated x, y and z position and energy data to assess the improvement that parametric PSA provides to the discrimination of position within the detector segments.

The simulated energy and position smeared data reconstructed image resolution has been compared to the experimental data reconstructed image resolution. It has been found that the parametric PSA method developed in this thesis, will give a position resolution of 3 ± 0.5 mm within the segments of the crystal when compared to a 15 ± 0.5 mm position resolution for data reconstructed without utilising parametric PSA.

Contents

List of Figures

List of Tables

Chapter 1

Introduction

The work presented in this thesis is part of the GammaKEV project. This project is to develop a portable detector to locate and identify sources of gamma radiation for use on-board a nuclear submarine. The requirement is to cover an energy range of 60 keV to 10 MeV [1]. The subject of this work is to discuss and develop the precision of current Compton imaging techniques. This developmental work will be carried out utilising the AGATA A006 detector. This AGATA detector will provide position and energy information that will be used in the discussion for the development of Compton imaging techniques for this project. The accuracy and improvement of parametric pulse shape analysis (PSA) on Compton image reconstruction has been investigated in this thesis.

1.1 The GammaKEV project

This project requires a gamma radiation sensor capable of imaging the gamma radiation field associated with gamma radiation from the reactor, from fission products and gammas arising from neutron scattering activation. This is due to health and safety reasons, for a better understanding of the condition of the on-board reactor [1]. This project aims to utilise the Compton camera technique and a major part of this thesis is determining the performance and limitations of this method.

1.2 The AGATA project

This work has utilised an AGATA detector. The AGATA project is the next generation of high resolution gamma spectroscopy arrays, the aim of which is to improve the photopeak efficiency to around 40% compared to previous arrays. To achieve this efficiency the AGATA array is assambled with a 4π confinguration around the target, giving the advantage of using a larger detection solid angle and also removing the bismuth germinate (BGO) suppression shield. Removing the Bismuth Germinate suppression shield stops Compton scattered events being vetoed but instead are reconstructed by utilising gamma-ray tracking increasing the efficiency of the detector. The AGATA A006 detector is HPGe detector manufactured by Canberra, it is electrically segmented into 36 segements, 6 azimuthal and 6 through depth with one core segment. The crystal has the overall dimensions of 100 mm in length and 80 mm in diameter.

1.3 Compton imaging technique

The Compton imaging technique relies on a minimum of two gamma-ray interactions that need to be measured with excellent energy and position resolution. The first interaction is a Compton scatter event from an electron in the detection material. It will then be scattered into an absorber material where the second interaction will undergo photoelectric absorbtion. Compton kinematics, using the positions of interaction and energy deposited, are then used to reconstruct the gamma ray paths. The sensitivity of this system will be much greater than physically collimated systems, increasing the efficiency of the process and reducing the collection time [2].

1.4 Research aims

- Assess the limitations of a Compton camera setup
- Develop algorithms to enable more precise information about the position of

interaction

- Utilise the algorithms developed
- Utilise a Compton image reconstruction code to assess the improvement of the developed algorithms.
- Predict the experimental imaging performance through simulation.

Chapter 2

Radiation detection

2.1 Gamma radiation

The emission of gamma radiation is caused by excited nuclei decaying to lower-lying levels. The excited states typiclly de-excite in the order of picoseconds or less. During de-excitation, a gamma-ray photon is emitted with energy equal to the difference in energy between the initial and final nuclear states. The gamma rays appear with a half-life characteristic of the parent nuclide but with the energy level structure of the daughter nuclide. If an example of the decay of ^{60}Co is taken, these gamma rays decay with a half-life of 5.26 years but gamma-ray transistions are observed from the daughter ^{60}Ni nucleus [3].

2.2 Interaction of gamma radiation

A fundamental requirement for the detection of radiation is the production of secondary charged particles which are collected to produce an electrical signal. Gamma radiation is uncharged, unlike alpha and beta radiation, so to produce a secondary electron the gamma ray must transfer energy to an electron within the detector material. The energy of the electron is proportional to the energy of the gamma ray enabling spectroscopic information to be gathered. Gamma radiation can interact

with the detector material through several mechanisms, interactions such as Rayleigh scattering and Thompson scattering are possible. The most likely interactions within the energy range of $\approx$ 10keV to a few MeV are photoelectric absorption, Compton scattering and pair production [3]. Each of these contribute to the total linear attenuation coefficient for gamma rays, as shown in Equation 2.1

$$\mu_t = \mu_{pe} + \mu_{cs} + \mu_{pp} \tag{2.1}$$

where μ_{pe}, μ_{cs} and μ_{pp} are defined as the attenuation coefficient for photoelectric absorption, compton scattering and pair production, respectively. Equation 2.1 represents the total probability that a gamma ray is absorbed through the contributions of the interaction mechanisms. The intensity I of a collimated mono energetic gamma-ray beam after travelling a distance z through an absorbing medium can be related to the linear attenuation coefficient by:

$$I = I_0 e^{-\mu_t z} \tag{2.2}$$

where I_0 is the intensity of the gamma-ray beam before it enters the absorbing material.

The probability of a photoelectric absorption, Compton scattering or pair production interaction occurring is dependent upon the atomic number Z of the absorbing material and the energy of the incident gamma ray E_γ. This is shown in Figure 2.1.

2.2.1 Photoelectric absorption

Photoelectric absorption occurs when a gamma-ray photon interacts with a bound electron in an atom. This is normally a K-shell electron of the detector material, with the photon completely disappearing. A photo-electron is ejected from this interaction with an energy of:

$$E_e = E_\gamma - E_b \tag{2.3}$$

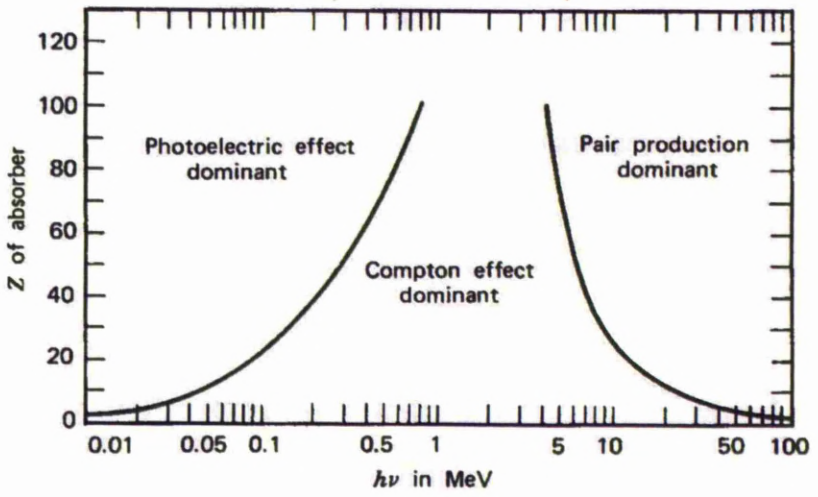

Figure 2.1: Figure showing the relative probabilities of a particular gamma ray interaction occurring as a function of absorber number Z and gamma-ray energy $E_\gamma = h\nu$ [3]

where E_e is the energy of the electron, E_γ is the energy of the incoming gamma-ray photon and E_b is the binding energy of the photoelectron in its original shell.

The atom is now left in an ionised state, this excitation energy is transferred to leave the atom in equilibrium. Either the excitation energy is redistributed between the remaining electrons in the atom, which can lead to the emission of an Auger electron or alternatively X-ray flouresence can occur where an electron from a higher valency fills the shell of the ejected electron resulting in the emission of a characteristic X ray. Photoelectric absorption is the dominant interaction process at low energies and high atomic Z number. It is not possible to define a single function to describe the cross section for photoelectric absorption over all energies as a function of atomic number. As an approximation, the value of probabiltiy for photoelectric absorption per atom over all ranges of E_γ and atomic number Z is given by:

$$prob_{pa} \propto \frac{Z^n}{E_\gamma^{3.5}} \tag{2.4}$$

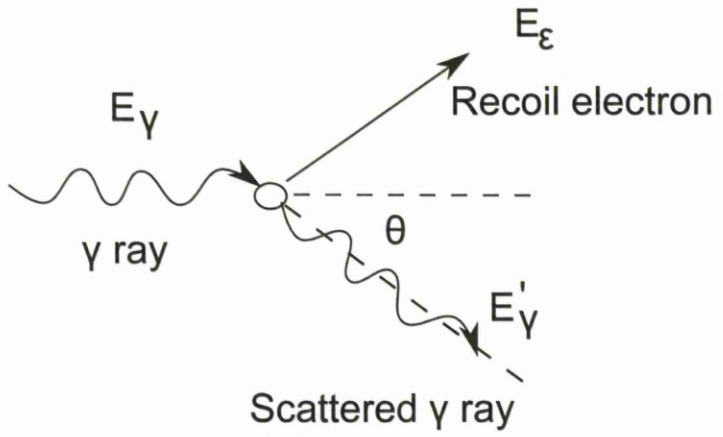

Figure 2.2: Figure showing the process of Compton scattering [3].

where n is in the range of 4 to 5.

2.2.2 Compton scattering

The work contained within this thesis relies on Compton scattering interactions. During a Compton scatter interaction a gamma ray transfers a fraction of its energy to a weakly bound electron in the atom. This results in the deflection of the gamma ray from its incident path, by the scattering angle θ, and the transfer of energy to the electron. The fraction of energy carried away by the scattered gamma ray [4], E'_γ, is given by Equation 2.5.

$$E'_\gamma = \frac{E_\gamma}{1 + \frac{E_\gamma}{m_0c^2}(1 - cos\theta)} \tag{2.5}$$

where m_0c^2 is equal to 0.511MeV, the rest mass of an electron.

The scattering angle θ varies between 0° and 180° resulting in a distribution of energies for E'_γ. The maximum energy transferred by the incident gamma ray to the electron occurs at an angle of 180° with a minimum at 0°.

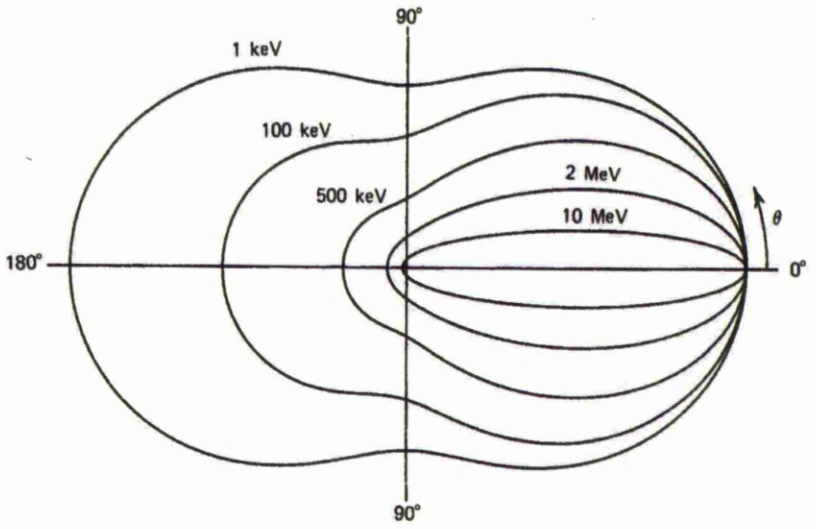

Figure 2.3: Polar plot showing the Compton scattering cross section against deflection angle for a range of initial gamma-ray energies.

The probability of a gamma ray undergoing Compton scattering increases linearly as a function of Z as the increasing atomic number increases the number of scattering targets. The angular distribution of the scattering of incident gamma rays on a given detector material is defined by the Klein-Nishina formula as shown in Equation 2.6.

$$\frac{d\sigma}{d\Omega} = Zr_0^2 \left(\frac{1}{1+\alpha\,(1-cos\theta)} \right)^2 \left(\frac{1+cos^2\theta}{2} \right) \left(1 + \frac{\alpha^2\,(1-cos\theta)^2}{(1+cos^2\theta)\,[1+\alpha\,(1-cos\theta)]} \right) \tag{2.6}$$

where r_o is the electron radius and $\alpha \equiv E_\gamma / m_0 c^2$

Figure 2.3 is a polar plot of Compton scattering cross section against deflection angle for a defined range of gamma-ray energies in germanium. At incident energies of over 500keV forward focused scattering is highly probable.

2.2.3 Pair production

When a gamma ray interacts via the pair production process, it disappears within the Coulomb field of the nucleus and is replaced by an electron-positron pair. This interaction mechanism is therefore only energetically possible if the incident gamma-ray energy exceeds 1.022 MeV, twice the rest mass of the electron, which is required to create the electron-positron pair. Any additional energy is transferred as kinetic energy to the two outgoing particles and nucleus recoil energy. The positron will thermalise over a short distance in the material until it annihilates with an electron in the medium. Two annihilation gamma rays with energy 511 keV are subsequently emitted 180° from each other. These gamma rays may be absorbed in the material, although it is possible that one or both may escape, resulting in escape peak features in gamma-ray spectra [5].

2.3 Gamma-ray detectors

To maximise the detection efficiency the use of a solid state material in gamma-ray detectors is highly favourable, as these materials have densities up to a thousand times greater than the equivalent gas-filled detectors, thus enabling detector dimensions to be kept much smaller.
Scintillation materials such as sodium iodide(NaI) and bismuth germinate(BGO) had widespread applications within nuclear physics research for many years providing high stopping power for incident gamma rays. A major limitation was their poor energy resolution due to the inefficient steps involved generating a proportional electric signal from an incident gamma ray.
The steps required for scintillation are as follows:

1. A gamma ray interacting in a scintillation detector excites the scintillation detection material causing fluorescence, a prompt emission of visible radiation. Scintillations are minute flashes of light produced by certain materials when they absorb radiation.

2. The light photon is converted to an electron by passing through a photoemissive material located at the entrance of a photomultiplier tube.

3. Figure 2.4 shows the electrons are accelerated between dynodes, releasing secondary electrons.

4. This results in a measurable signal proportional to the incident photon energy.

However there are uncertainties in the electron multiplication process in the photomultiplier tube and non - linearity in the light yield. The energy required to produce an information carrier is of the order of 100 eV or more, meaning that the number of charge carriers are no more than a few thousand per interaction.
Due to the low statistics it is difficult to improve the energy resolution. However, semiconductor materials are able to produce many more charge carriers per interaction, thus resulting in the improvement of the energy resolution [6] [5].

2.4 Semiconductor detectors

In the early 1960s the development of semiconductor technology and fabrication led to the widespread use and availability of semiconductor detectors for gamma-ray spectroscopy, providing improved energy resolution [3].
Semiconductor detectors are more efficient in generating a proportional electric signal from an incident gamma ray, due to a reduced number of steps to produce information carriers.
When a gamma ray transfers energy to an atomic electron through one of the interaction mechanisms mentioned in the previous section, electron-hole pairs are created along the subsequent path of the atomic electron through the detector. A potential difference is applied to the detector, which produces an electric field that causes the electron-hole pairs to be swept from the active volume to the contacts, where the electrical signal is then read out [7] [5].

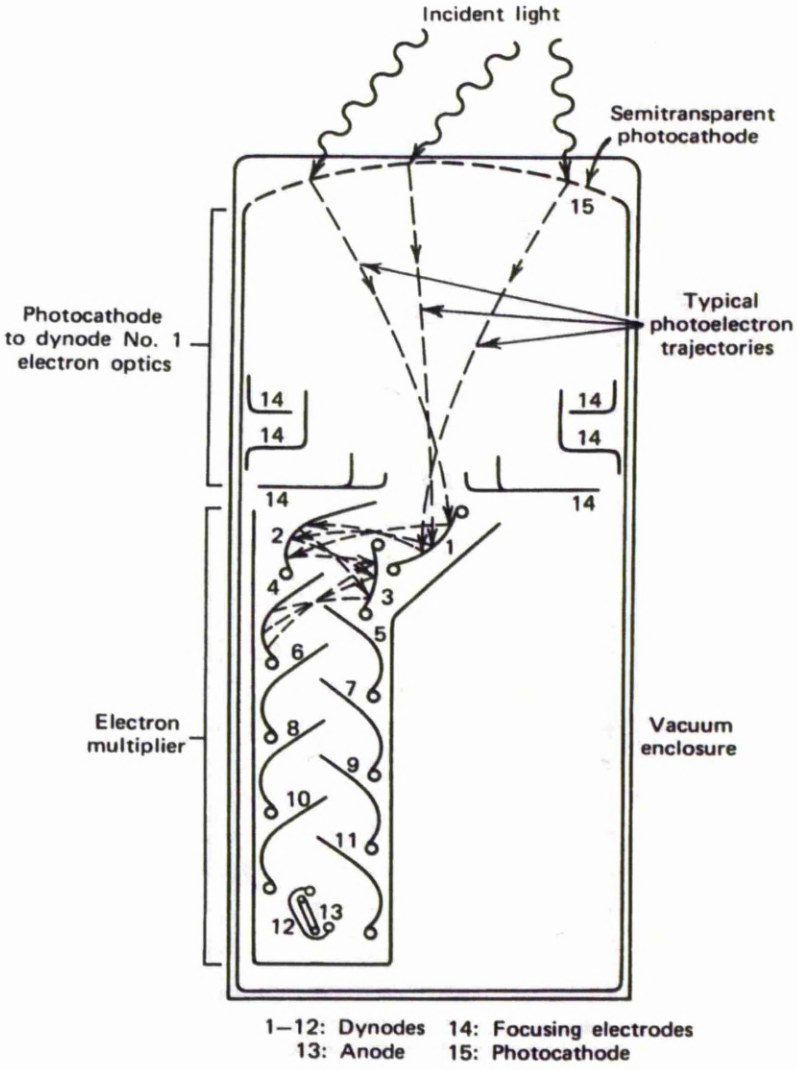

Figure 2.4: Figure showing the operation of a photomultiplier tube, the electrons are accelerated between dynodes, releasing secondary electrons [6]

2.4.1 Charge carrier generation

Following a gamma-ray interaction, a large number of excitations and ionisations take place as the electron comes to rest in the detector, this mechanism occurs over a small volume in the detector and is known as a charge cloud. For 1332 keV gamma rays the average path length of electrons in germanium is $\approx$ 4mm.

$$N = \frac{E_\gamma}{E_{pair}} \tag{2.7}$$

The number of electron-hole pairs N that are created in the charge cloud is dependent on the energy of the incident gamma ray, E_γ and the ionisation energy E_{pair} of the absorber material, for Ge $E_{pair} = 2.76$ eV. The excitation of each valence electron into the conduction band results in a net positive charge, or hole, in the valence band. The electron and hole diffuse away from their initial sites as a function of time and will eventually recombine. However, under the application of a potential difference, which produces an electric field ϵ, the electrons and holes will migrate in opposite directions, parallel to the direction of the electric field.

Each hole acts as a point positive charge and the holes move in the same direction as the electric field. The net average drift velocity with which the charges move varies for different materials according to the mobility μ for holes and electrons.

The drift velocity increases proportionally as the electric field strength is increased until saturation occurs, typically of the order of 10^7 cm/s.

Above this electric field strength, the drift velocity is independent of the electric field strength. Semiconductor detectors are typically operated so that saturation velocity is achieved.

If it is assumed that the creation of individual electron-hole pairs obeys Poisson statistics, it can be shown that the associated uncertainty in N_{pair} should simply vary as $\sqrt{N_{pair}}$. The creation of one carrier pair is not independent of the next, however, so a correction factor must be introduced to relate the observed variance to the theoretical variance described by Poisson statistics. This factor is known as the Fano factor and is calculated empirically as the ratio of the observed variance in N_{pair} and the Poisson

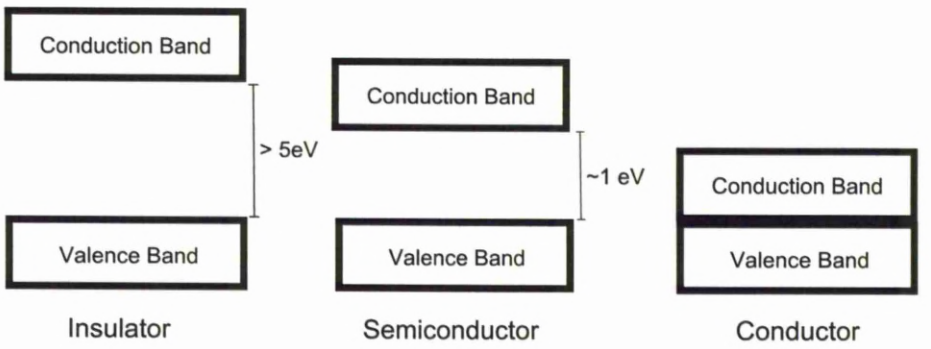

Figure 2.5: Figure showing the band gaps in semiconductor materials

- predicted variance [7].

2.4.2 Semiconductor properties

The band structure defines the electrical properties of the material classifying it either as an insulator, conductor or a semiconductor [3]. These band gaps can be seen in Figure 2.5.

In a conducting material the conduction band is either partially filled or the valence band and conduction band overlap. The lack of a band gap (region of non-allowed electron energies) allows electrons from the valence band to move up into the conduction band with only a small gain in kinetic energy. In a conducting material this kinetic energy is typically provided by an applied electric field and facilitates current flow. In contrast, an insulating material exhibits a large band gap which is larger than the thermal energy of an electron. As a result, even in the presence of an applied electric field, valence electrons may not be promoted into the conduction band and current will not flow.

Semiconductor materials may be considered to be the intermediate case where the band gap is extremely small (typically around 1eV) and thermal excitation of valence electrons can result in promotion to the conduction band. At low temperatures semiconductor materials act as insulators, but at room temperature and above the

thermal energy is an appreciable fraction of the band gap energy resulting in a significant number of electrons being promoted to the conduction band, the probability of this is given by Equation 2.8 [7] [8] [9].

$$p(T) = CT^{\frac{3}{2}} exp(-\frac{E_g}{2kT}) \tag{2.8}$$

where T is the absolute temperature, E_g is the band gap energy, k is the Boltzmann constant and C is the proportionality constant characteristic of the material. The application of a small applied potential results in current flow.

2.4.3 Doping

The band structure of an intrinsic semiconductor shows that under excitation the number of electrons in the conduction band is equal to the number of holes in the valence band. There are, however, small amounts of donor impurities and acceptor impurities in semiconductors. These impurities can occur naturally but are often intentionally added during fabrication to give the detector certain operational characteristics. An example of an n-type semiconductor is phosphorus doped silicon. The impurity atom substitutes a silicon atom in the covalent bonds of the lattice, leaving an extra electron bound weakly to the impurity site. This electron sits in a position near the top of the band gap called the donor level. Due to the weak bond, it is easy to promote the electron to the conduction band from the donor level, without leaving a hole in the valence band. The electrons in an n-type semiconductor will therefore significantly outnumber the holes, thus the electrons are appropriately named majority carriers and the holes are minority carriers. An example of a p-type material is boron doped silicon, the boron atom substitutes a silicon atom in the lattice site and will have one fewer valence electron which results in an acceptor level situated just above the valence band. In p-type semiconductors, the majority charge carriers are holes and the minority charge carriers are electrons [7] [10].

2.4.4 The p-n junction

A semiconductor detector relies on the junction of p-type and n-type semiconductor materials. A gradient of conduction electron density exists across the junction due to the higher density of conduction electrons in the n-type material and and holes in the p-type material.

A net diffusion of charge carriers is observed across the junction as electrons migrate from the n-type material and the holes diffuse towards the n-type material. When the electrons are removed from the n-type material, a net positive charge is observed on the n side of the junction. The opposite occurs with a p-type material where the net negative charge is observed. This results in a potential which induces a diffusion electric field across the junction.

At equilibrium, a region of steady-state charge distribution known as the depletion region is formed due to the induced potential. This region extends into the n and p sides at a distance depending on the doping concentrations of the materials.

The depletion region is essential in the detection of radiation. The electric field that exists across the depletion region causes any electrons that are created through the interaction of radiation to travel towards the n-type material, and the holes to travel to the p-type material. This produces an electrical signal.

The thickness of the depletion region is small, the detector when unbiased, resulting in charges becoming trapped due to the slow movement to the contacts. An external voltage is applied to counteract this at the junction, creating a reverse-biased diode. The applied bias is large enough so that the volume of the detector becomes depleted [7] [3] [10]. The thickness d of the depletion region is calculated from Equation 2.9

$$d \cong \sqrt{\frac{2\epsilon V}{eN}} \tag{2.9}$$

where ϵ is the dielectric constant of the material, V is the applied bias and N is the impurity concentration.

2.4.5 Charge Collection

The localised distributions of electrons and holes that arise from a photon interaction can be thought of as charge clouds. The Coulomb field emanating from the charge cloud extends through the crystal volume. As the charge clouds drift towards their collecting electrodes, they are influenced by the strength of the electric field, the Coulomb field changes. The total charge Q contained within the current pulse from the detector is proportional to the energy, E, deposited within the detector.

$$E \propto Q = \int i(t)dt \tag{2.10}$$

The electron-hole pairs produced through the interaction of gamma rays with the detector move under the influence of an electric field on the crystal. The time taken for these charge carriers to travel to their respective electrodes is the collection time. To calculate the total energy deposited within the detector it is therefore necessary to integrate the detector signal current. Ramo proposed a method to calculate the instantaneous charge and current induced on an electrode with the following equation, the induced charge Q_q on the electrode by a point charge q located at position x_o is:

$$Q_q = -q.\psi_0(x) \tag{2.11}$$

and

$$i = qv.E_0(x) \tag{2.12}$$

where v is the instantaneous velocity of the charge carrier q. $\psi_0(x)$ and $E_0(x)$ are the electric potential and field that exist at the position of the charge, if the selected electrode is at unit potential, and all others are set to zero potential with all charges removed from the system. The ψ_0 and E_0 parameters are the weighting potential and field, and are used to construct a measure of electrostatic coupling between the moving charge and the sensing electrode. In the case of a multi-electrode semiconductor diode the application of Ramo's theorem is complex due to the non - uniform electric field. The instantaneous induced current on an electrode $i_{electrode}$ of a charge moving in inter electrode space between positions, dl can be calculated as a function of the normalised potential $(V/V_{electrode})$ at that position.

$$i_{electrode} = \frac{d(\frac{qV}{Velectrode})}{dt} = q.\frac{d(\frac{V}{Velectrode})}{dl}.\frac{dl}{dt} \tag{2.13}$$

where $V_{electrode}$ is the external bias on the given electode with V being the potential at the position of charge q allowing the time dependence of the calculation to be translated into a position dependence. This calculation is valid if all other electrodes are grounded. The normalised potential is the weighting potential and the gradient of the potential is the weighting field E_w, given by.

$$\bigtriangledown(\frac{V}{V_{electrode}}) = -E_w \tag{2.14}$$

The calculated weighting potential for a multi-electrode planar detector is shown in Figure 2.6.

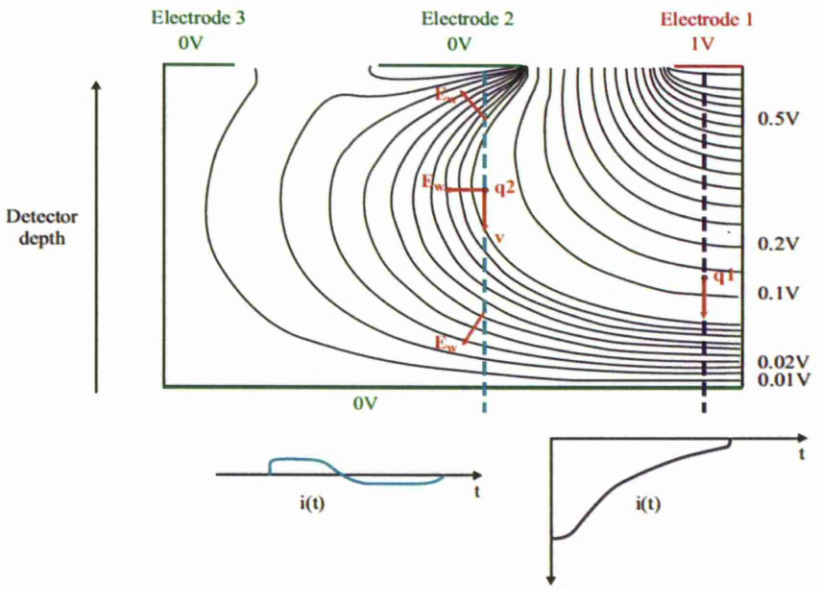

Figure 2.6: Calculated weighting field in a multi electrode planar HPGe detector. The measurement electrode is the rightmost strip. The induced current is shown for a charge terminating on the measurement electrode (right) and the neighbour electrode (left) showing the change in polarity.

Electrode one is at unity potential and all other electrodes are grounded. Plots of the induced current on electrode one are shown for two separate interaction positions, *q1* (purple) and *q2* (blue). The gaps between the lines represent the gradient of the potential. The field is strongest close to the contact and falls off as a function of distance. The weighting field depends on the specific geometry of the detector. The induced current on electrode one is calculated as,

$$i(t) = -q.v(\vec{r}(t)).E_w(\vec{r}(t)) \tag{2.15}$$

Thus the collecting charge Q, is given as,

$$Q = \int i(t)dt = -q\int_{x2}^{x1} E_w dl = q[V_w(x1) - V_w(x2)] \tag{2.16}$$

where *x1* and *x2* are the positions before and after the displacement of charge q.

2.5 High Purity Germanium (HPGe)

As most of this thesis will concentrate on HPGe it is important to discuss this material. Germanium has been used in gamma spectroscopy for many years due to its excellent energy resolution and good efficiency. Techniques for the production of high-purity germanium with impurity levels as low as 10^{10} atoms/cm^3 were first developed in the mid 1970s. The starting material is bulk germanium, which is further refined through processing. The impurity levels are progressively reduced through repetitions of processing until the impurity level is as low as 10^9 atoms/cm^3 [7]. A semiconductor material provides superior energy resolution when compared to a scintillation material, this improvement can be attributed to the larger number of charge carriers liberated during a gamma ray interaction [11].

Typically a scintillation material will require $\approx$ 100eV for the liberation of a charge carrier. However the small band gap in germanium means only $\approx$ 3eV is required to promote a charge carrier from the valence band to the conduction band. For a given gamma-ray interaction, a larger number of carriers are produced per unit energy deposited in a germanium detector as opposed to a scintillation detector.

Table 2.1: Properties of Germanium

Material	Ge
Average atomic number	32
Density(g/cm^3)	5.33
Resistivity(Ω cm)	50
Band gap (eV)	0.67
Pair creation energy (eV)	2.95
Electron mobility (cm^2/Vs)	3900
Hole mobility (cm^2/Vs)	1900

Germanium has an atomic number if 32 and is a group IV element with a diamond structure.

2.6 Detector performance

To understand how a detector is operating, it is important to measure the detector performance quantitively. The detector measurements used to assess the performance are the energy resolution, counting efficiency and the peak to total. These will be discussed further in the following discussion.

2.6.1 Energy resolution

In most radiation detection systems, a quantitative measurement of the energy deposited by incident radiation is essential. Energy resolution is used to describe the precision with which a system can determine the energy deposited in the detector. There are a number of factors which contribute to the intrinsic energy resolution E_T , of a radiation detection system, this is shown in the following equation:

$$E_T^2 = E_S^2 + E_X^2 + E_E^2 \tag{2.17}$$

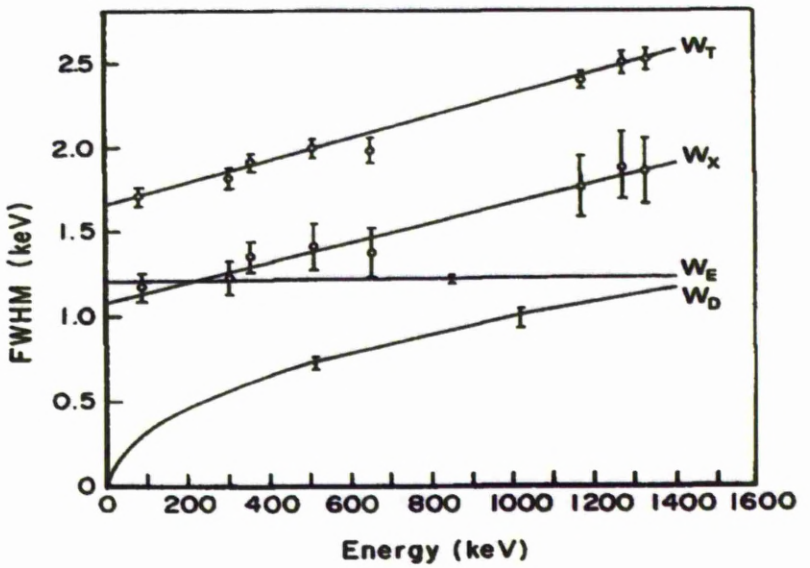

Figure 2.7: Figure showing the contribution of each factor to the energy resolution of a detector system [12]

where E_X represents signal losses in the detector such as incomplete charge collection in semiconductor diode detectors and light loss in scintillation detector systems. The contribution of E_E is due to noise from the electronics, the effects of these on a detector system can be seen in Figure 2.7.

At low energies the contribution from the electronic noise and charge collection dominate, with carrier statistics, E_S becoming significant at higher energies. The inherent contribution of E_s arises from statistical fluctuations in the number of charge carriers produced per interaction event N_{pair}, given by:

$$(\Delta E_S)^2 = \frac{(2.35)^2 F}{N_{pair}} \tag{2.18}$$

where F is the Fano factor which accounts for the deviation from pure Poisson statistics of the experimentally observed statistical fluctuation of the number of charge

carrier pairs produced.

2.6.2 Efficiency

The counting efficiency of a gamma-ray detector is essential to determine the quantity of radiation emitted from a source. There are three definitions that describe efficiency, these are; absolute efficiency, intrinsic efficiency and relative efficiency. The absolute efficiency is defined as:

$$\epsilon_{abs} = \frac{N_{detected}}{N_{emitted}} \tag{2.19}$$

where $N_{detected}$ is the number of detected events and $N_{emitted}$ is the number of gamma rays emitted from the source of radiation. The absolute efficiency is dependent on detector properties and the solid angle subtended by the detector. In order to remove the dependence on solid angle, the intrinsic efficiency may be quoted:

$$\epsilon_{int} = \frac{N_{detected}}{N_{incident}} \tag{2.20}$$

where $N_{incident}$ is the number of gamma rays incident on the detector.
The intrinsic efficiency is dependent on the physical properties of the detector and the energy of the incident gamma rays.

As the physical properties of the detector, such as size, heavily contribute to the intrinsic efficiency it is useful to measure its counting ability relative to an industrial standard. Therefore, the absolute efficiency of a detector is measured using a 1332keV ^{60}Co gamma-ray source placed 25 cm from the detector face, then the relative efficiency is calculated by dividing the result by $1.24\text{x}10^{-3}$,which corresponds to the absolute efficiency of a 76 mm x 76 mm NaI(Tl) detector.

2.6.3 Peak to total measurement

The measurement of the number of gamma-ray events detected in the full-energy peak compared to the total gamma-ray events emitted by the gamma-ray source is given

by the full energy peak efficiency. The calculation of the full energy peak is given by the ratio of the number of counts detected in the peak to the number emitted by the source.

$$\epsilon = R/(S \times P_\gamma) \tag{2.21}$$

where R is the full-energy peak count rate in counts per second. S is the source strength in disintegrations per second such as Becquerels. P_γ is the probability of emission of a particular gamma ray.

Chapter 3

Compton imaging techniques

Compton imaging was initially proposed independently by Pinkau [13] and White for imaging solar neutrons [14]. This technique has diversified into many other application fields, with the ability to locate and identify a source, such as:

1. Medicine: using a Compton camera setup results in a superior counting efficiency and the ability to locate a source. The advantage is that a smaller amount of radionuclide needs to be injected into the patient.

2. Nuclear non-proliferation: in the nuclear non-proliferation field, there is a need for portable gamma-ray imagers that can quickly detect hidden or unseen quantities of highly enriched uranium (HEU). Compton camera imaging has certain advantages that are attractive over coded aperture imaging, as heavy metal collimator reduces the ability to image at much higher energies.

3. Environmental monitoring: the advantage of Compton imaging for environmental monitoring is the ability to have a large field of view.

3.1 Current systems

Currently the most common techniques to identify and locate radioactive sources rely on the use of mechanical apertures, typically made of lead or tungsten. A collimator

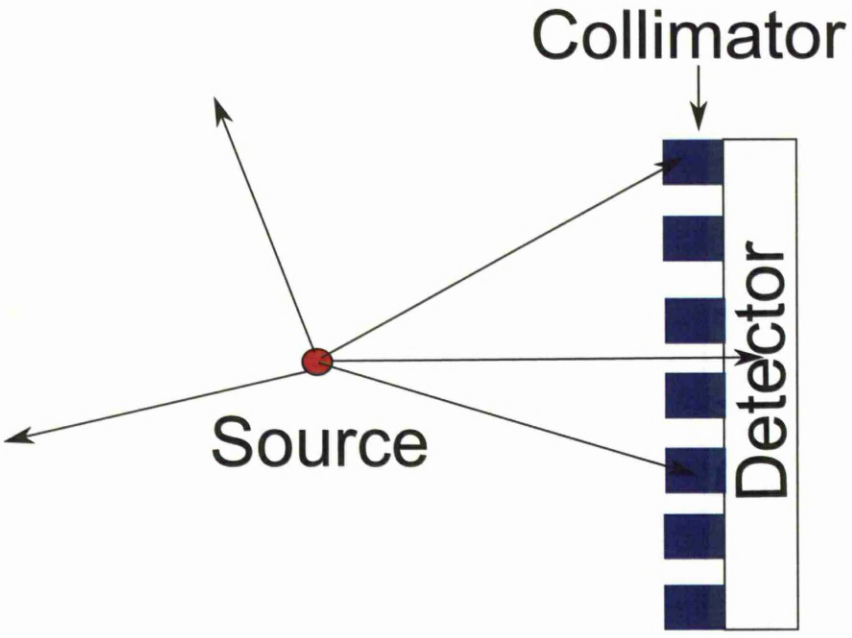

Figure 3.1: Figure showing an example of a mechanical collimator setup with a source set at an arbitary distance

in its simplest form is a pinhole or pinhole array, which is placed in front of the detection device limiting the angle of incident radiation, as shown in Figure 3.1 [14]. Limiting the direction of incident radiation allows only those gamma rays that are incident from a certain direction to be detected, allowing positional information to be collected. The disadvantage of this technique is that many of the gamma - ray events are absorbed in the collimator leading to a detector with very poor sensitivity [2].

The disadvantages associated with this type of setup are:

1. As the position resolution increases the counting efficiency decreases.

2. High-energy gamma-rays can penetrate the collimator.

Another method is to use a coded aperture by creating a carefully selected pattern in a collimation material as shown in Figure 3.2. Each hole projects its own image

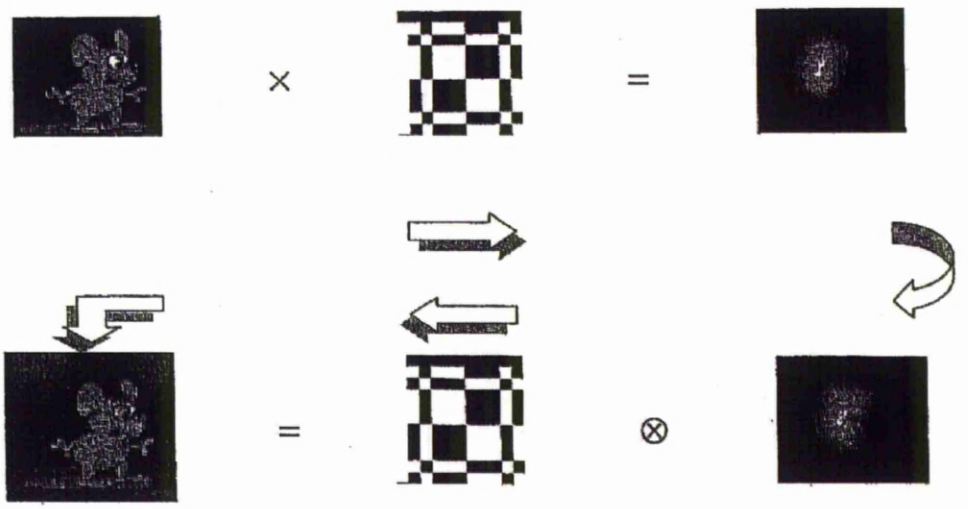

Figure 3.2: Figure showing the operation of a coded aperture. Each hole projects its own image on the detector, and the different images overlap. If the hole pattern is known, this can be reconstructed mathematically to enable the direction of the source to be found. If it is assumed that radiation is coming from a very distant source. [15]

on the detector, and the different images overlap. If the hole pattern is known, this can be reconstructed mathematically to enable the direction of the source to be found.

If it is assumed that radiation is coming from a very distant source the gamma rays from this source are parallel, so a shadow of the mask is projected on the detector much the way it would be projected by the sun. Each pixel in the image is represented by parallel gamma rays incident from one direction that project a detector-sized portion of the mask pattern onto the detector. The pattern is selected such that each projection is unique and independent of all other projections.

The image is recreated through a cross-correlation technique: the complete detector pattern is summed against each unique mask position by adding counts to the

sum if the mask is open at this position, and subtracting them if it is closed. Counts are added if they could have originated from that direction and subtracted if they could not. This technique has the advantage that the limiting sensitivity of a collimated system has been improved upon, but to be effective an aperture that has been carefully selected must be used. As the whole of the detector area is not utilised the detection ability of the detector is impeded [15].

3.2 Principles of Compton imaging

Compton cameras rely on electronic collimation, which is commonly performed by using two or more position and energy sensitive detectors. However, using a single monolithic gamma-ray detector will be discussed later. For the simplification of this discussion, to separate the two interactions of a gamma-ray event we will assume that there is one interaction per detector. A gamma ray will Compton scatter through interacting with an electron, shown in Figure 2.2, in the scatter detector. The scatter detector is designed to maximise the probability of a Compton scatter. A fraction of its energy will be deposited in the scatter detector carrying on into the second detector that is designed to absorb the remaining energy of the scattered gamma ray via photoelectric absorption.

The energy of the scattered photon $E_{\gamma'}$ is found from the initial energy E_γ of the photon and the angle through which it is scattered θ by

$$E_{\gamma'} = \frac{E_\gamma}{1 + \frac{E_\gamma}{m_0 c^2}(1 - cos\theta)} \quad (3.1)$$

where $m_0 c^2$ is the electron rest mass [3].

The two detectors are operated in coincidence, so that only gamma photons that interact with both detectors and deposit a total energy within a given time window are recorded, see Figure 3.3. This means that the energies deposited in the two de-

tectors and the direction of travel after passing through the first detector are known. If a photon with energy E_0 is incident upon the scatter detector the photon scatters and deposits energy equal to E_S in the first detector. It then carries on depositing the remainder of its energy, E_A, in the second detector [16] [17].
By adding the energy deposited in both detectors it is possible to determine the energy emitted from the source given by equation 3.2

$$E_0 = E_A + E_S \tag{3.2}$$

Using the known information of energy and position per event for an interaction in the scatter and absorber detector equation 3.3 can be used to back project and create a cone to find the origin of the photon. Figure 3.3 shows how this is achieved, the opening angle of the cone, θ, is calculated from the Compton formula 3.3. The vector difference of the positions of interaction in the scatter and absorber detectors are then used to define the cone axis.

$$cos\theta = 1 - \frac{m_o c^2 E_s}{E_0 E_A} \tag{3.3}$$

The scattering angle is used to form a cone apex with an angle 2θ, as it is not known what direction the recoil electron travels.

θ is the Compton scatter angle; E_1 is the recoil electron energy in the front detector; E_0 is the source energy; and $m_o c^2$ is the rest mass of an electron (511keV).

To locate the radionuclide accurately many more events from the same source will need to be used. This will produce many more cones, with the origin of the source being the point where the bases of all these cones overlap as shown in Figure 3.4.

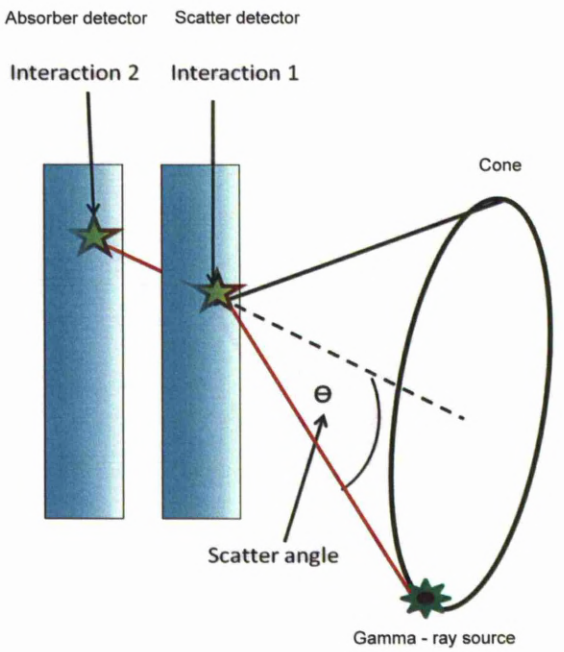

Figure 3.3: Figure showing the possible origin points of a source through cone reconstruction.

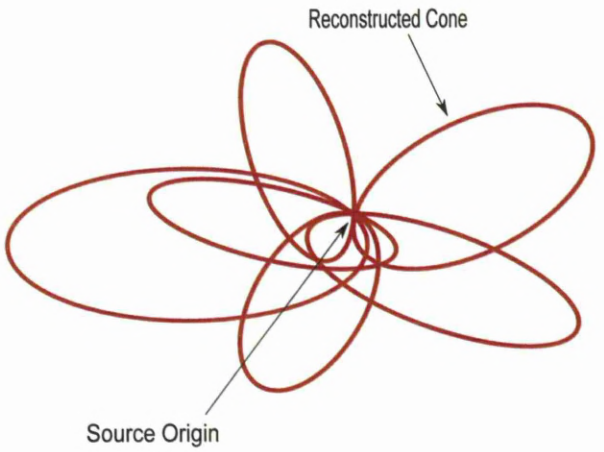

Figure 3.4: Figure showing overlapping cones that show the position of origin of the source.

3.3 Factors influencing Compton system performance

The accuracy of the size and position of the cones depends on the ability to determine accurately the energy deposited in the scatter and absorber detector and the position of interaction. It is therefore important for an imaging system to provide spatial resolution and detection sensitivity for incident gamma rays. The factors influencing the performance are [18]:

- The energy resolution of the detector
- The position resolution of the detector
- Doppler broadening

3.3.1 Effect of the energy resolution on the angular uncertainty

The Compton scatter equation, equation 3.3, shows that error in the angle of scatter originates from the uncertainty in the measurement of the energy in the scatter detector.

When the scatter angle is calculated using both the scatter energy and the absorber energy, the uncertainty on the scattering angle is given by equation 3.4 [19],

$$\Delta\theta = \frac{m_0c^2}{E_0\overline{E}_A{}^2 sin\theta}\sqrt{(\overline{E}_A\Delta E_S)^2(\overline{E}_S\Delta E_A)^2} \tag{3.4}$$

where E_S and E_A refer to the energy deposited in the scatter and absorber detector respectively. $\overline{E}_A$ and $\overline{E}_S$ refer to the mean values of the energy deposition in the scatter and absorber detector respectively. ΔE_S and ΔE_A refers to the Full Width Half Maximum of the detector at a defined energy.

This function is plotted in 3.5 for four different gamma-radionuclide energies.

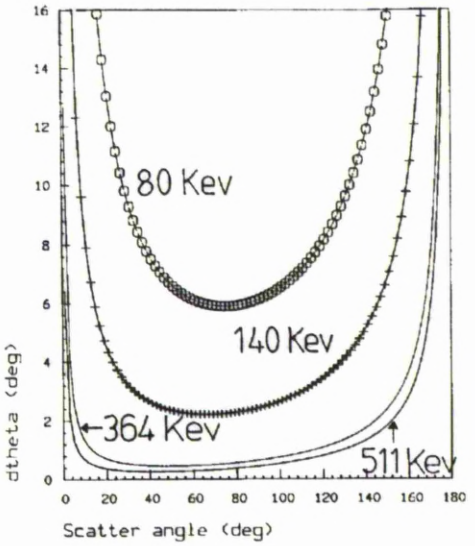

Figure 3.5: The FWHM uncertainty in the Compton scattering angle per keV energy resolution against the scattering angle for four different radionuclide energies [12].

3.3.2 Effect of the position resolution of the detector for imaging

During a single event the uncertainty on the vector on the cone axis due to the detectors finite position resolution is given by the equation:

$$\Delta\theta = \frac{E_1.r_m + E_2.r_m}{|{r_m}^2|} \tag{3.5}$$

where $E_{1,2}$ are the error vectors going from the measured points of interaction, (x_1, y_1, z_1) and (x_2, y_2, z_2) to the true points of interaction, $({x_1}^T, {y_1}^T, {z_1}^T)$ and $({x_2}^T, {y_2}^T, {z_2}^T)$ and r_m is the vector $(x_2\text{-}x_2)i + (y_2\text{-}y_2)j + (z_2\text{-}z_2)k$, where i,j and k are unit vectors representing the x,y and z axis respectively.

3.3.3 Effect of Doppler broadening of the detector for imaging

It is assumed that the electron has zero momentum to simplify the relationship between the energy deposited in the scatter detector and the scattering angle. However, in reality the electron is moving and bound to an atom in the scattering material, resulting in a non-zero electron momentum distribution. This results in the broadening of the energy spectra in the scatter and absorber detectors and is independent of the intrinsic energy resolution of the detector. The influence of the Doppler broadening is predicted to be more significant in materials with a high atomic number as the density of electrons will be greater. As the quantitative contribution of Doppler broadening is intrinsic to the scattering material, it is essential to take this into account when determining the optimum Compton camera configuration. It has been shown by Harkness [10], that for a HPGe/HPGe scatter and absorber event the Doppler broadening can affect the image resolution $FWHM_x$ of the detector by 9mm. Therefore any simulation that is carried out will incorporate Doppler broadening to ensure the best reproduction of experimental data.

3.4 Comparison of detector materials for Compton Imaging

A comparison of detector materials and their suitability for Compton camera imaging will be discussed in this chapter. In the previous sections the operation of a Compton camera relies on detectors that can provide excellent position and energy resolution. Table 3.1 shows some commonly used semiconductor materials and their associated properties.

Table 3.1: Comparison of materials for Compton camera optimization

Material	Ge	Si	CZT
Average atomic number	32	14	49.1
Density(g/cm^3)	5.33	2.33	5.78
Resistivity(Ω cm)	50	$< 3 \times 10^4$	3×10^{10}
Band gap (eV)	0.67	1.12	1.64
Pair creation energy (eV)	2.95	3.62	4.64
Electron mobility (cm^2/Vs)	3900	1400	1000
Hole mobility (cm^2/Vs)	1900	480	65

3.4.1 Germanium

Germanium detectors provide very high energy resolution and the crystals can be grown several centimetres thick with relatively small impurities, and combined with the high density of germanium, generate relatively high efficiencies [20].

The Compton scattering and photelectron interaction cross sections for germanium compared to silicon can be seen in 3.7. It can be seen that the cross section for Compton scattering is relatively high between 0.01 and 0.1 cm^2/g over an energy range of 1 keV to 10 MeV. The cross section for photoelectric absorption is an order of magnitude greater than silicon for energies above 100 keV. This makes germanium less desirable as a scattering detector for a Compton imaging setup as it is necessary to maximise the number of scattered gamma rays and minimise the number of gamma rays absorbed in the scattering material.

However, germanium has excellent energy resolution which is a consequence of the low band gap energy as a large number of charge carriers are generated for each gamma-ray interaction, reducing statistical variations.

3.4.2 Silicon

Silicon has a higher band gap energy enabling it to be used at room temperature although the typical energy resolution of silicon is less than that of germanium. Silicon has a much lower atomic number than that of germanium causing degradation of the intrinsic energy resolution of scattered gamma rays due to the Doppler broadening, which is significantly less than in germanium.

The cross section for Compton scattering is higher than that of germanium for gamma-ray energies below 1 MeV and similar above 1 MeV. The photoelectric absorption, however, is much lower than that of germanium. This makes silicon an excellent scattering detector material [21].

3.4.3 Cadmium Zinc Telluride

Cadmium zinc telluride was developed from cadmium telluride, a II-VI semiconductor, to allow higher resistivities and lower leakage currents. A band gap of 1.6 eV can be achieved enabling it to be used at room temperature. The Compton scattering cross section for CdZnTe is comparatively low. However, its photoelectric absorption cross section is higher than that of germanium or silicon. The high density of CdZnTe means there is a high stopping power for gamma rays in the material and makes it an efficient absorber of gamma rays. However, it is unsuitable as a scattering detector due to its high Z value. This material also suffers from poor intrinsic energy resolution due to poor charge mobility of charge carrying holes within the material. The hole mobility is an order of magnitude lower than that the electron mobility.

This hole trapping results in a detector material that is very sensitive to the depth of interaction. Signals arising from interactions that occur close to the negative electrode will be primarily due to the drift of the electrons. Interactions that occur deeper in the detector will have a greater dependence on the hole mobility and a proportion of holes will be trapped leading to incomplete charge collection observed as a low energy tail in the photopeak of the energy spectrum. Through careful design of the segmentation of the electrical contacts the effect of the hole mobility and trapping

can be reduced [22] [23][24][25][26].

3.4.4 Caesium Iodide

Caesium iodide is a scintillator, the energy resolution of CsI is relatively poor compared to semiconductor materials, discussed in the previous chapter. This would therefore make it unsuitable for use as a scattering detector for which excellent energy resolution is crucial. However the materials high density and low cost means it could be used as an effective absorber. The plots shown in Figure 3.7 show that the cross section for Compton scattering is relatively low while the cross section for photoelectric absorption is significantly higher than germanium or silicon and comparable to CdZnTe. The average Z value of 54 is relatively high so the level of Doppler broadening will be high. CsI has a significant advantage over semiconductor materials in that they are significantly cheaper and more widely available. Position resolution can be achieved through the use of pixel detectors. These are individual crystals whose scintillation light is isolated from its neighbours [22].

3.4.5 Conclusion

The discussion above gives an insight into creating an optimum Compton imager. Silicon is the most suitable material to use for a scatter detector, having a high Compton cross section, whilst providing an excellent energy resolution, reducing the uncertainty on the opening angle of the detector. However, it is not an ideal absorber detector. Ideal candidates for this are CsI and CdZnTe both of which have similar material properties and absorption cross sections. To reduce the error on the cone axis and opening angle using a CdZnTe detector would be favourable with excellent spectroscopic performance compared to CsI. However reference [27] has suggested that if the incident gamma-ray energy is known then the scatter detector need only be the detector with excellent energy resolution allowing an absorber detector with poor energy resolution but good position resolution to be used. Though this situation is rarely the case in security scenarios, in medical imaging scenarios this is useful.

Finally, the electronics must not introduce noise into the system as this would add uncertainty into angular resolution of the reconstructed cone.

3.5 Methods of image reconstruction

An image reconstruction algorithm is an important tool to turn the raw hits recorded into 3-D images. There are two main types of reconstruction that are used; iterative and analytical methods.

Analytical image reconstruction algorithm methods rely on the position and energy deposited in the scatter and absorber detector to create a reconstructed image. This typically carried out using back projection, this thesis will concentrate on using this approach and is further discussed in the next section 3.6 [2]. Iterative techniques compare an estimated projection to the measured position and energy values.

A guess of the 3-D distribution is made and successive modifications of that estimate are made until a solution is reached. The basic process is to descritise the image into pixels, each pixel value is unknown then using linear equations that model the imaging geometry and physics a solution can be found to locate the image source in 3-D space.

However the complexity and computer intensity of iterative techniques most reconstruction algorithms are based on analytical rather than iterative methods [28] [29].

3.6 Cone reconstruction used in this discussion

To locate the source in 3-D space, the energy deposited and the position of interaction in the scatter and absorber detector must be known. Vectors are used to reconstruct the source position. All 3-D vectors can be represented by a direct line from the start point to an end point in 3-D space. The length of the line represents the magnitude of the vector and the difference in the start and end positions gives the direction of the vector. The origin of the vector is the first hit detector position given by x_1, y_1, z_1 and its end position is given by x_2, y_2, z_2. The magnitude of the vector a can

be calculated from the position difference between the x, y and z components. The vector is calculated using equation 3.6

$$\sqrt{dx^2 + dy^2 + dz^2} \tag{3.6}$$

Once this magnitude vector has been calculated this gives the axis vector of the reconstructed cone, with an opening angle given by θ. This axis and opening angle now need to be projected out into z - space to create a cone. The C++ programming language has been utilised to calculate the direction vector from the interaction positions and the opening angle of the cone. This requires the user to input the desired reconstruction z-plane Figure 3.6. Using this information the axis vector is reconstructed out to and projected onto this plane.
The angle of scatter from this axis is then reconstructed back to the inputted z plane and an ellipse is projected onto this plane, with a centre of the ellipse being the projected axis and the ellipse being created from double the angle of scatter.

Once the data have been put into the correct format of $Z_1, Y_1, X_1, E_1, Z_2, Y_2, X_2, E_2$, these data are inputted into a C++ code developed by D.S.Judson [30] to reconstruct simulated and experimental data.
The data once transformed into the correct format are read into the C++ code, so that the positions of interaction and energy can be interpreted as a Cartesian position in 3D space.
The procedure to interpret this position is called image reconstruction and the image created by this reconstruction is referred to as a projection.

The C++ reconstruction code is a simple back projection analytical algorithm. The term back projection is applied if there is no enhancement of the image through filtering or iterative approaches.

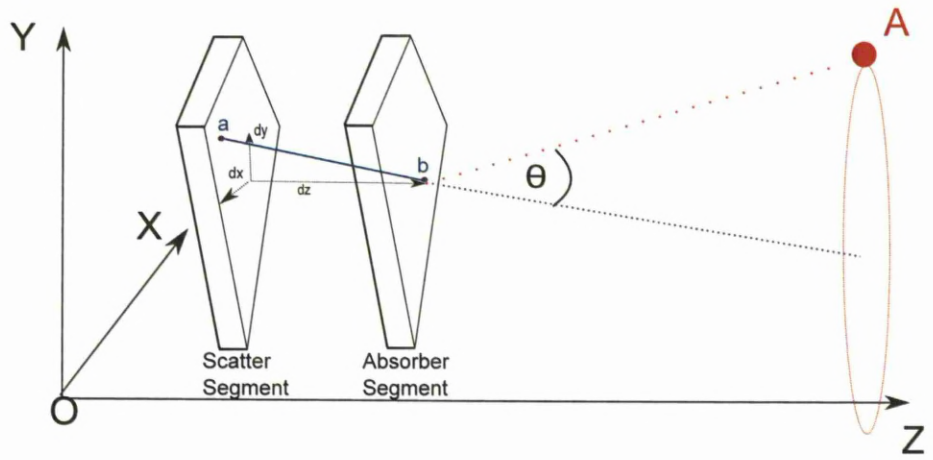

Figure 3.6: Figure to show the creation of an ellipse in the z-axis. d_x,d_y,d_z is the difference between the position of interaction in the scatter and absorber detectors in the x,y and z axis. a and b represents the the interaction position with a line vector between the two that is extended out along the z axis. θ represents the opening angle of the cone. The letter A represents a gamma ray source located at a distance along the z axis.

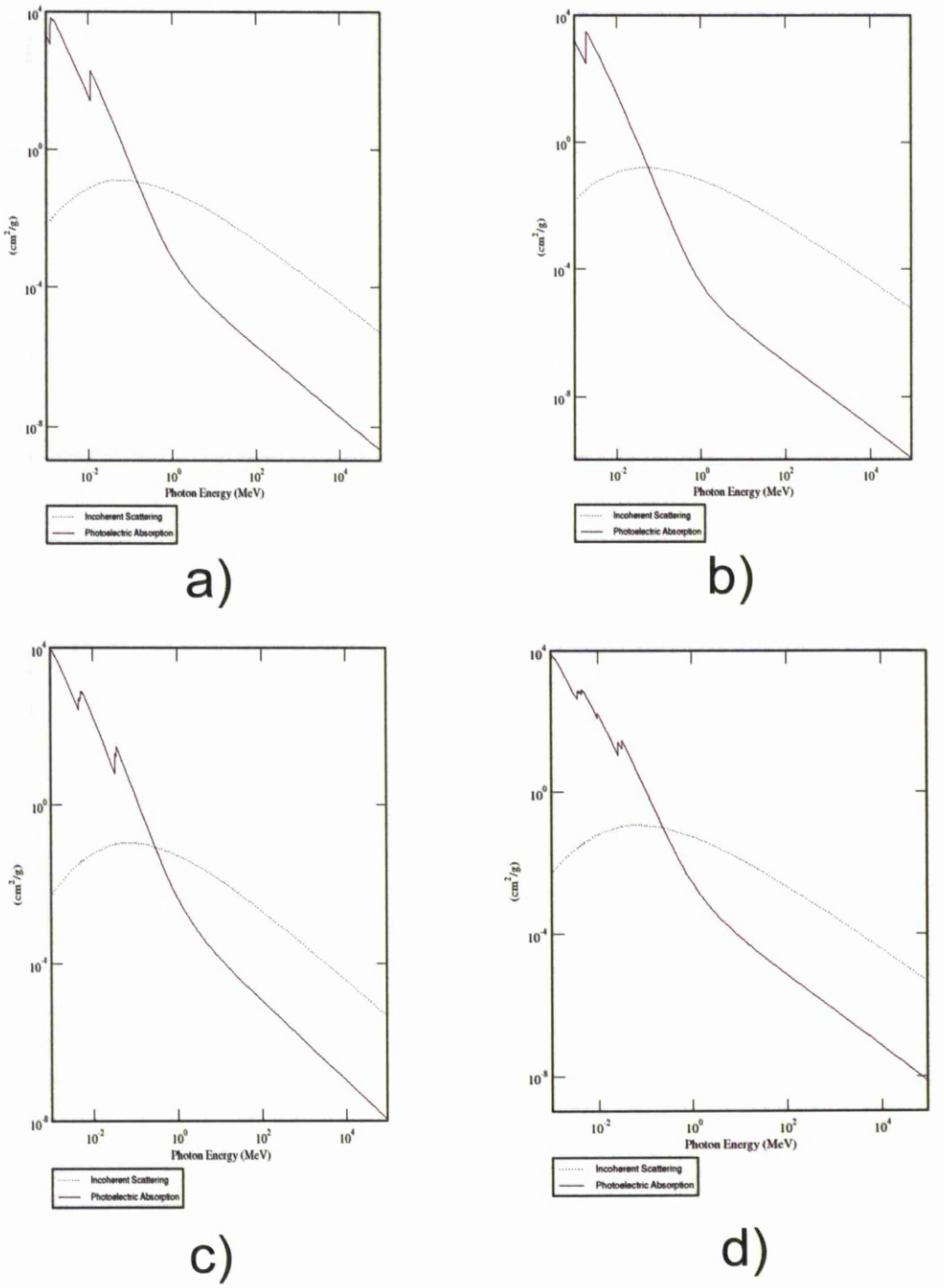

Figure 3.7: Figure showing Compton and photoelectric absorption cross sections for a) germanium, b) silicon, c) caesium iodide, d) cadmium zinc telluride [31].

Chapter 4

Testing of CZT for use with the GammaKEV project

4.1 Vibration testing of CZT

An important part of the GammaKEV project was the ability for the imaging device to be used in extreme conditions. Tests were carried out to assess the suitability of CZT in environments with high background noise at BAE Systems in Barrow in Furness as previous research has shown that CZT exhibits a strong piezoelectric effect [32][33].

The experiment was setup as shown in Figure 4.1 and 4.2. One co-planer and three planer CZT detectors were attached to a vibration rig, a Signal Force IV46, to test their response. The detectors were tested over a frequencies ranging from 40Hz through to 10kHz.

The response of the accelerometer and the detector, when placed on the test rig, can be seen in Figure 4.3. The accelerometer shows the acceleration generated on the detector by the test rig and the detector response shows the signal produced by the detector whilst the test rig is operational.

The results over the four detectors and the whole frequency range show the same behaviour to that in Figure 4.3. This would suggest that vibrations are a major

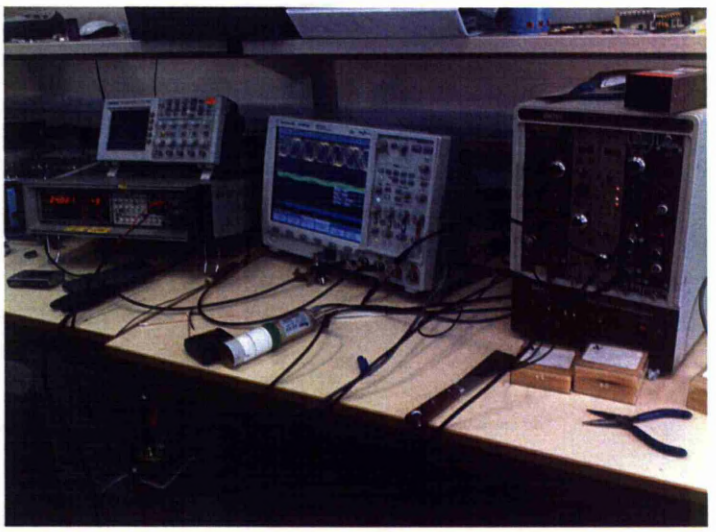

Figure 4.1: A photograph of the noise tests at BAE Systems. The photograph shows a Flyde frequency generator, oscilloscope and ORTEC minibin. The preamplifier can be seen attached to the table.

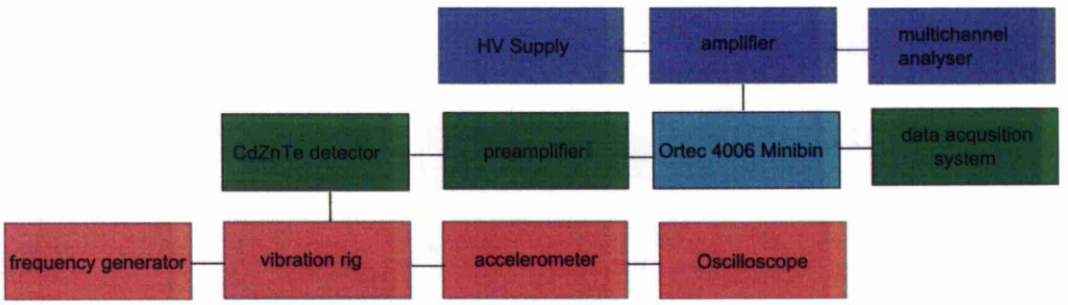

Figure 4.2: A diagram of the setup of the vibration tests.

consideration to take into account when using CZT detectors for portable gamma-ray imaging and spectroscopic devices. However, further investigation revealed that the observed effects did not originate through the detector. Sending a pulser through the preamplifier whilst operating the vibration test rig reproduced a similar response to that of the accelerometer.

The analysis of the vibration tests suggest that it is important to consider the design

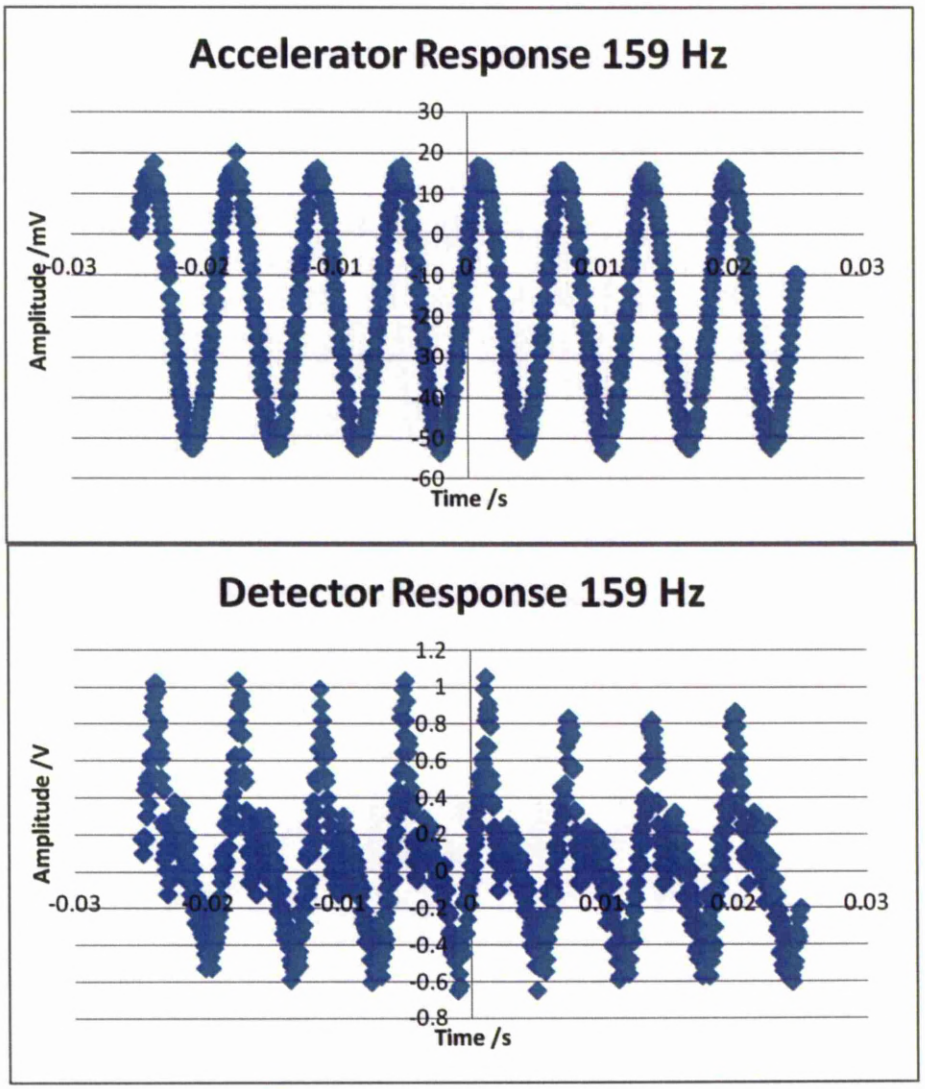

Figure 4.3: The response of the accelerometer and the detector at 159 Hz.

of the electronics to negate the effect of vibration and noise on a portable gamma-ray imager.

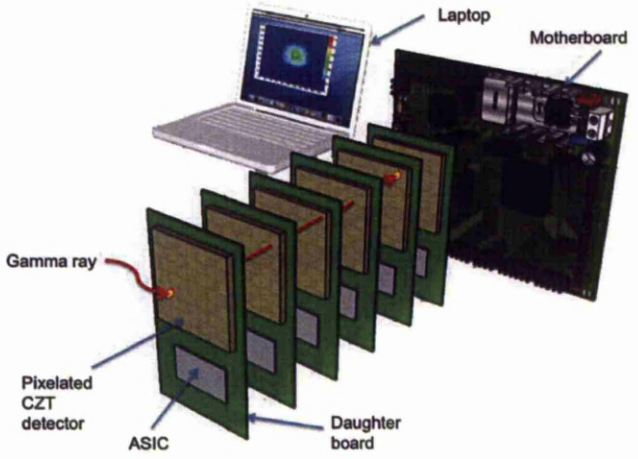

Figure 4.4: A schematic of the PorGamRays spectrometer [34].

4.1.1 Compton image reconstruction using CZT

The PorGamRays project was of interest to the GammaKEV project as this focused on the development of a portable gamma-ray imaging device for Compton imaging. It has the ability to provide spectroscopic energy information over an energy range from a few keV to a few MeV. The PorGamRays project aimed to develop a portable gamma-ray detector system designed around a stack of CZT detectors. This device is a hand-held portable gamma-ray imaging and spectroscopic sensor with the ability to be operated at room temperature. The design of the PorGamRays project enables multiple wafers of CZT to be used. This provides a suitable volume of material to provide good detection efficiency whilst reducing the thickness of CZT used that could cause degradation in spectroscopic performance due to poor hole mobility. The device uses a stack of six thin eV Products CZT detectors, each 2 mm thick separated by 4 mm. Each of these detectors has dimensions of 20 mm x 20 mm with a segmentation of 100 pixels. The data from each of these pixels are processed through an application specific integrated circuit (ASIC) designed by the Rutherford Appleton Laboratory (RAL). The ASIC and the CZT detector are bonded to a daughter board,

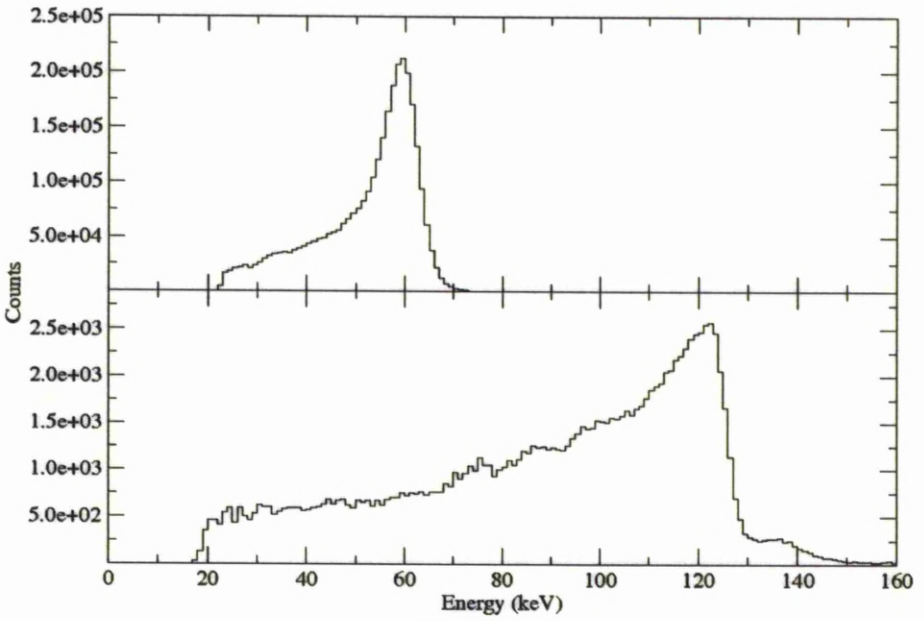

Figure 4.5: This figure shows two spectra. The top spectrum shows a ^{241}Am spectrum taken with a 100 pixel CZT detector through a NUCAM II ASIC and on the bottom a ^{57}Co spectrum.

which in turn are attached to a motherboard to correlate the data from all the daughter boards. The correlated data is then output to an external computer; a schematic of this setup can be seen in Figure 4.4. The advantage of such a design enables the ASIC's to be easily replaced and different detector material to be incorporated.

It was decided that the CZT detectors should be attached to a 128 channel NUCAM II ASIC [35]. These cards are early iterations of the final PorGamRays ASIC but have a limited dynamic range corresponding to a maximum energy of 350keV. This is significantly less than the original specification for the project, which specified a range of 60 keV to 6 MeV. This limits the energy range of gamma-ray sources the that the demonstrator can image. Initial tests using the NUCAM II card found that the device provided excellent gamma-ray energy resolution below 60 keV and deteri-

orates with increasing energy. In Figure 4.5, the top spectrum shows a peak at 59.5 keV the FWHM has been calculated to be 12 keV. The spectrum below shows an energy increase to 121 keV. The 121 keV peak exhibits a much more significant low energy tail. This is due to charge being lost to neighbouring pixels as the NUCAM II ASIC does not allow for recovery of these events. The future PorGamRays ASIC will provide recovery of charge lost to neighbouring segments resulting in an improvement in spectroscopy at higher energies. The electronic noise level corresponds to an energy of 15 keV. This is mainly due to the capacitance of the wire bonds between the detector and the ASIC.

Compton image reconstruction was carried out utilising a NUCAM II ASIC bonded to a CZT. A ^{133}Ba source was placed 35mm from the front face of the scattering detector in the z direction and positioned at 100 and 115 mm, in x and y, respectively. From Figure 4.6 it can be seen that the source position is clearly identified. The position resolution (FWHM) of the image is measured as 20mm in both x and y [34].

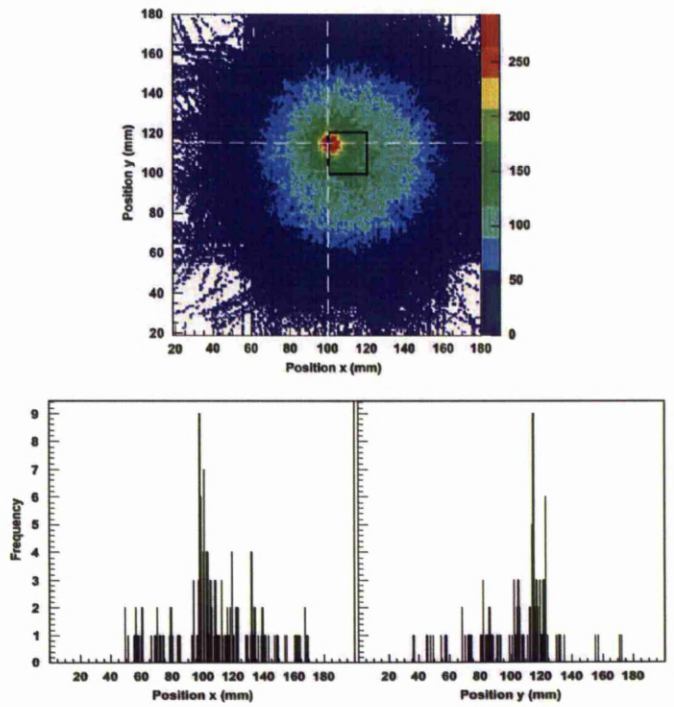

Figure 4.6: A Compton image of a ^{133}Ba point source in the xy plane. The source was placed at x = 100 mm, y = 115mm, as indicated by the intersection point of the dashed white lines. The black square indicates the position of the detector [34].

Chapter 5

Experimental setup

5.1 Detector

Each crystal has a lithium drifted centre contact (p^+) and 36 electrically segmented boron implanted outer contacts (n^+). Initially the volume of the crystal is a cylinder of HPGe with a length of 90 mm and 80 mm in diameter, the schematic of the AGATA crystals can be seen in Figure 8.1. The cylinder is ground down and shaped into six tapered surfaces extending 76.8 mm from the front face of the cylinder. A hole of 5mm radius is bored from the back of the crystal to a depth of 77 mm. To create 36 electrically segmented contacts the crystal is segmented into six rings of depth 8 mm, 13 mm, 15 mm, 18 mm, 18 mm, and 18 mm. Each ring is segmented into six equal portions, the segment map used for this experimental setup can be seen in Figure 5.2.

5.2 Electronics

The electronics components used for the Compton imaging measurements are shown in Figure 4.3. The AGATA preamplifiers, were located within the cryostat, these 37 preamplifier channels each had gain of 100mV/MeV and provided differential output signals for low noise transmission to the digitisers.
Preamplifier signals were passed through Low-Voltage Differential Signaling (LVDS)

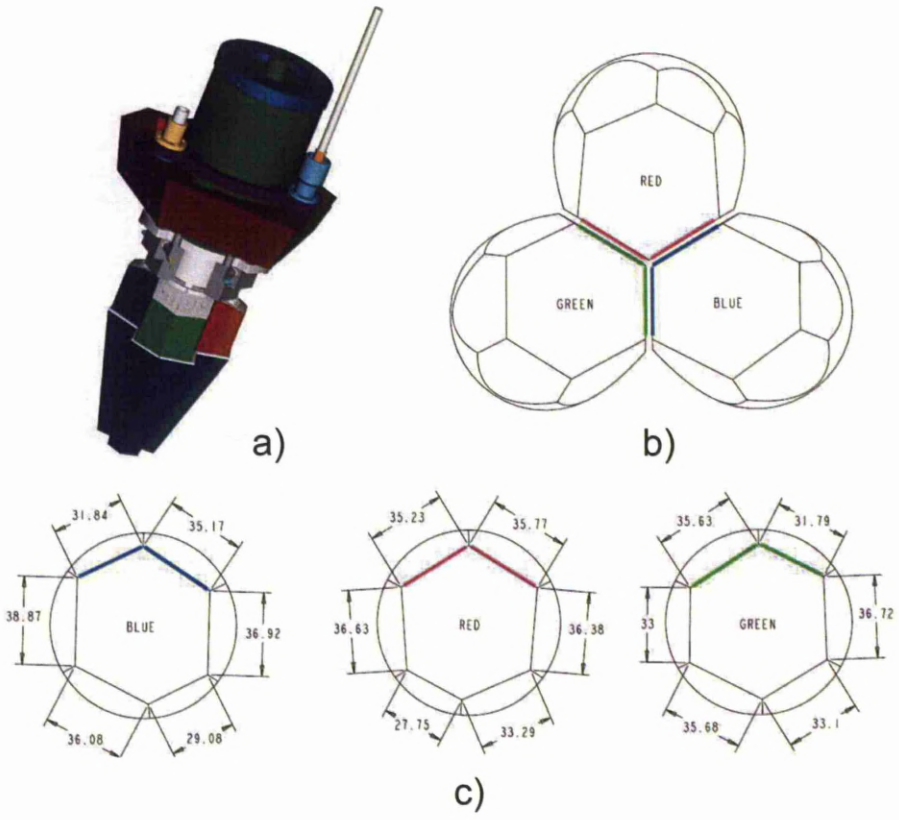

Figure 5.1: AGATA asymmetric cryostat ProEngineer model and projections. a) Representation of the asymmetric AGATA triple cluster cryostat. b) Schematic diagram of the crystal configuration. c) Blue, red and green asymmetric crystal geometry specifications. [36]

cables to the CWC converter boxes, which were manufactured at Technical University Munich and Institut fr Kernphysik der Universitt zu Kln and installed within a standard Nuclear Instrumentation Module (NIM) crate. The converter boxes recombined the differential signals, providing one single-ended output for each segment and three identical outputs for the core.

All segment signals and one of the core signals were sent directly from the CWC converter boxes to the GRETINA digitiser cards. The second core signals were used

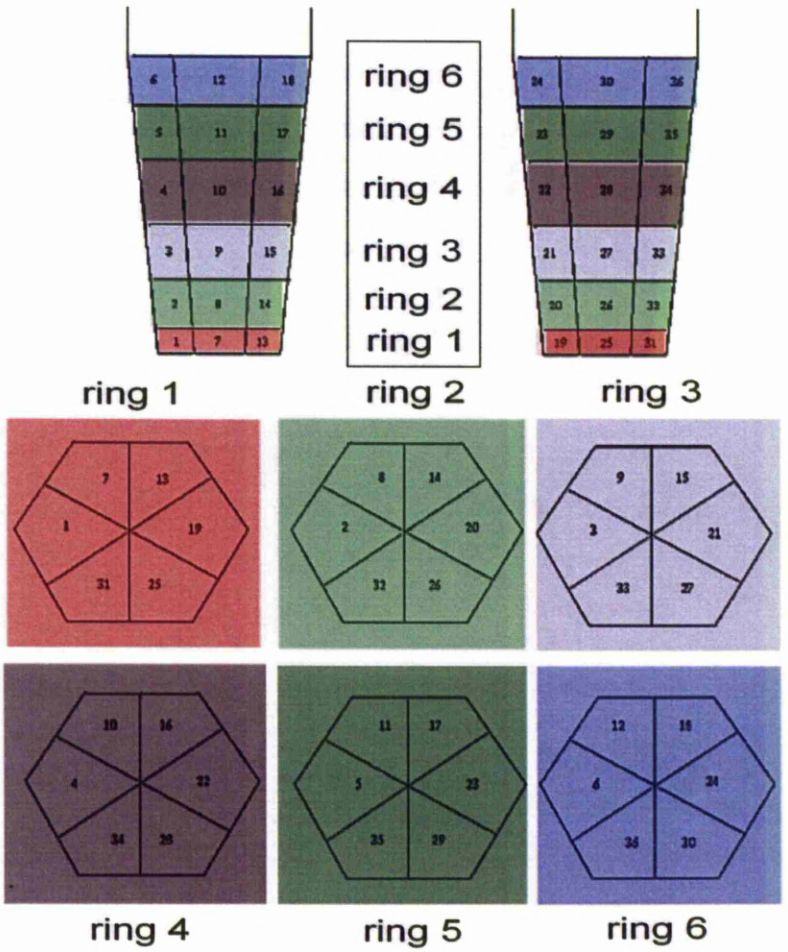

Figure 5.2: The AGATA A006 detector is electronically segmented into 6 rings, each with 6 segments per ring

for an analogue measurement of the deposited energy; an ORTEC 671 spectroscopy amplifier, with a 6μs shaping time was used to shape the signal and a Silena ADC was used to measure the peak height. This provided an additional check on the measured

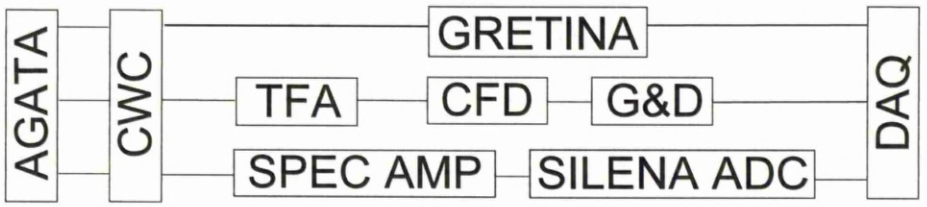

Figure 5.3: The electronics components used in the A006 Compton scan. The 36 differential signals from the segment preamplifiers were converted to single ended signals and passed directly to the GRETINA digitisers. Three copies of the core signal were produced at the converter box, one was passed to the GRETINA digitisers, one was used for an analogue energy measurement.

energy, which was included in the data written to disk every time the system was triggered. The remaining core signal was used as a trigger during coincident events to determine when the Data Acquisition System (DAQ) should pause to write the values from the GRETINA and Silena ADCs to disk. A combination of an ORTEC 474 Timing Filter Amplifier (TFA) and an ORTEC 584 Constant Fraction Discriminator (CFD) was used to determine if the appropriate energy threshold had been met. The logic pulse produced by the CFD was passed to a Phillips Scientific 795 Gate and Delay generator which provided the 50μs wide, 1V high pulse required to trigger the Silena ADC Controller (SAC).

The SAC fulfilled the dual function of propagating the trigger signal to all of the data collecting components and inhibiting further triggers while the system was in the process of writing data. If a trigger request signal was received while a disk write operation had not been completed it was ignored.

5.3 Signal processing

The electronics are designed to be able to deal with high count rates and preserving the fast leading edge of the charge sensitive preamplifier signals through digitization. Front-end processing digitizes the pulse through a digitizer box and then goes

through a preprocessing card where the charge pulses are tagged with channel IDs, trigger points, timestamps and energy information.

The preprocessing card implements a Field Programmable Gate Array (FPGA) to calculate pre-determined parameters, the timestamp, channel ID, the energy derived from the Moving Window Deconvolution calculation [37], the Moving Window Deconvolution trigger point and a baseline sample. In practice carrying out gamma-ray spectroscopy requires measuring many pulses in succession at a very high rate, occaisionally resulting in two pulses overlapping. To reduce the effect of this, the pulse width can be reduced to allow time for the first pulse to return to the baseline before the second pulse arrives. The signal from the preamplifier is passed through a CR high pass filter to introduce a decay time constant and an RC low pass filter to limit bandwidth and set the rise time to limit the noise bandwidth. Pulse shapers are often more sophisticated and complicated than a simple CR-RC shaper but all shapers contain a CR-RC shaper. Changing the time constants of the CR and RC sections changes the noise bandwidth, affecting the noise level and noise amplitude [38].

5.3.1 Digitiser

The aim of the digitiser is to provide an interface between the detector preamplifiers and preprocessing unit while maintaining sufficient resolution and sampling rate to extract information on the charge collection.

The digitiser units are located as close as possible to the detector cryostat in order to reduce the induced noise. The GRETINA digitiser card was used as it is optimised for the purposes of Pulse Shape Analysis (PSA) with HPGe detectors. Digital data acquisition was performed using four, 10-channel GRETINA digitisers. Each card combines 10 100MHz flash ADCs (10ns sample size) with 14bit precision, and a powerful FPGA to perform analysis on the digitised signal. In order to avoid aliasing effects, the input stage of each channel incorporates a Nyquist high-frequency filter [39].

The digitisers sample the signal continuously and write the results into an on-board

first-in first-out (FIFO) memory buffer. On receiving a trigger signal the cards pause the sampling process while the contents of the FIFO are written to disk. For this experiment we chose to write 128 samples of each signal for each event. A pre-trigger value can be set in the digitisers' registry, which tells the card how far back to look in its FIFO to account for the finite processing time of the triggering system. The value was tuned during set up to ensure the rising edge of the charge pulse was centred in the 128 sample range. The on-board FPGAs implement a series of digital signal processing (DSP) algorithms on each signal:

- leading edge discrimination
- constant fraction discrimination
- pole-zero correction
- trapezoidal filter [40]

The two discriminators each provide timestamps; the pole-zero correction accounts for the pre-amplifier decay and the trapezoidal filter, also known as a Moving Window Deconvolution (MWD), provides an accurate measure of the integrated charge, which is proportional to the energy deposited in the detector. The timestamps and energy values for all signals were written to disk along with the signal traces.
The trapezoidal filter is used to calculate the energy deposited from the signal trace. In the first stages of the analysis, the mean of the first 30 and of the last 30 samples in the trace were calculated. The difference between these was recorded as the Baseline Difference energy. Both methods of calculating the deposited energy were subject to the variation in gain of one channel relative to the next. This effect was accounted for by performing gain-matching, as discussed in detail in section 6.2, after the experimental run.

The digitization of the analogue signal is important for data storage and analysis. The analogue continuous signal distribution is transformed into a proportional set of discrete values. The conversions are carried out at a fixed clock frequency of 100 MHz producing 100 megasamples per second or one sample every 10ns.

Chapter 6

Detector Performance

6.1 Energy calculations

The energy is calculated using two algorithms; the first is the Moving Window Deconvolution (MWD) method; and the second is the Baseline Difference method. The energy for the Moving Window calculation is extracted by applying a trapezoidal shaping function to the amplitude of the preamplifier signal. This algorithm enables the precise energy information from the sampled data to be extracted with the minimum processing dead time.

This is carried out using:

- a time invariant digital filter
- a trapezoidal shaping function
- individual adjustment of shaping parameters
- adaptive shaping

The processed signal through the Moving Window Deconvolution algorithm can be seen in Figure 6.1

The Baseline Difference method uses the height difference between the start of the pulse and the end of the pulse to extract the energy. This is carried out through

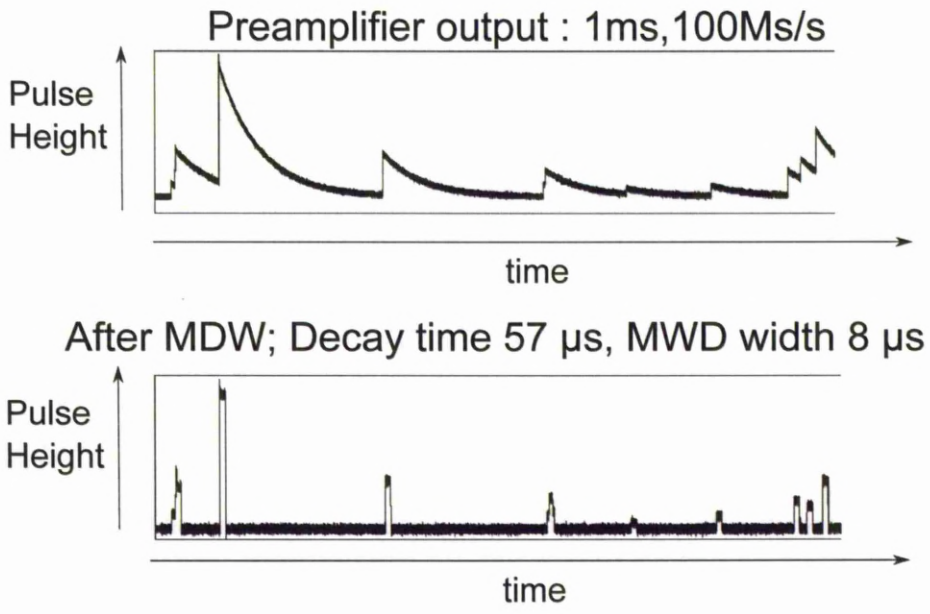

Figure 6.1: Effect on the signal using a MWD algorithm [37].

measuring the first and final 30 samples of the pulse to calculate the baseline. This was measured to be $\approx$ 4 keV. If the change from the beginning to the end of the trace was greater than three times the standard deviation of the baseline noise, the segment was considered to have been hit. There are two types of signals measured; real charge signals and image charge signals. To calculate if the signal represents a real or an image charge two calculations are carried out. To distinguish if the signal was a real or image charge pulse, a real pulse was defined if the difference between the start of the pulse and the end of the pulse was $>3\sigma$ of the baseline noise. An image charge pulse was defined if the integrated charge was >3 σ of the baseline noise, where 3σ is $\approx$ 12 keV.

6.2 Gain matching

Gain matching was conducted to calibrate all the segments within the detector. The gain matching was carried out on both the Moving Window Deconvolution and Base-

line Difference calculated energies.

To gain match all the segments a ^{241}Am and ^{152}Eu source were used to collect spectra for each channel across a range of gamma-ray energies from 59.5keV to 1408keV. The value returned by the cards and baseline difference were recorded for each peak. A least-squares fitting algorithm was then used to establish the relationship between the true deposited energy and values that were measured using each method. The raw spectra from all of the segments were fitted using the gf3 fitting program to align each segment channel number to the photopeak energy [41]. By using the following equation, coefficients were extracted so the energy values were binned correctly in each segment.

$$E = a + bx + cx^2 \tag{6.1}$$

where x is the channel number and a,b and c are coefficients.

6.3 Energy resolution

A spectrum of the total spectrum of the 36 segments added together can be seen in Figure 6.2.

Measurement of the detector energy resolution was carried out using digital electronics. This was carried out utilising the GRETINA digital cards. The energy resolution for the 36 segments and 1 core signal were measured individually at a gamma-ray energy of 1332.5keV using a ^{60}Co source. The energy resolution of these channels can be seen be seen in Figure 6.3.

The energy resolution can be seen to be around 2.75 keV FWHM at 1332 keV. The manufacturer's specification at 1332keV should be around 2.3keV . This measurement was also carried out using analogue equipment consisting of a Canberra 2026 spectroscopy amplifier with a $6\mu s$ shaping time and an ORTEC 927 multi-channel analyser. Figure 6.4 shows the energy resolution of the central contact was measured to be 2.27keV at 1332keV, which is within the manufacturers specifications. The

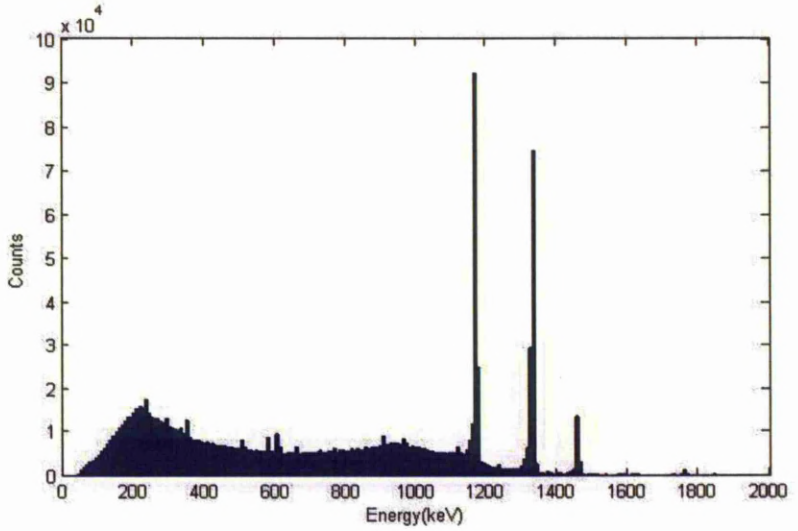

Figure 6.2: A sum energy spectrum of the 36 segments using a ^{60}Co gamma-ray source

analogue to digital conversion was carried out over 16k channels with an amplifier gain selected to spread the energies of interest over the full range of channels. From this it is concluded that the measured energy resolution is worse due to the use of digital electronics. This could be due to noise in the GRETINA cards. In an analogue amplifier there is usually one channel per card, however, in the GRETINA cards there are 10 input channels from the preamplifier resulting in noise within the cards. It may also be due to a less than optimal setup of the MWD trapezoid parameters resulting in the shaping time being incorrect.

6.4 Detector efficiency

The absolute photopeak efficiency measurement was carried out using a ^{152}Eu, ^{241}Am, ^{137}Cs and ^{60}Co source placed 25 cm from the front face of the detector. Figure 6.5 shows the variation of absolute efficiency with gamma-ray energy. The relative efficiency for a ^{60}Co source placed 25cm from the front face has been measured to be 83.69% $\pm$3.7%, the relative efficiency quoted by the manafacturer was 78.9%.

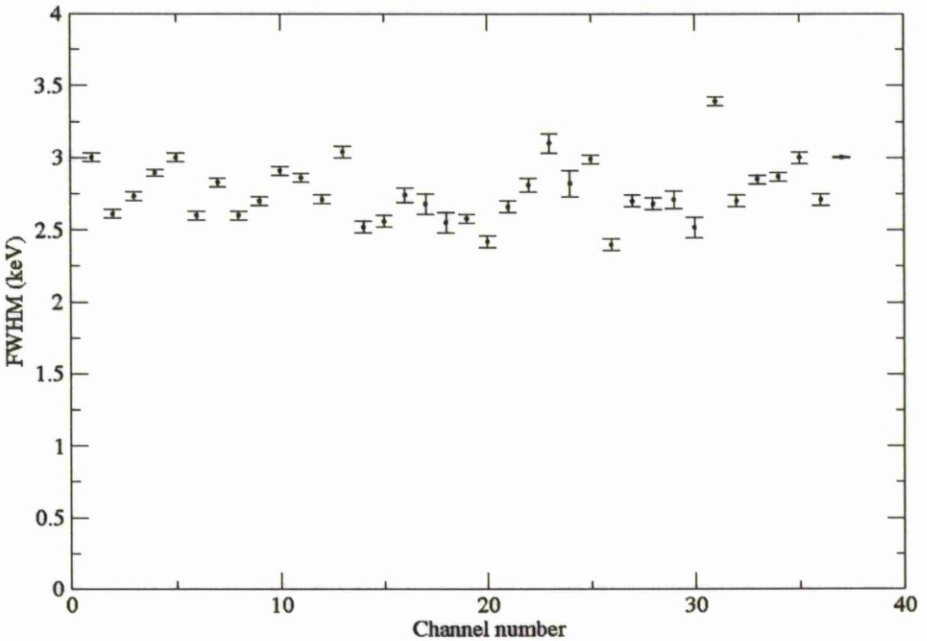

Figure 6.3: Energy Resolutions measured for all A006 segments and the core at 1332.5 keV using digital electronics.

6.4.1 Scattering probability between segments

It is important to have an understanding of Compton scattered events to perform Compton image reconstruction for which two interactions within the detector per event are required. The number of interactions that occur within the crystal are referred to as fold. There are two connotations of fold, the first is referred to as true fold and the second is referred to as segment fold. These can be seen in Figure 6.6. The true fold refers to the number of gamma-ray interactions that have occurred within the crystal so deposition 1 and deposition 2 will both be a fold 2 event. Segment fold however refers to the number of segments that the deposited energy per event is shared over. Referring to Figure 6.6 deposition 1 would be a fold 1 event and deposition 2 is a fold 2 event. The term fold used from here refers to the segment fold, referring to the number of segments that record an energy deposition per event.

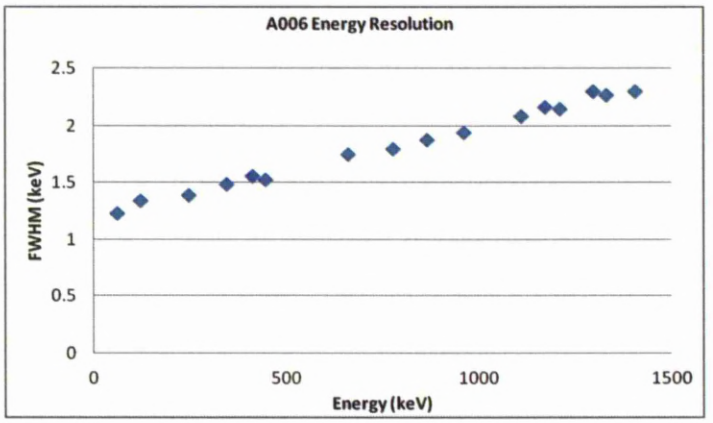

Figure 6.4: Energy resolution for photopeaks from a mixed ^{152}Eu, ^{241}Am, ^{137}Cs and ^{60}Co source placed 25 cm from the front face of the detector

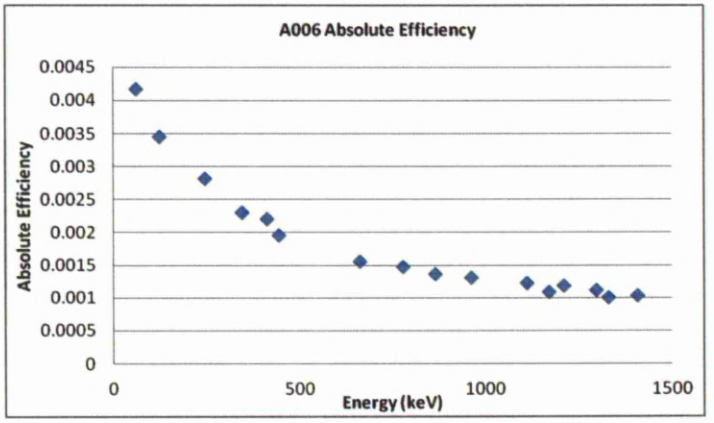

Figure 6.5: The absolute photopeak efficiency for a ^{152}Eu, ^{241}Am, ^{137}Cs and ^{60}Co source placed 25 cm from the front face of the detector

The fold number for 1332 keV ^{60}Co events can be seen in Table 6.1. This table shows that it is most likely that the gamma ray will deposit its energy in one segment, with decreasing probabilities for higher fold events. The size of the segment which is 2 cm at it's widest point, plays a factor in the large number of fold 1 events, as an event if scattered is likely to be absorbed in the same segment. This is deliberate for

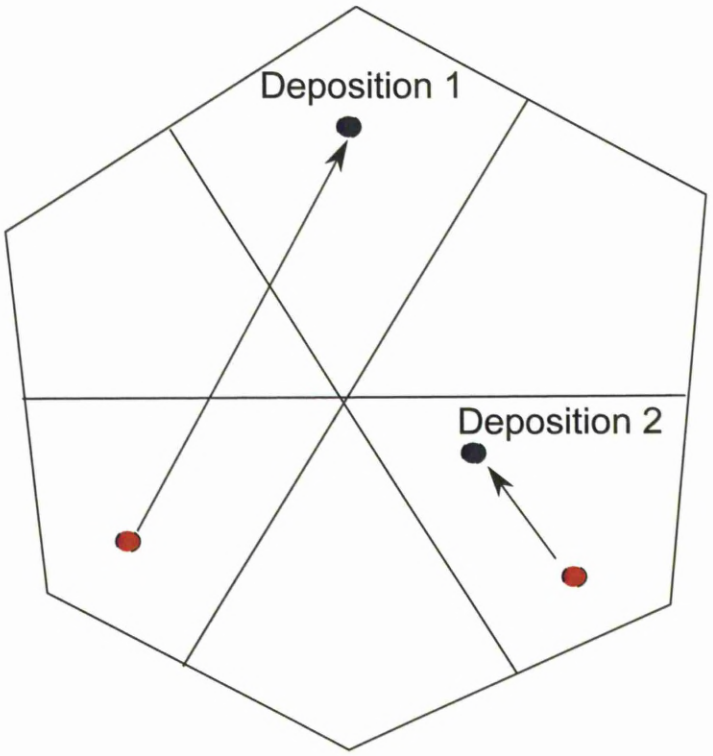

Figure 6.6: Figure to explain fold. The true fold refers to the number of gamma-ray interations that have occured within the crystal, deposition 1 and deposition 2 will both be a fold 2 event. Segment fold however refers to the number of segments that the deposited energy per event is shared over, referring to Figure 6.6 deposition 1 would be a fold 1 event and deposition 2 is a fold 2 event.

the AGATA detectors as total energy deposition is required.

The fold 2 events are of interest for this thesis. Higher folds can be used if the full energy is not known by computing the correct energy by observing the positions and energy losses of each interaction that a gamma ray undergoes. However, this is not applicable in this thesis as the energies are known and the volume of the crystal means that there is a high probability that complete gamma-ray deposition will occur.
A condition was implemented for the fold 2 events. For events that met the condition it is of interest to see the position of hit segments relative to each other.

Table 6.1: Table to show the number of hit segments per event for a ^{60}Co gamma-ray source

Fold	Number of events	Percentage of total
1	11575449	66 %
2	4022262	23 %
3	1339998	18 %
4	394741	2%

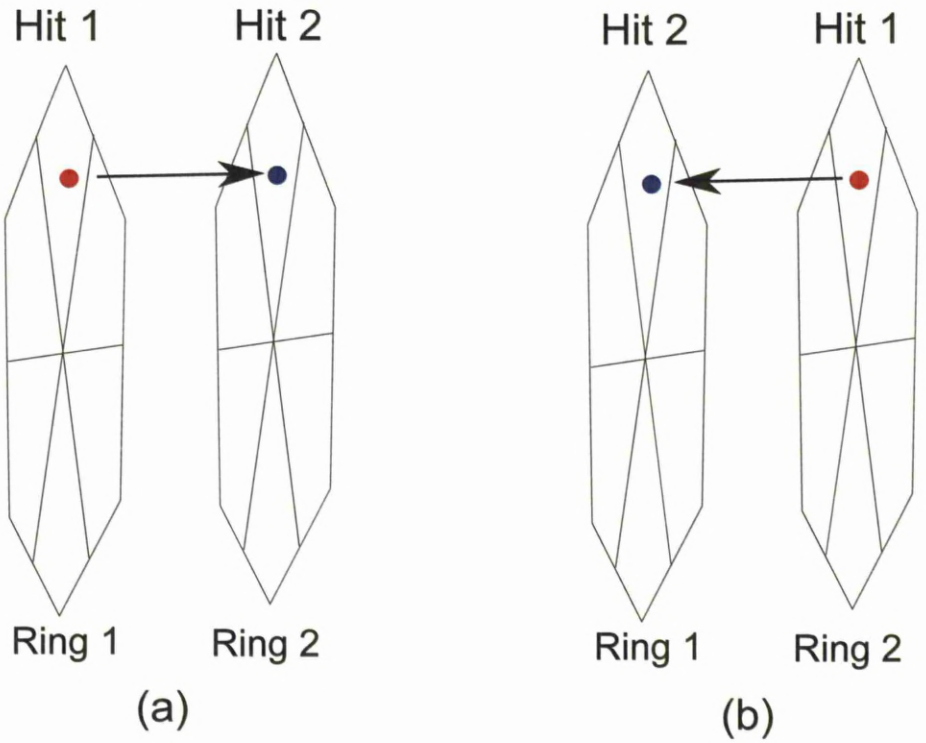

Figure 6.7: Figure to show probable scatter and absorber hits for the same event

It is not known in what order the hit events occur, see Figure 6.7. It is possible that case *a* could occur, with a scatter from ring 1 into ring 2. Also for the same event case *b* could occur where the scatter is in ring 2 into ring 1. For the purposes of this analysis of the relative positions of hits it is assumed that the lowest segment number that is hit is the first interaction the segment numbering can be seen in Figure 5.2.

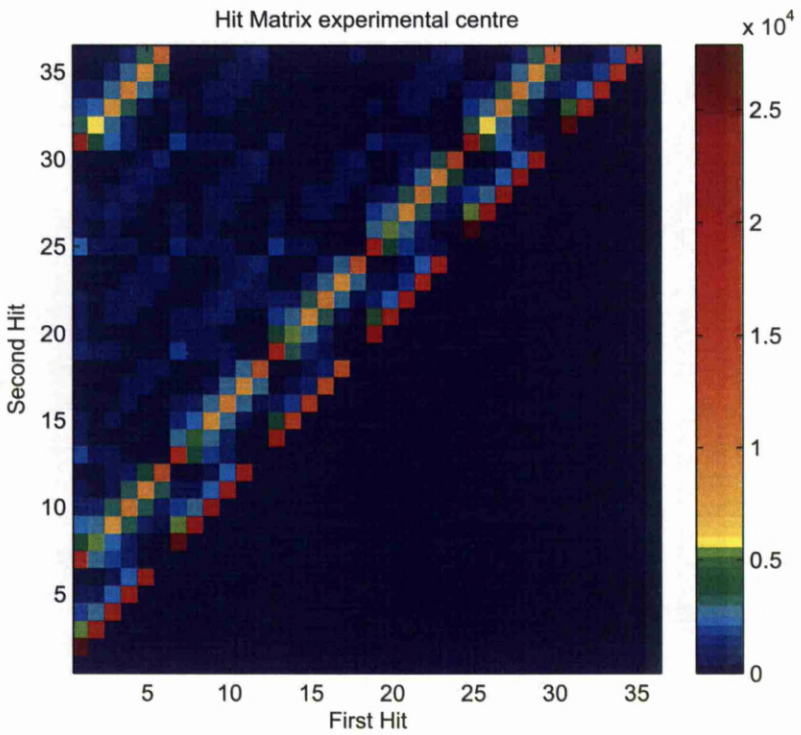

Figure 6.8: The segment number of the first hit segment is plotted against the segment number of the second hit segment

The segments in ring 1 are known as the scatter segments and the segments of rings 2 to 6 are the absorber segments. In Figure 6.8 the segment number of the first hit segment is plotted against the segment number of the second hit segment. Using this plot and cross correlating this against Figure 5.2 it can be seen that the nearest neighbour either side in the same ring and the segment behind is the second hit, this is shown as diagonal lines of increased intensity.

6.4.2 Experimental scatter angle results

The maximum angle possible for a gamma ray to scatter from the scatter detector into the absorber detector is 73.8° geometrically assuming a scatter from segment 1

into segment 14. The most probable angle of scatter of a gamma ray can be found through the energy deposited during an interaction in the scatter detector. Figure 6.9 shows the calculated angle of scatter for each keV of energy deposited within the AGATA A006 scatter segments and Figure 6.10 shows the energy deposited in all of the first hit segments added together. Figure 6.11 shows that the most probable energy deposited is $\approx$ 230 keV in the scatter segment. This equates to a scatter angle of $\approx$ 20 °.

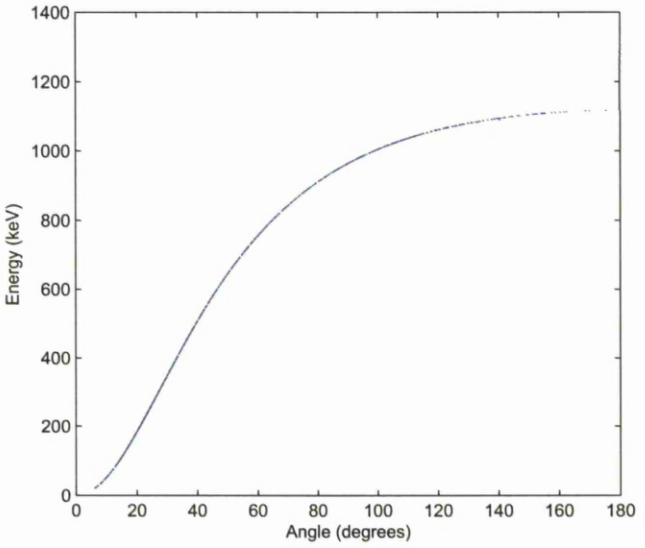

Figure 6.9: This plot shows the calculated scatter angle per keV of a gamma ray Compton scattering in a segment of the detector.

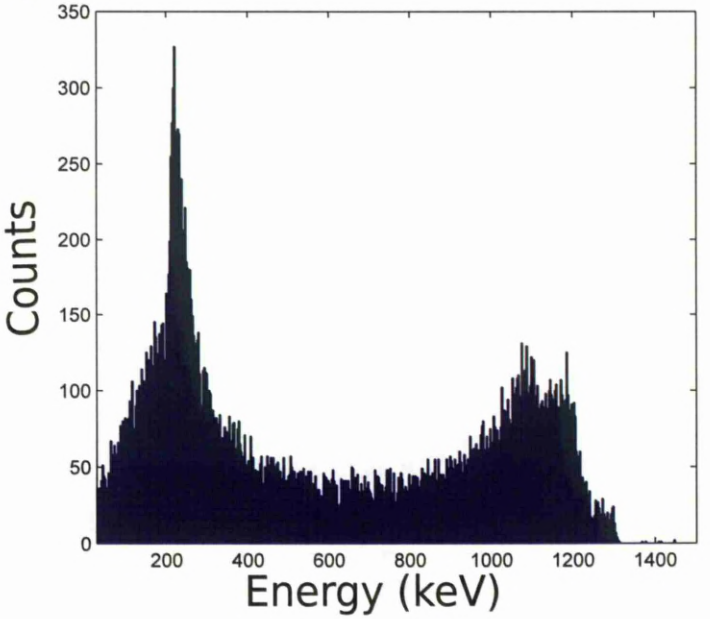

Figure 6.10: Energy deposited in the scatter segment. It can be seen that $\approx$ 230 keV is the most probable energy deposited within the scatter segment.

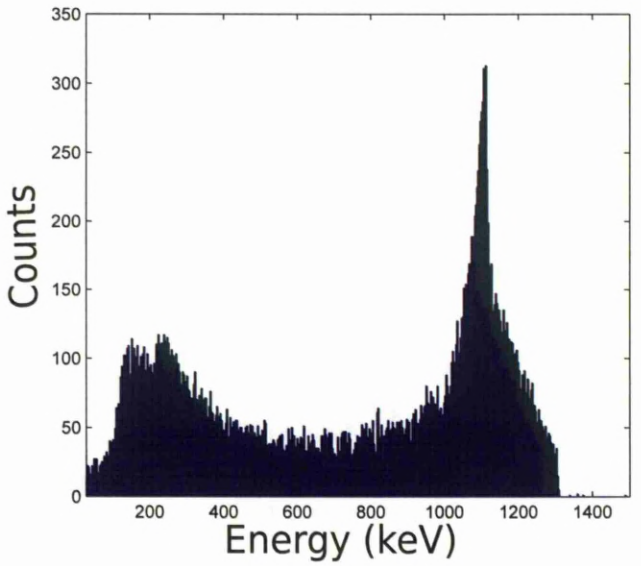

Figure 6.11: Energy deposited in the absorber segment. It can be seen that $\approx$ 1100 keV is the most probable energy deposited within the absorber segment.

Chapter 7

Signal analysis of the AGATA A006 detector

7.1 Pulse shape analysis for Compton image reconstruction

The position resolution of a detector can be improved by the utilising pulse shape analysis. Signals from a semiconductor radiation detector contain not only the information about the amplitude of the pulse but also information regarding the position of interaction is contained within the real and transient charge signals. The real charge contains information on the energy and the radial position of the interaction, while the transient image charge contains information on the azimuthal position of the interaction.

The precision of pulse shape analysis (PSA) to be used as a tool for the extraction of interaction positions will be investigated. It is important to have detailed understanding of the pulse shapes to have accurate gamma-ray tracking. The combined response of the 36 segments and the core is characteristic of each position within the detector.

Pulse shape analysis makes use of the signal shapes observed as the charge pulse

from the gamma-ray interaction contains information about the interaction. There are two different approaches to position determination; parametric PSA and library PSA(BASIS).

Parametric PSA makes use of the rise time and image charge asymmetry to locate the position of interaction, as will be discussed further in 7.2.

7.2 Parametrisation of signals

The signal contains information regarding the position of interaction, the radial information is contained within the within the rise time of the signal[42] [43]. The signal is parametrised into two parameters T30 and T90. these represent the time taken for the signal to rise from 10 % to 30 %, and 90 % of the full magnitude. Figure 7.1 describes this graphically.

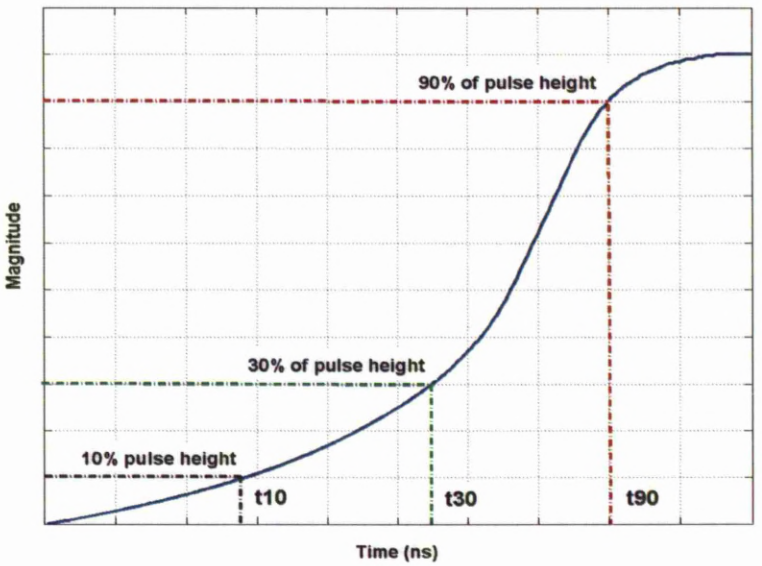

Figure 7.1: An example of a pulse shape from a semiconductor detector. The magnitude is plotted as a function of time and shows the t10, t30 and t90 parameters of a preamplifier pulse.

The T90 value provides a measure of the time required for full charge collection while the T30 risetime is more closely related to the charge carrier with the shortest drift distance to its collecting electrode. The T30 risetime is therefore more sensitive to the point of interaction, reflecting the movement of charge carriers local to the interaction site [44].

To determine the azimuthal position the transient charge signals are analysed and Figure 7.2 shows an example of this. The signal induced on the neighbouring segments gives information on the position of interaction. The sizes of the transient signals in neighbouring segments in the same ring and adjoining rings will give the azimuthal angle of interaction. The total amount of charge induced on each contact from the transient image charge is given by the area under the transient pulse.

Both electrons and holes are in motion during charge collection, resulting in positive and negative values of induced charges. Either the positive or negative charge carrier will dominate the charge signal depending on the proximity of the interaction to the contacts. This results in either one or the other charge carrier dominating the polarity. If neither polarity dominates a bipolar signal can occur.

To calculate the area under these bipolar signals the modulus of the induced charge on each neighbouring segment is used to calculate the area of the signal this is calculated by using equation 7.1

$$ICArea = \frac{Area_{clockwise} - Area_{anticlockwise}}{Area_{clockwise} - Area_{anticlockwise}} \tag{7.1}$$

where $\text{area}_{anticlockwise}$ refers to the segment in the x-y plane anticlockwise from the interaction segment and $\text{area}_{clockwise}$ refers to the segment in the x-y plane clockwise from the interaction segment.

7.2.1 Radial discrimination

The risetime within an AGATA detector can be seen in Figure 7.3. This shows the average T30 and T90 risetimes as a function of x,y position for each ring of the AGATA S002 detector. Radial discrimination is calculated from the distribution of

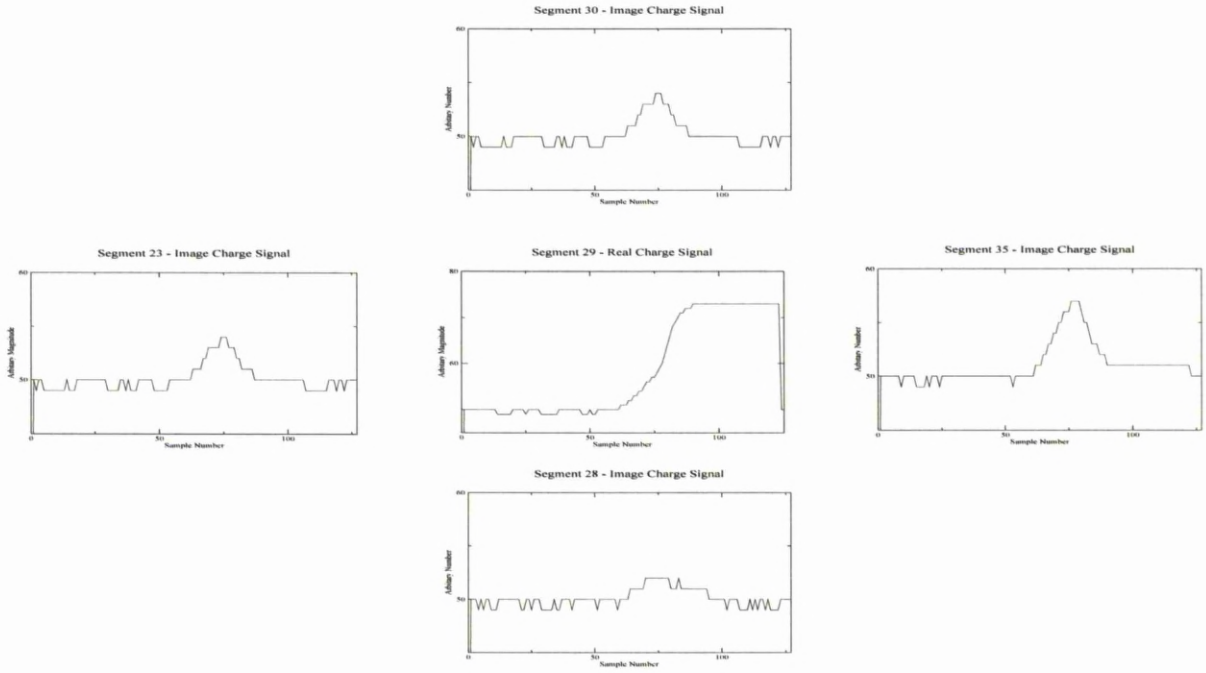

Figure 7.2: Example of real charge pulse and image charge pulses during a gamma-ray event

the risetime. Figure 7.4 shows the distribution of the risetime for the data taken with the A006 AGATA detector. The Figure shows a T30 vs T90 matrix of all the events that occur within each segment. The T30 vs T90 values, as discussed in section 7.2, refer to the time taken to reach 30% and 90% of the total charge collection respectively.

Risetime as a function of position has been investigated previously by Nelson [45] these can be seen in Figure 7.3. The minimum T90 values are found at intermediate radii, where the electron and hole drift times are similar. At positions either side of this the time is dominated by the collection of the carrier with the longest drift time. The longest T90 values are found near regions of weak field in ring 1, and at the extremes of radii in rings 5 and 6, where the total drift distance is longest.

For quick rise times of T30, it can be seen that there are longer T90 values, this would be an interaction that has occurred near the core. The electrons will flow

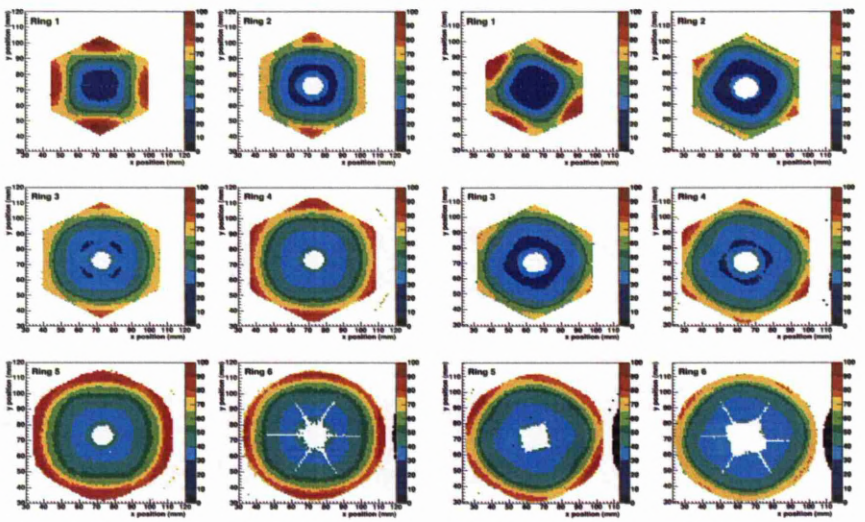

Figure 7.3: a) Average T30 risetime as a function of x,y position for each ring of S002. The x and y axes denote the respective x and y positions of the collimator in millimetres. The z axis represents the T30 risetime and has units of nanoseconds. b) Average T90 risetime as a function of x,y position for each ring of S002. The x and y axes denote the respective x and y positions of the collimator in millimetres. The z axis represents the T90 risetime and has units of nanoseconds.[45]

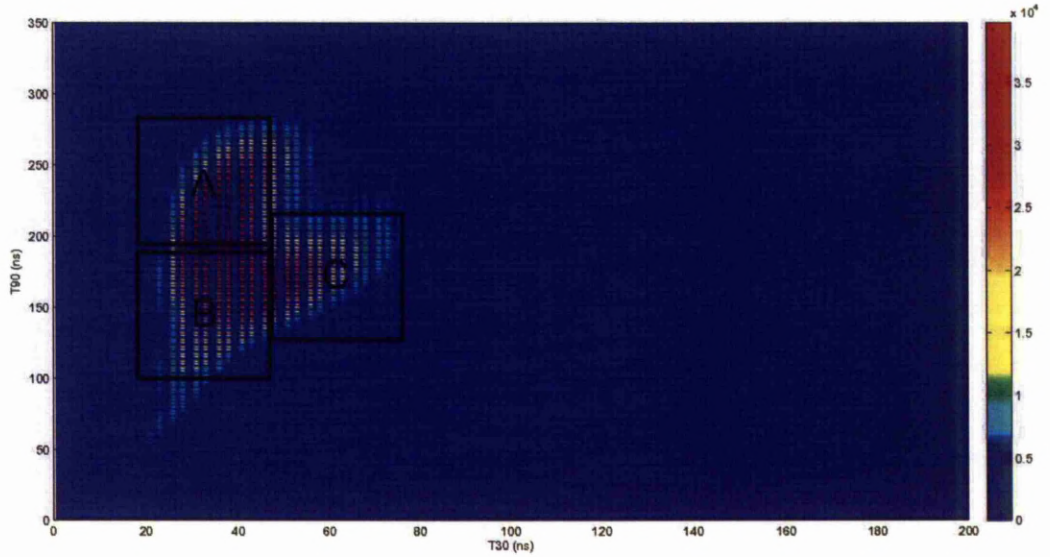

Figure 7.4: The distribution of the risetime for the data taken with the A006 AGATA detector. The Figure shows a T30 vs T90 matrix of all the events that occur within each segment.

to the core anode and the holes flow to the outer cathode. The T90 values will be dominated by the holes due to charge trapping and T30 values are dominated by electrons. This can be seen in Figure 7.4. As the T30 collection times increases, the radial interaction point increases the T90 collection time decreases to a minimum. This describes an interaction where neither the electrons nor holes dominate the charge collection. This suggests an interaction point towards the radial centre of the segment. When the interaction position occurs near the outer areas of the segment, hole collection dominates and electron collection takes longer, resulting in increasing T30 and T90 values [46][47][48].

Three gates are set to describe these situations, these are shown in Figure 7.4:

- gate A describes a situation where radial position of interaction occurs near the inner edge of a segment. The collection times for T30 are short, with large T90

values.

- gate B describes a situation where the radial position of interaction occurs near the centre of a segment, where the electrons and holes contribute equally to the charge collection
- gate C describes a situation where the radial position of interaction occurs near the outer edge of a segment, so the collection time of the electrons (T30) is long.

7.2.2 Azimuthal discrimination

The response of the image charge asymmetry can be seen in Figure 7.5 to have approximately linear dependence for a large part of the detector. With this being the case it is possible to apply linear gates to improve the information regarding interaction position within the segments

To calculate the azimuthal position of interaction, the transient image charge signal induced on neighbouring segments was analysed. To decide if the pulse was a real or image charge, the noise level of the pulse shape is calculated as the standard deviation, σ of the baseline fluctuations.
To distinguish if the signal was a real or image charge pulse, a real pulse was defined if the difference between the start of the pulse and the end of the pulse was $>3\sigma$ of the baseline noise. An image charge pulse was identified if the integrated charge was $>3\sigma$ of the baseline noise. Equation 7.1 calculates the ratio of the signals in the segments either side of the segment of interaction .

Three different situations can be used to describe image charge asymmetry:

- The first two situations can describe where the point of interaction is closer to one neighbouring segment than the other, resulting in a larger transient image charge signal on the segment closer to the interaction position.
- The last situation can describes a situation where the position of interaction occurs in the centre of the segment, resulting in an equal image charge signal on each segment either side.

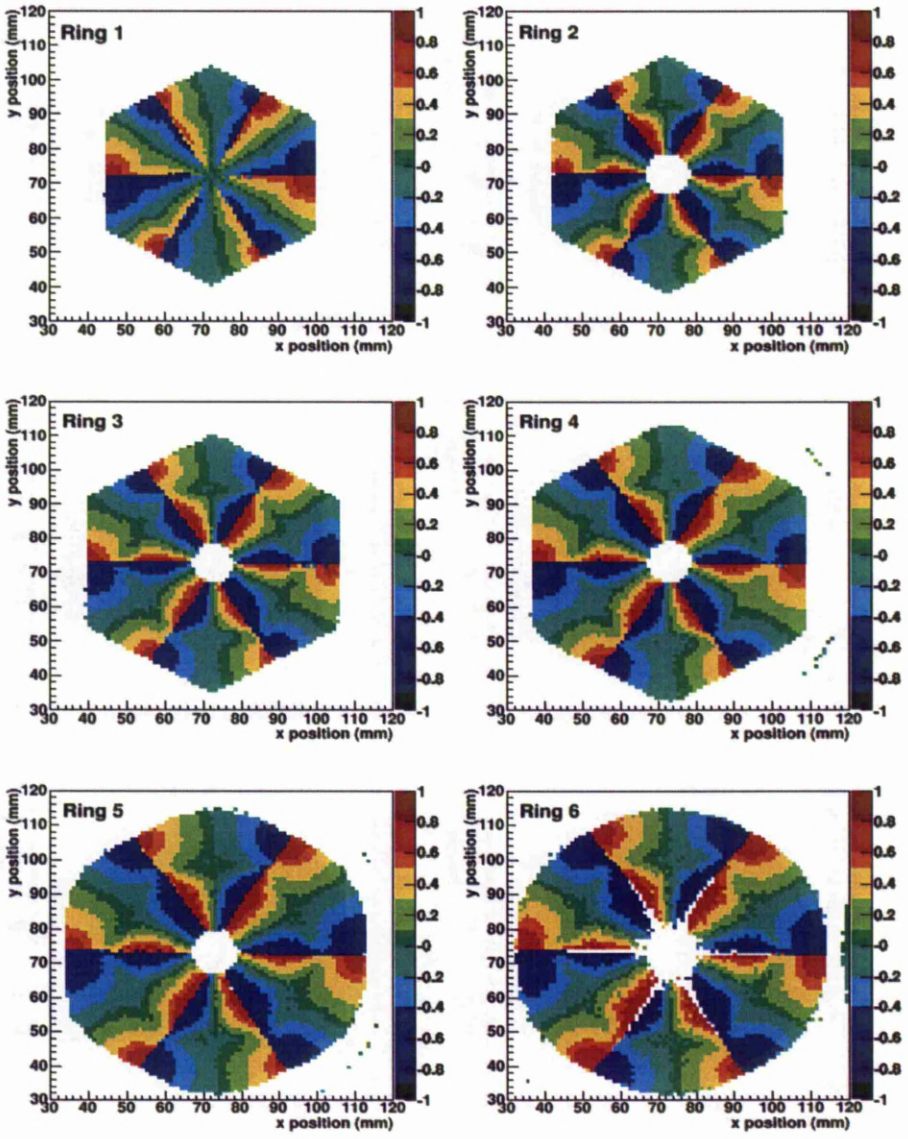

Figure 7.5: Average image charge asymmetry from neighbouring segments as a function of x,y position for each ring of S002 [45].

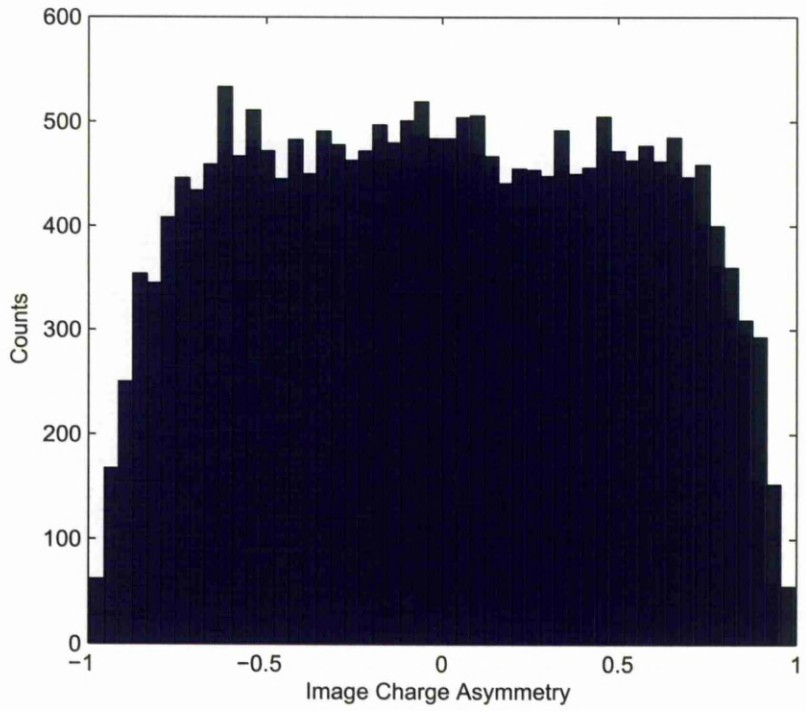

Figure 7.6: Calculated image charge asymmetry of segment 1

The image charge asymmetry for experimentally collected data in segment 1 can be seen in Figure 7.6. Any variations in the image charge asymmetry as a function of position will be minimised later by splitting the segment azimuthally into three sectors. This will be discussed in section 8.4

Chapter 8

HPGe Compton Image Reconstruction

8.1 Introduction

The AGATA detector provides excellent energy resolution, with an average of $\approx$ 2.7keV at 1332 keV for all segments, but due to the segment sizes it has relatively poor position resolution. The effect of this will be be investigated in this chapter. Compton image reconstruction will be carried out using the centre of the segment as the interaction position, to assess whether this information is sufficient for image reconstruction. Parametric pulse shape analysis will then be implemented to improve the position of interaction resolution and then the reconstructed image will be assessed.

8.2 Experimental setup

The experimental data were obtained using the AGATA A006 asymmetric detector, with the detector electronics setup as shown in the previous section. Two ^{60}Co gamma-ray sources sources having 4.3 kBq and 4.9 kBq were positioned 100 mm away from the front face of the detector.

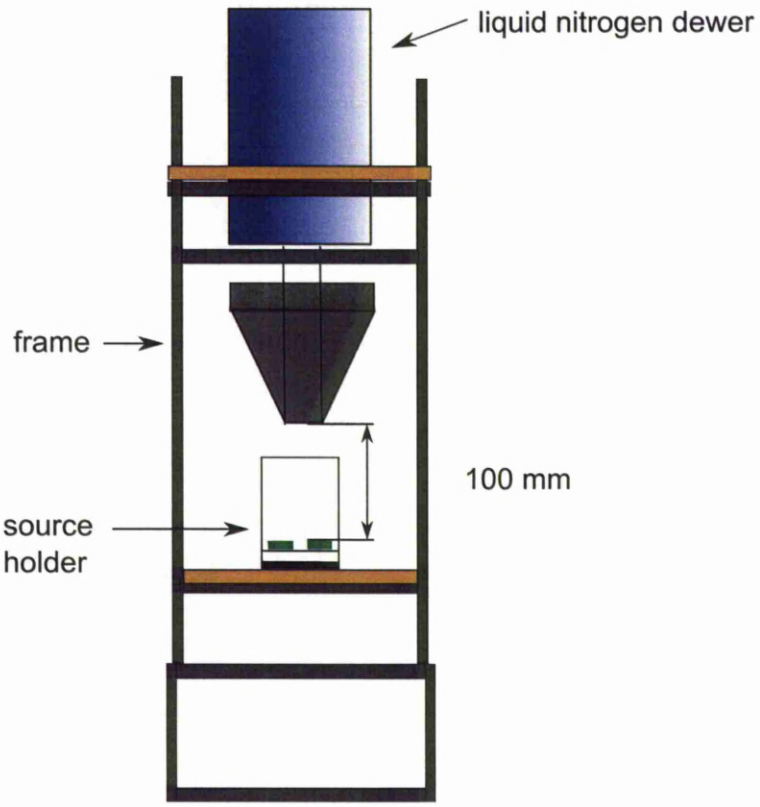

Figure 8.1: Experimental setup for the collection of Compton data using the AGATA A006 detector

The ^{60}Co gamma-ray sources were positioned within their holders 12.5 mm away from each other.

8.3 Data pre-sort

The raw data collected from the experimental setup were pre-sorted using the MTSort programming language to provide analysis of the pulse shapes and extract the raw data in a readable format. The steps required to do this can be seen in Figure 8.2. A C code and MTSort code were read into the MTSort package. The C code provided

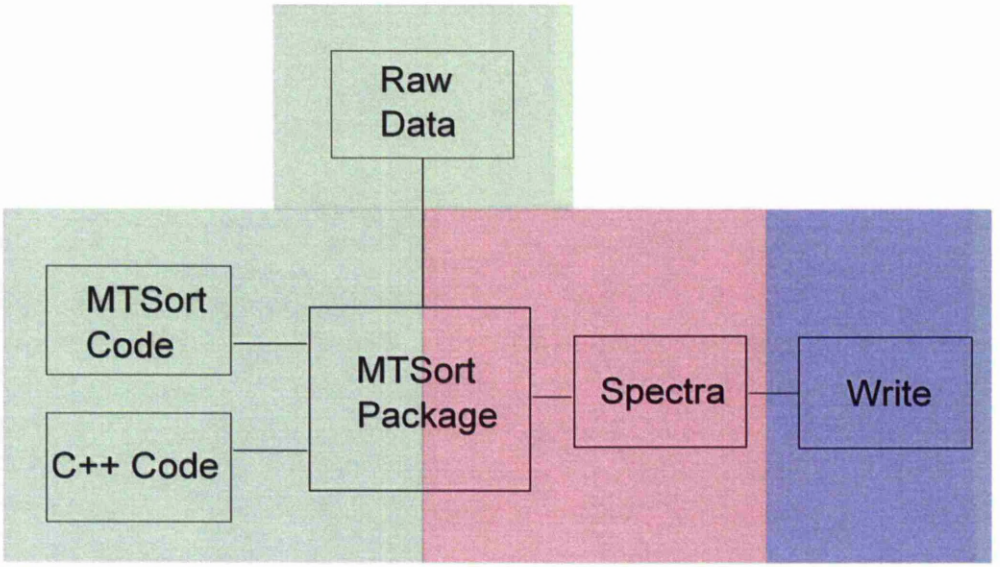

Figure 8.2: This figure describes the steps required for the pre-sort of the raw data. The area shaded in green shows the items required to be read into the MTSort package. The area shaded in red is the analysis of the items read in by the MTSort package. The area shaded in blue is the data extracted from the MTSort package that is written to file. [49]

analysis of the pulse shapes while the MTSort code used in conjunction with it enabled the data to be put into a readable format to analyse the pulse shapes and extract data. The sort extracted the following information from the pulse shapes:

- energy
- fold
- segment hit
- area of image charge pulse in adjacent segments

These data were further analysed in the MTSort program to output data from the MTSort program into the format below:

- first hit segment

- energy deposited in segment 1
- second hit segment
- energy deposited in segment 2

8.4 Calculation of segment centres

The centre of the segment has been calculated with the GEANT4 simulation program, described in greater detail in chapter 9. The AGATA GEANT simulation code, (see chapter 9) was developed to produce realistic simulated data for the AGATA collaboration. Information regarding the segment of interaction, exact x, y and z coordinates and the energy deposited within the crystal volume can be extracted. The position of interaction for 5 million events has been plotted. Using these positions of interaction, the geometry of the detector can be calculated. A condition on a segment can be added enabling a precise geometry for each segment to be analysed easily.
The simulated segment geometry has been analysed to calculate the segment centres as it provides a data set of possible positions within the detector and thus in a segment.
Due to the complicated shape of the AGATA A006 detector, to calculate the centre of the segment of a coaxial, non-symmetrical detector, the Cartesian values were transformed into polar coordinates.

Figure 8.3 shows segment 7 transformed into polar coordinates, where the x-axis represents the azimuthal angle and the y - axis represents the radial position in millimeters.
The angle values and radial positions were then summed and divided by the total number of events to calculate the mean value. The two mean azimuthal and radial positions are transformed back into Cartesian coordinates to give the centre of the segment. This was then applied to all segments to calculate the segment centres for the whole detector.

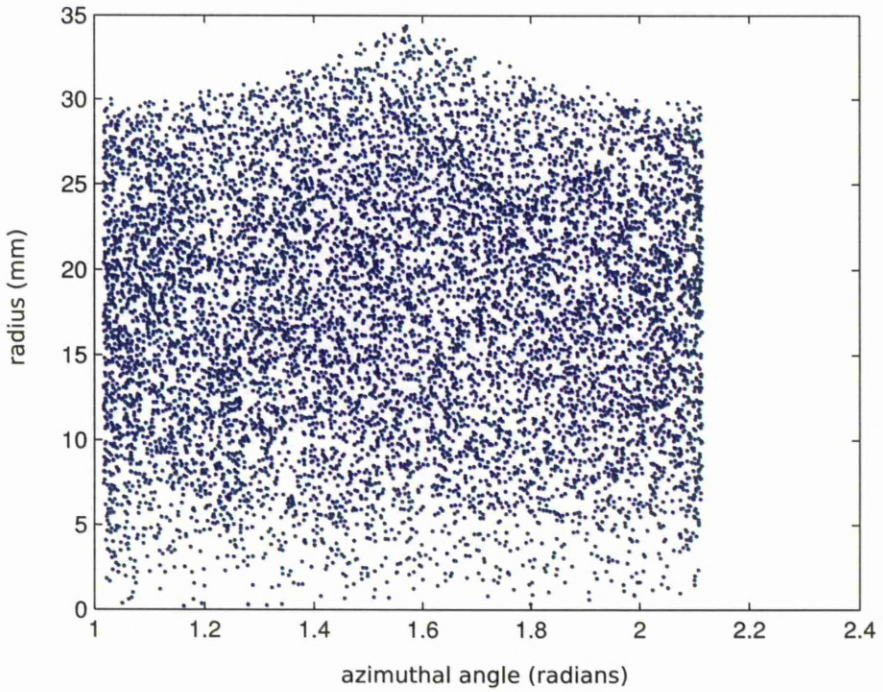

Figure 8.3: A scatter plot to show segment Cartesian coordinates transformed into polar coordinates

Figure 8.4 shows the x, y and z positions for the segment centres for the AGATA A006 detector. The MATLAB programming language was used to read in the calculated x, y and z coordinates for each segment and the experimental data. A code was written so that the segment number of the experimental data was then compared with the associated x, y and z coordinate for that segment and this was outputted in the following format:

$$Z_{1,centre}, Y_{1,centre}, X_{1,centre}, E_1, Z_{2,centre}, Y_{2,centre}, X_{2,centre}, E_2.$$

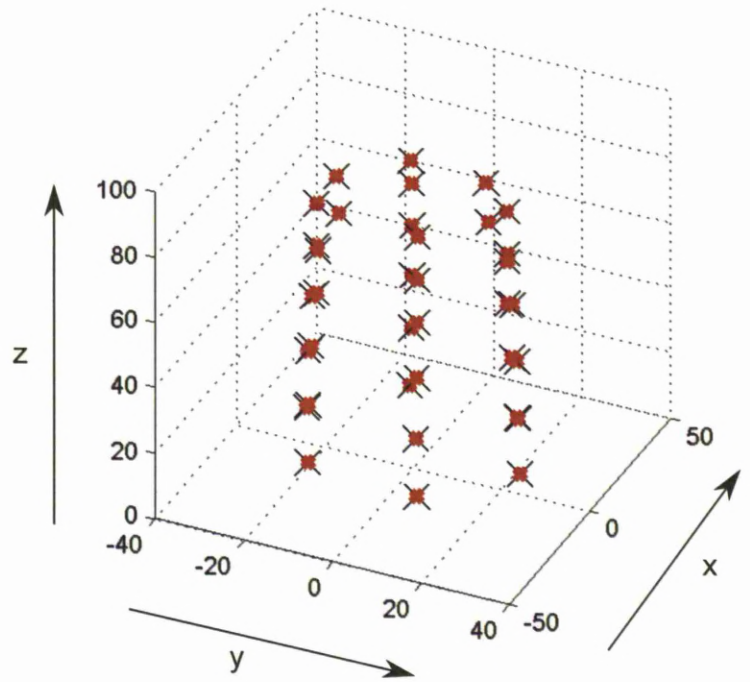

Figure 8.4: A 3-D scatter plot to show segment centres for an asymmetric AGATA detector

8.4.1 Experimental Results; Position of interaction segment centre

The outputted data describing the position of interaction as the centre of the segment were read into the Compton Image Reconstruction code described in section 3.6. The information on the energy and position of interaction was used to create an ellipse at a distance of 100 mm from the front face of the detector. In total 476877 fold 2 events were incident on the detector, of which 122768 were reconstructed into the z-plane 100 mm from the front face of the detector. The Compton - reconstructed image of the two ^{60}Co point sources using the segment centre as the position of interaction can be seen in Figure 8.5.

The reconstructed image has an offset of 300 mm and a ring effect can be seen. The

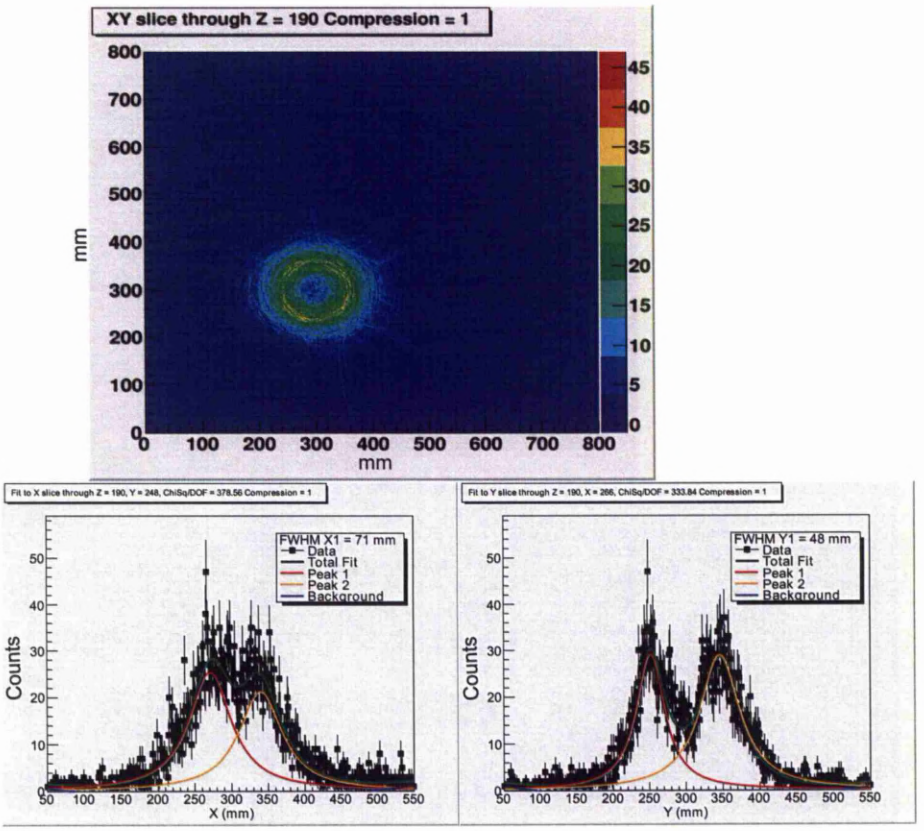

Figure 8.5: Image slice of two 1332keV ^{60}Co points source located 100mm from the front face of the detector, utilising the segment centre as the position of interaction. The image FWHM values for these peaks are 70 ± 5 mm at 271 mm and 71 ± 6 mm at 339 mm in the x profile. In the y profile the image FWHM values for these peaks is 47 ± 3 mm at 251 mm and 65 ± 3 mm at 346 mm.

x and y profile has been fitted using a Lorentzian peak fit and quadratic background fit utilising a least squares minimisation fit. There are two major peaks seen in the x and y profiles, at 271 ± 2 mm and 339 ± 2 mm in the x profile and 251 ± 1 mm and 346 ± 1 mm in the y profile. The image FWHM values for these peaks are 70 ± 5 mm at 271 mm and 71 ± 6 mm at 339 mm in the x profile. In the y profile the image FWHM values for these peaks is 47 ± 3 mm at 251 mm and 65 ± 3 mm at

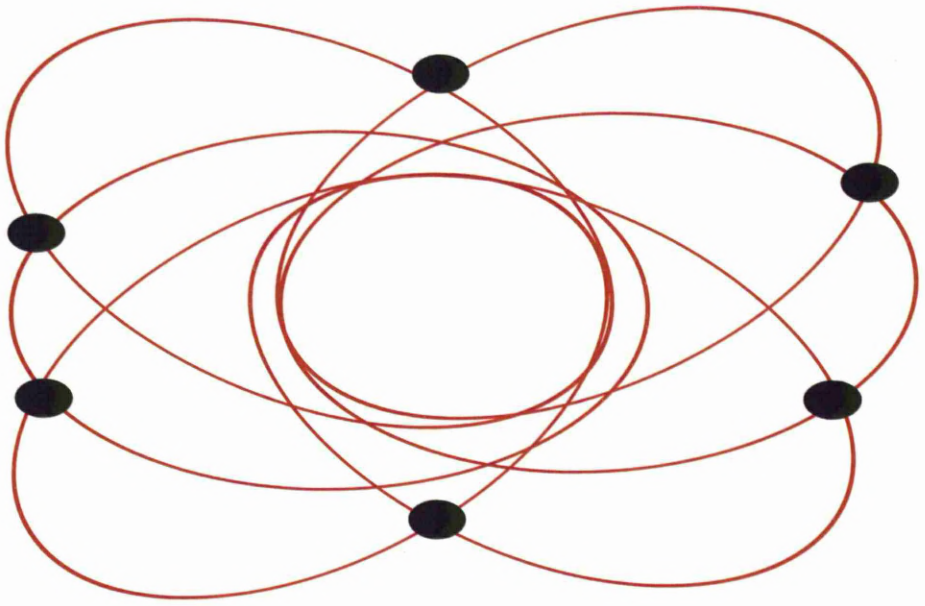

Figure 8.6: An explanation of the observed ring effect can be seen in this figure, six reconstruction positions have a high probability for interaction

346 mm. This does not provide precise information about the position of interaction at 100 mm away from the front face of the detector.
The ring effect can be explained by comparing the reconstructed image to the hit matrix shown in Figure 6.8. Figure 6.8 implies that it is highly probable that a scatter from the first hit segment will be absorbed in the segments behind it. This is predicted by the Klein-Nishina distribution for a 1332keV gamma ray. Therefore six reconstruction cones have a high probability of being constructed. This was analysed by using just 100 experimental Compton image reconstructed cones. Figure 8.6 shows the cone pattern observed.

To correct for this ring effect, events that were scattered into the segment behind, during a fold 2 event, were removed from the reconstructed data set. This data set was then read back into the Compton image reconstruction code, the image produced can be seen in Figure 8.7.

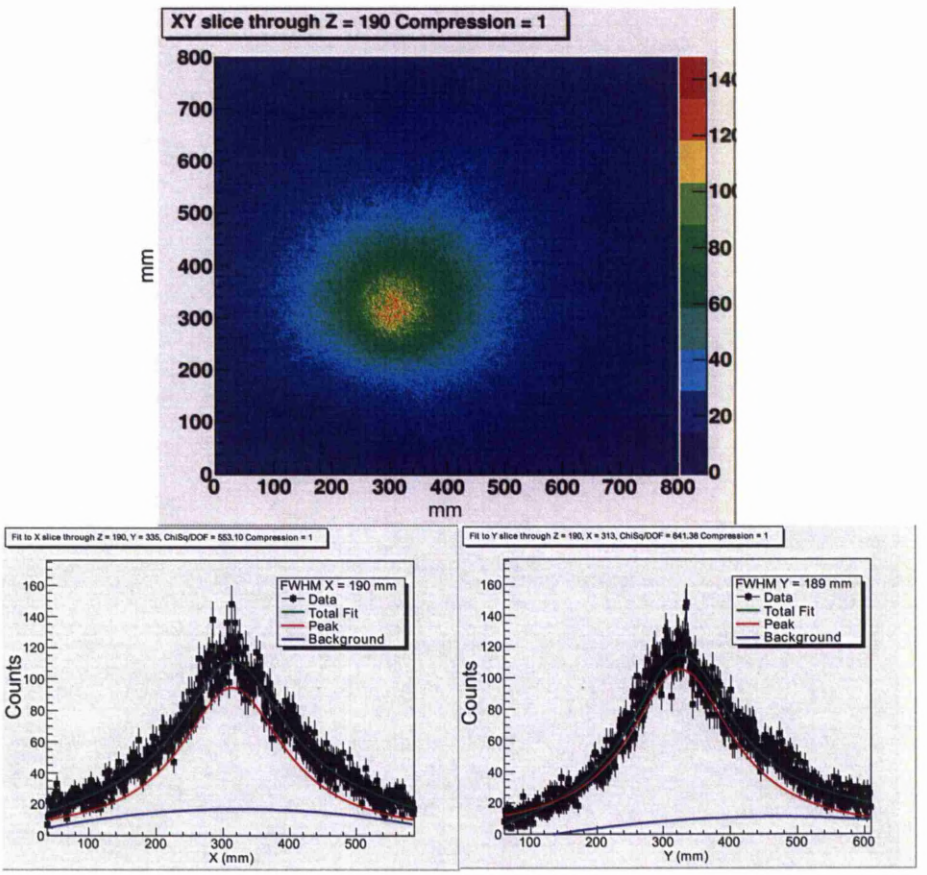

Figure 8.7: Compton image reconstruction of two 1332keV ^{60}Co sources located 100mm from the front face of the detector with events scattered directly behind removed. The image FWHM values for these peaks are 190 ± 10 mm at 314mm and 188 ± 9 mm at 326 mm.

The reconstructed image has an offset of 300 mm and the ring effect has been removed, with the position of the source at 100 mm away becoming clearer. The x and y profile has been fitted using a Lorentzian peak fit and quadratic background fit utilising a least squares minimisation fit. The image has a greater precision in the position of interaction compared to Figure 8.5. One major peak can be seen at 314 ± 1 mm in the x profile and 326 ± 1 mm in the y profile. The image FWHM values for these peaks are 190 ± 10 mm at 314mm and 188 ± 9 mm at 326 mm. The values for

image FWHM are greater than the previous reconstructed data set, which included scatters into segments behind, but from the reconstructed image this is a much more valid measurement of the position of interaction at 100 mm away from the front face of the detector.

8.5 Image reconstruction utilising pulse shape analysis

A grid of 9 sectors was created as illustrated in Figure 8.8. Three conditions are created for the radial and azimuthal positions within each segment of the detector. Discrimination between the 9 sectors was carried out through analysis of the risetime and image charge asymmetry values.

The rise time condition artificially split the segment into three radial positions through analysis of the real pulse using the three gates described in section 7.2.1. Interactions that occured near the core were assigned rise time position 1, interaction that occured near the centre of the segment were assigned risetime position 2 and those towards the edge of the segment were assigned rise time position 3.

The asymmetry condition artificially split the segment into three azimuthal positions. Each segment is assumed to cover a 60° angle. The segments were therefore split into three equal 20° gates.

The image charge asymmetry value calculated in section 7.2.2 gives a distribution of numbers between -1 and 1. -1 refers to an interaction that has taken place close to the segment anti-clockwise and 1 refers to an interaction that has taken place close to the segment clockwise. This distribution is then multiplied by 30 to spread the distribution over a 60° angle.

The conditions required to meet these gates are:

1. if the experimental image charge asymmetry is between -30 and -10 an azimuthal position of 1 is assigned.

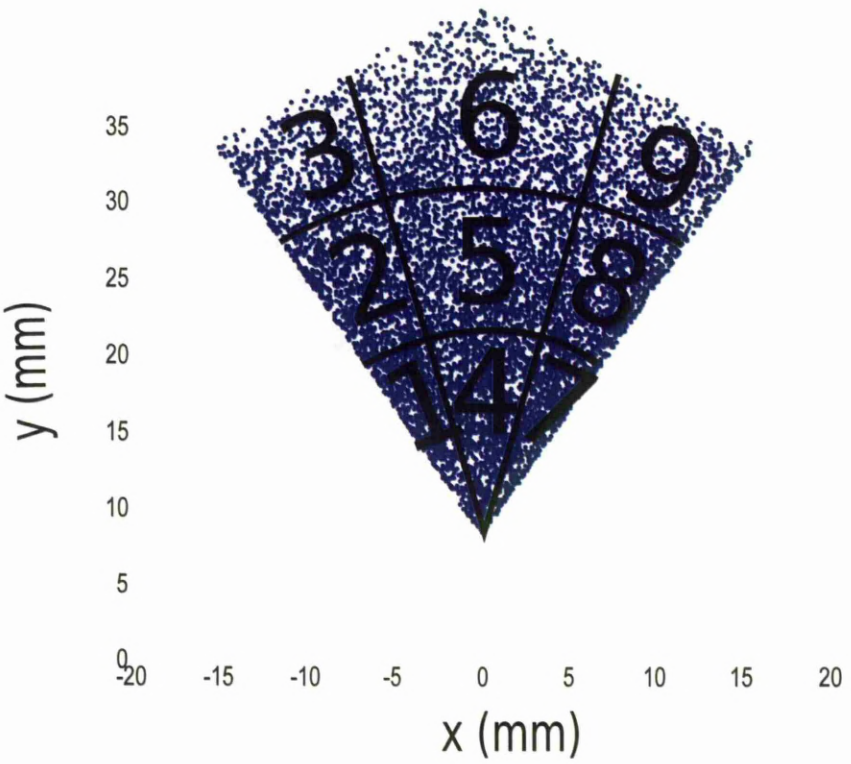

Figure 8.8: Grid positions setup for Pulse Shape Analysis.

2. if the experimental image charge asymmetry is between -10 and 10 an azimuthal position of 2 is assigned.

3. if the experimental image charge asymmetry is between 10 and 30 an azimuthal position of 3 is assigned.

Calculation of the sector centres is carried out in a similar manner to that in section 8.4. However, the positions for each segment from simulation data were analysed to find the centre of each sector rather than the centre of the segment. This was done by splitting the segment up into thirds and finding the centre of that third for each radial and azimuthal sector. An example of this can be seen in Figure 8.9.

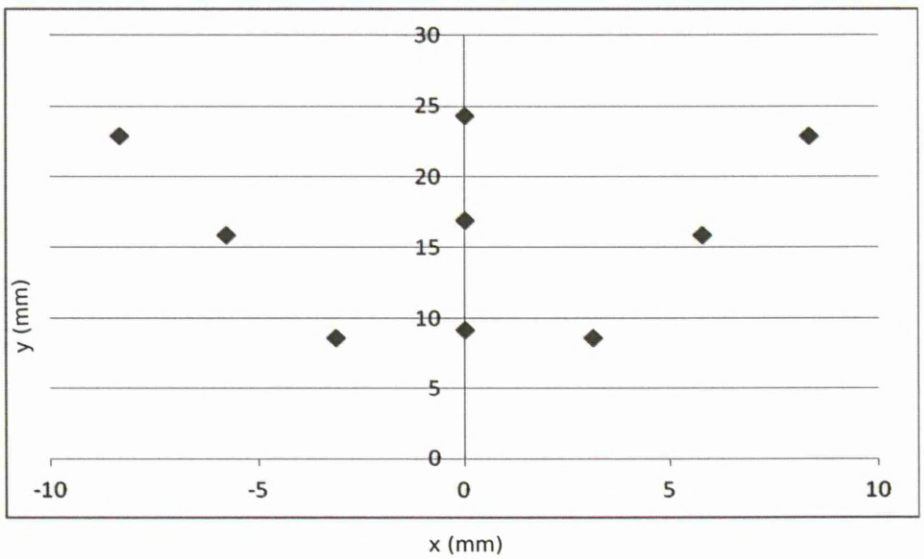

Figure 8.9: A plot to display sector centres.

These sector centre positions were assigned with the sector number from the map shown in Figure 8.8, enabling this to be compared with the experimental interaction position number set by the radial and azimuthal gates. Both the experimental data and position data were read into the MATLAB programming environment. A code was constructed to assign a sector centre position to the radial and azimuthal gate number and write these position and energy assignments to file.

The data set with the sector centre positions and energy deposited was read into the Compton image reconstruction code. The resulting image of two 1332 keV ^{60}Co sources can be seen in Figure 8.10.

The reconstructed image shown in Figure 8.10 has an offset of 300 mm. The two sources are able to be distinguished with the peaks seperated $\approx$ 60 mm. The x and y profile has been fitted using a Lorentzian peak fit and quadratic background fit utilising a least squares minimisation fit. There are two peaks seen in the x and y profiles, at 278 $\pm$ 1 mm and 365 $\pm$ 1 mm in the x profile and 267 $\pm$ 1 mm and 330 $\pm$ 1 mm in the y profile. The image FWHM values for these peaks are 70 $\pm$ 2 mm

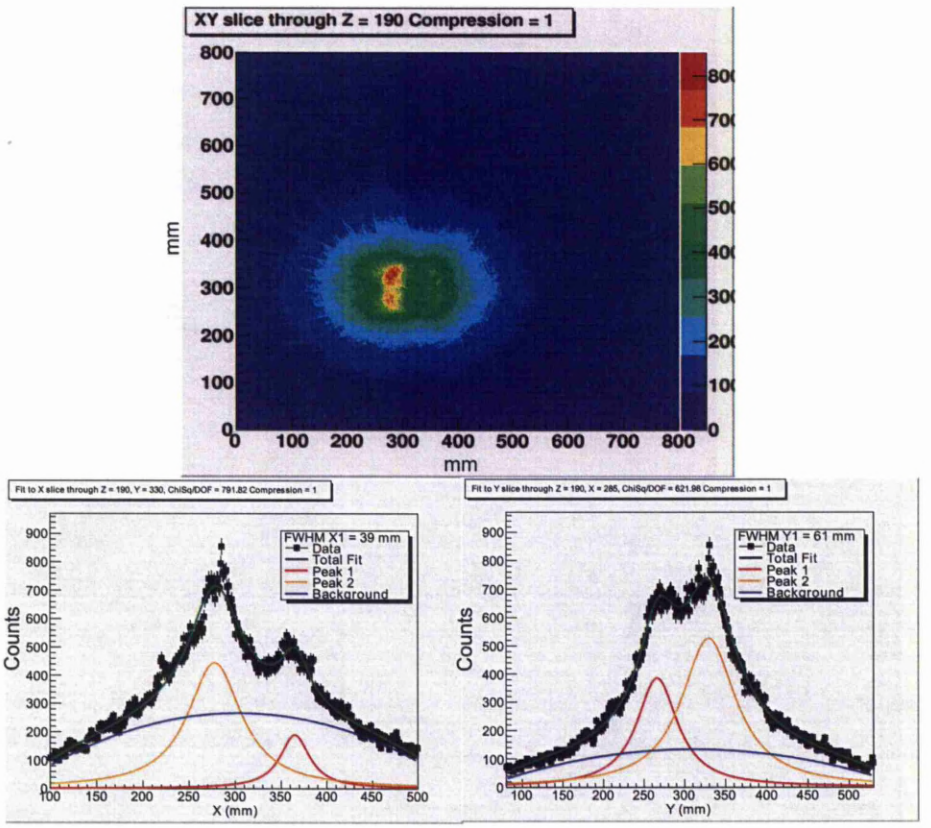

Figure 8.10: Image slice of two 1332keV ^{60}Co point sources located 100mm from the front face of the detector, utilising the segment centre as the position of interaction. The image FWHM values for these peaks are 70 ± 2 mm at 278 mm and 80 ± 2 mm at 365 mm in the x profile. In the y profile the image FWHM values for these peaks are 60 ± 2 mm at 267mm and 80 ± 2 mm at 330 mm.

at 278 mm and 80 ± 2 mm at 365 mm in the x profile. In the y profile the image FWHM values for these peaks are 60 ± 2 mm at 267mm and 80 ± 2 mm at 330 mm.

8.6 Effect of the weighting field on image reconstruction

The simulated weighting field of an AGATA prototype detector can be seen in Figure 8.11. This shows the complex electric field on the charge carrier trajectories and will have an effect on the Compton image reconstruction.

The electric field distributions can be considered as planar (zone 1), semi-planar (zone 2) and bulk (zone 3). The influence of these regions on the charge carrier trajectories are shown in Figure 8.11b, Figure 8.11c and Figure 8.11d respectively. The electron trajectory is shown by the red path, while that of the holes is shown in black. The planar region, directly beneath the central anode, can be considered as influencing the charge carrier trajectories as if it were the bulk region rotated by 90°. Thus the qualitative change in T90 as a function of interaction depth resembles that of the radial variation in the bulk region. The most difficult section of the volume to interpret is that of zone 2. The complex shape of the outer cathode causes large variations in the radius as a function of depth and azimuthal angle. The surface on which the hole trajectories terminate also varies with interaction position and there are regions of weak electric field in the corners of the detector. The combination of these effects give rise to a large change in pulse shape response as a function of interaction position.

8.6.1 Image reconstruction of ring 1 to 3

The reconstructed image used 8306 counts and is shown in Figure 8.13. The image has an offset of 300 mm and the two sources can be distinguished, seperated by $\approx$ 60 mm. However, these are skewed and there is also an area of intensity at approximately 360 mm in the x profile. There are two peaks seen in the x and y profiles, at 287 $\pm$ 1 mm and 362 $\pm$ 1 mm in the x profile and 271 $\pm$ 1 mm and 325 $\pm$ 1 mm in the y profile. The image FWHM values for these peaks are 44 $\pm$ 4 mm at 287 mm and 29 $\pm$ 5 mm at 362 mm in the x profile. In the y profile the image FWHM values for

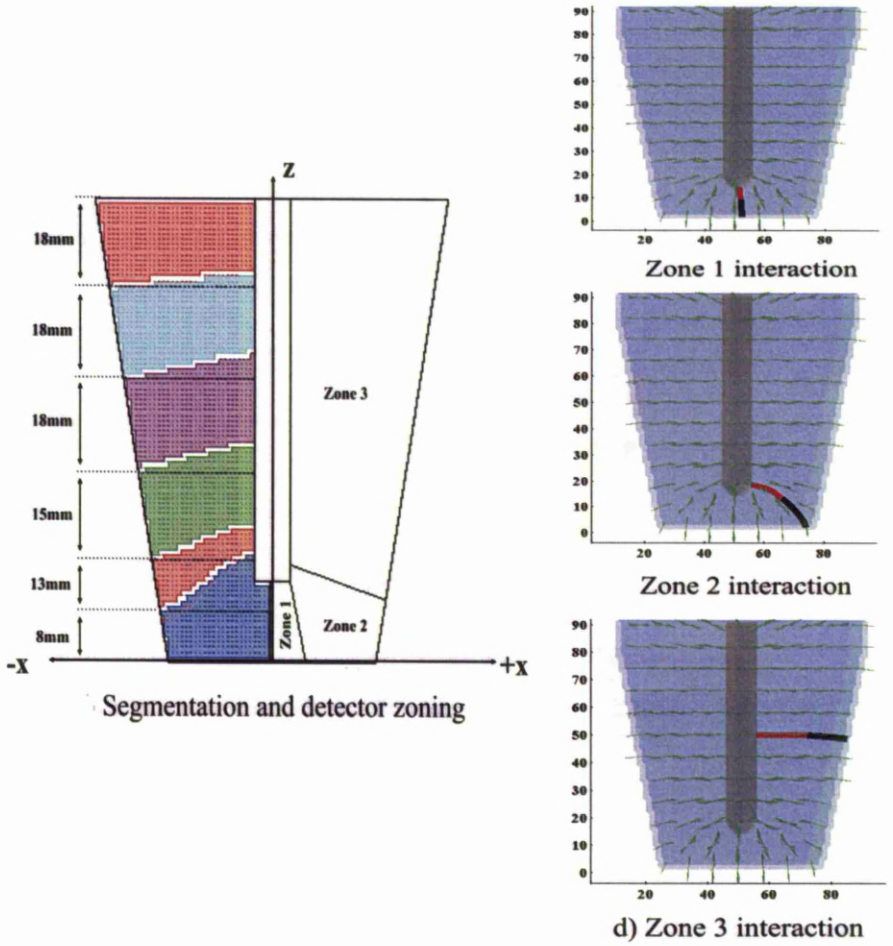

Figure 8.11: Simulated representation of the AGATA prototype detector geometry showing the effect of the complex electric field on the charge carrier trajectories.The crystal volume can be split into three distinct zones where the drift of the charge carriers is influenced by the planar, semi-planar and bulk electric field.

these peaks are 43 $\pm$ 4 mm at 271 mm and 45 $\pm$ 4 mm at 325 mm.

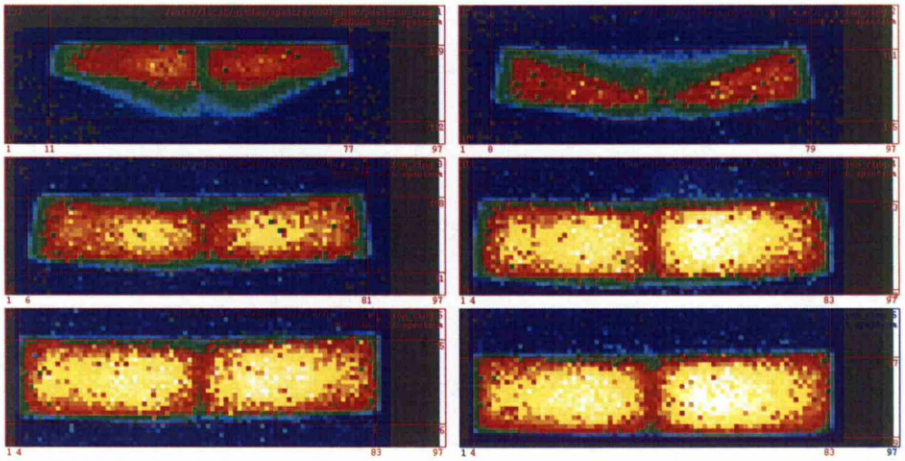

Figure 8.12: Experimental side scan data showing the weighting field within the AGATA C001 detector showing the effect of the complex electric field on the charge carrier trajectories.

8.6.2 Image reconstruction of ring 2 to 4

The reconstructed image uses 3480, Figure 8.14 has an offset of 300 mm, the two sources are able to be distinguished $\approx$ 60 mm peak to peak away from each other however it is difficult to see visually where the source is located. There are two peaks seen in the x and y profiles, at 291 $\pm$ 2.9 mm and 372 $\pm$ 2.2 mm in the x profile and 258 $\pm$ 9.4 mm and 350 $\pm$ 3.3 mm in the y profile. The image FWHM values for these peaks are 106 $\pm$ 32.9 mm at 291 mm and 35 $\pm$ 7.2 mm at 372 mm in the x profile. In the y profile the image FWHM values for these peaks are 295 $\pm$ 34.14 mm at 258 mm and 297 $\pm$ 16.06 mm at 350 mm. This fit is poor due to to the spread of the values.

8.6.3 Image reconstruction of ring 1 to 2

The reconstructed image uses 46060 counts, Figure 8.15 has an offset of 300 mm, the two sources are able to be distinguished $\approx$ 60 mm peak to peak away from each other but are however skewed.. There are two peaks seen in the x and y profiles, at 282 $\pm$

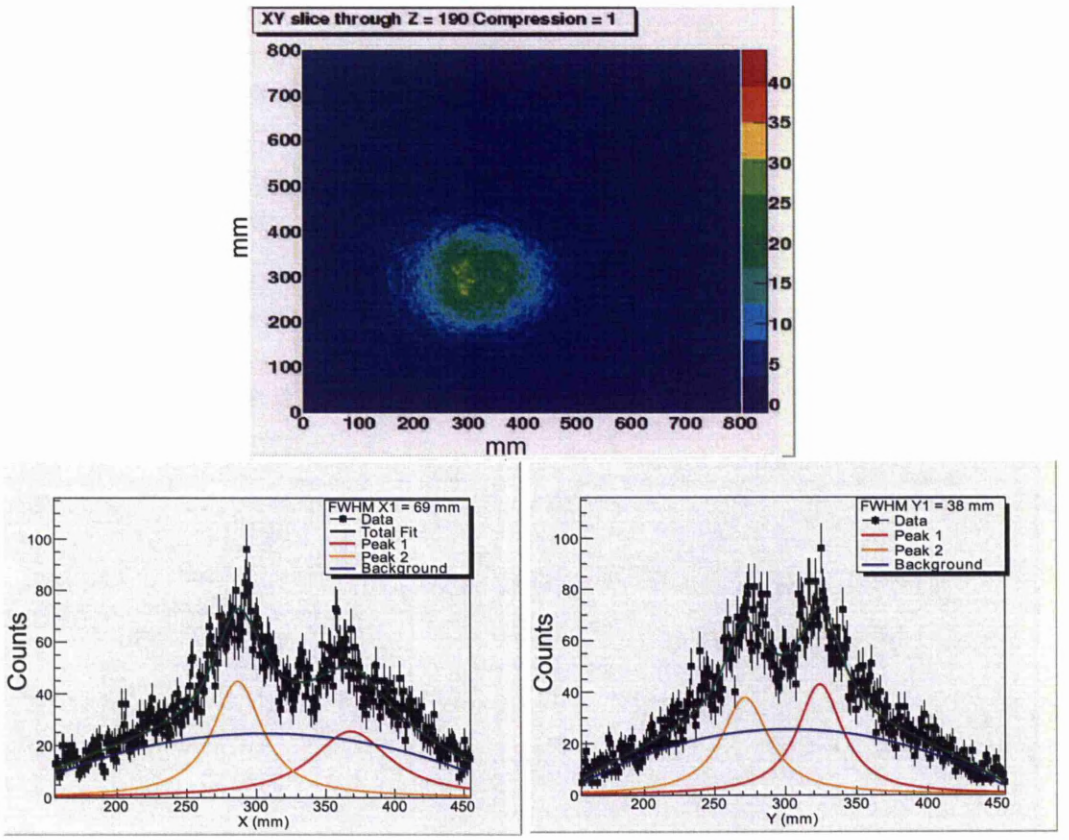

Figure 8.13: Image slice of two 1332keV ^{60}Co point sources located 100mm from the front face of the detector, with a Compton scatter from ring 1 to ring 3. The image FWHM values for these peaks are 44 ± 4 mm at 287 mm and 29 ± 5 mm at 362 mm in the x profile. In the y profile the image FWHM values for these peaks are 43 ± 4 mm at 271 mm and 45 ± 4 mm at 325 mm.

0.45 mm and 356 ± 0.9 mm in the x profile and 271 ± 0.4 mm and 329 ± 0.4 mm in the y profile. The image FWHM values for these peaks are 10 ± 1.4 mm at 282 mm and 30 ± 2.4 mm at 356 mm in the x profile. In the y profile the image FWHM values for these peaks are 26 ± 1.6 mm at 329mm and 27 ± 1.4 mm at 329 mm.

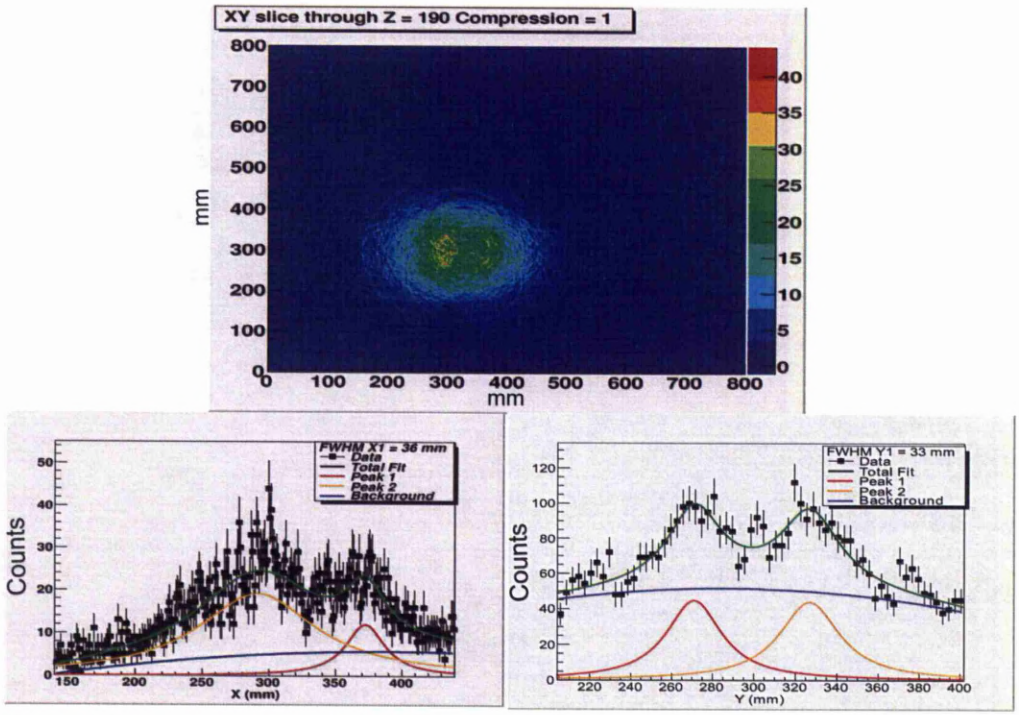

Figure 8.14: Image slice of two 1332keV ^{60}Co point sources located 100mm from the front face of the detector, with a Compton scatter from ring 2 to ring 4. The image FWHM values for these peaks are 106 ± 32.9 mm at 291 mm and 35 ± 7.2 mm at 372 mm in the x profile. In the y profile the image FWHM values for these peaks are 295 ± 34.14 mm at 258 mm and 297 ± 16.06 mm at 350 mm.

8.6.4 Image reconstruction of ring 2 to 3

The reconstructed image for rings 2 to 3 used 31205 counts and is shown in Figure 8.16. This image has an offset of 300 mm and the image shows that the two sources are not clearly distinguishable. There are two peaks seen in the x and y profiles, at 268 ± 1 mm and 363 ± 1 mm in the x profile and 269 ± 1 mm and 327 ± 2 mm in the y profile. The image FWHM values for these peaks are 51 ± 7 mm at 268 mm and 94 ± 7 mm at 363 mm in the x profile. In the y profile the image FWHM values

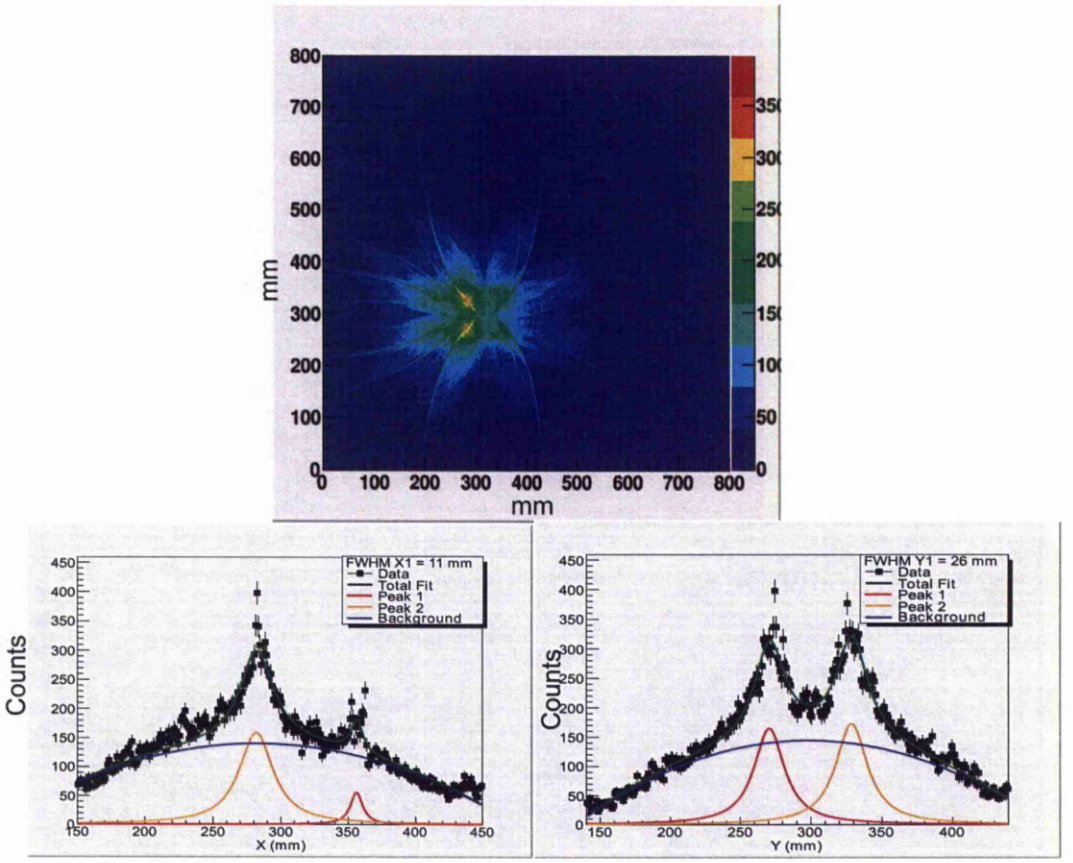

Figure 8.15: Image slice of two 1332keV ^{60}Co point sources located 100mm from the front face of the detector, with a Compton scatter from ring 1 to ring 2. The image FWHM values for these peaks are 10 ± 1.4 mm at 282 mm and 30 ± 2.4 mm at 356 mm in the x profile. In the y profile the image FWHM values for these peaks are 26 ± 1.6 mm at 329mm and 27 ± 1.4 mm at 329 mm.

for these peaks are 63 ± 5 mm at 269mm and 69 ± 6 mm at 327 mm.

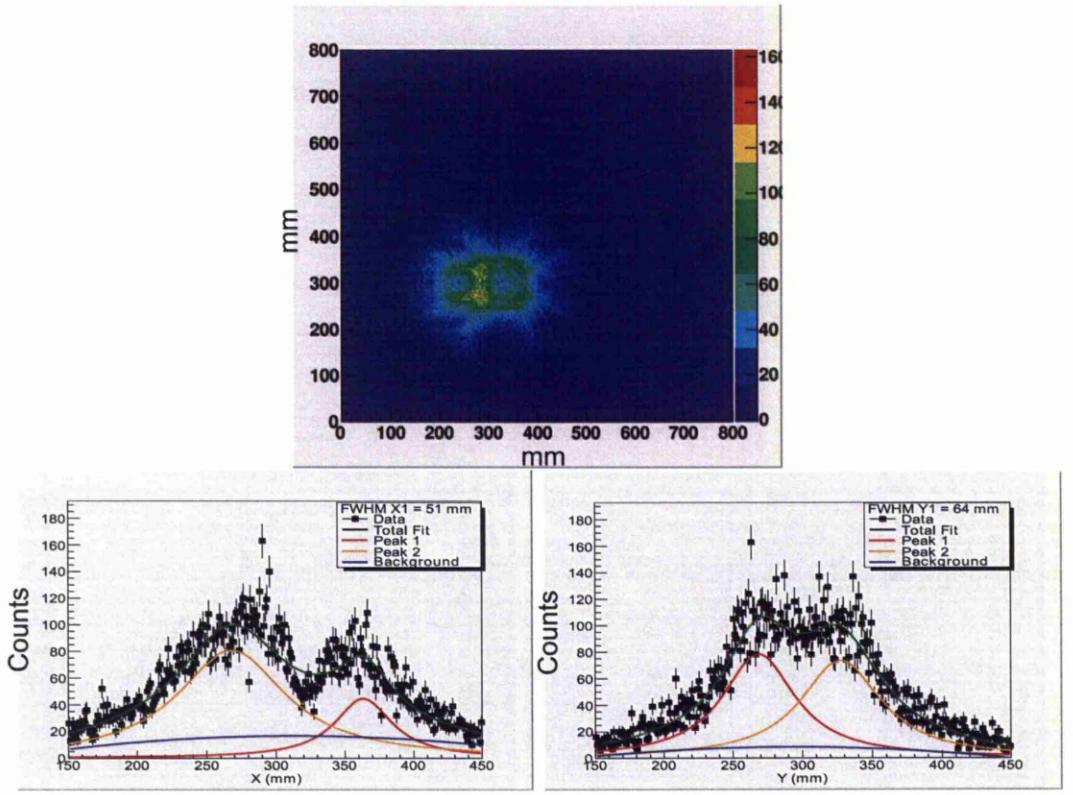

Figure 8.16: Image slice of two 1332keV ^{60}Co point sources located 100mm from the front face of the detector, with a Compton scatter from ring 2 to ring 3.The image FWHM values for these peaks are 51 ± 7 mm at 268 mm and 94 ± 7 mm at 363 mm in the x profile. In the y profile the image FWHM values for these peaks are 63 ± 5 mm at 269mm and 69 ± 6 mm at 327 mm.

8.7 Compton image reconstruction using 36 positions per segment for reconstruction

Pulse shape analysis splitting the azmuthal and radial positions into 6 to create 36 positions per segment has been performed.

The reconstructed image in Figure 8.17 uses 30254 counts. The image has an offset of 300 mm and there are two peaks seen in the x and y profiles. These are seen

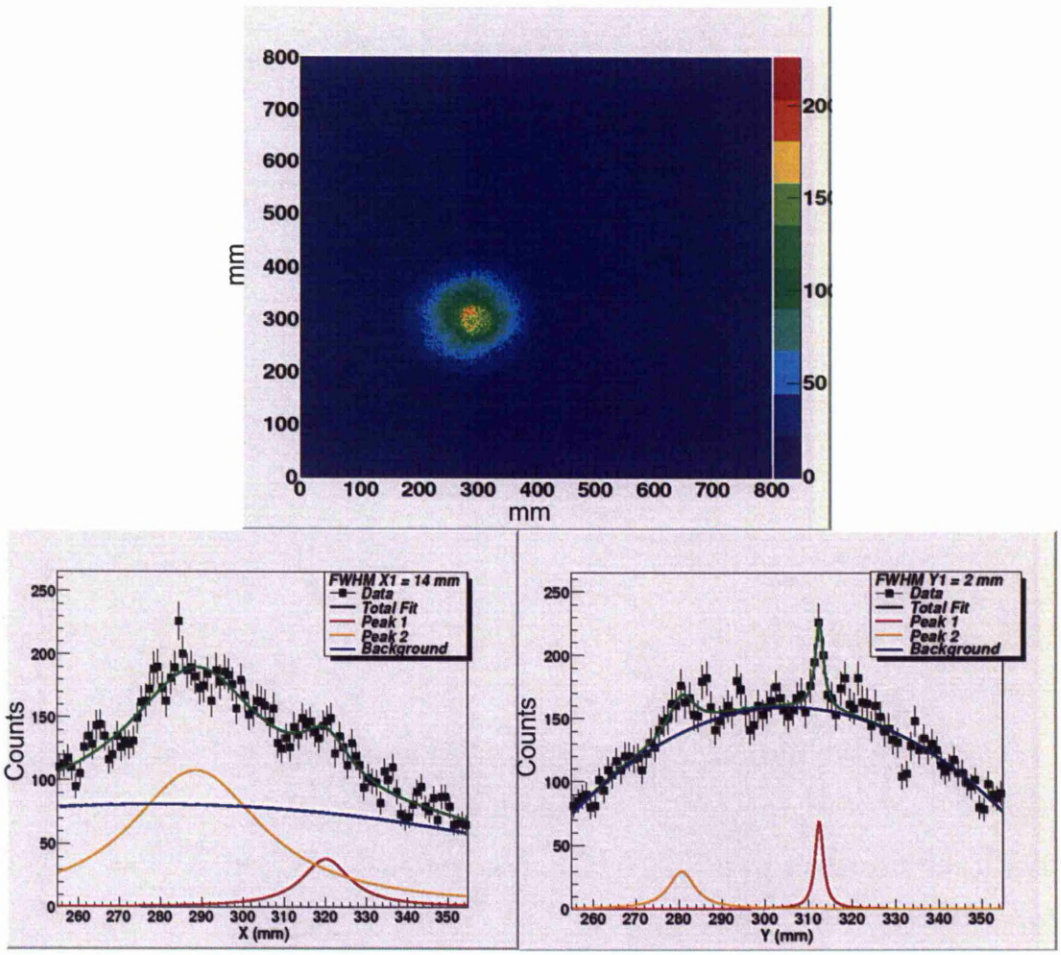

Figure 8.17: Image slice of two 1332keV ^{60}Co point sources located 100mm from the front face of the detector, with a Compton scatter from ring 1 to ring 3 using 36 points of interaction per segment. The image FWHM values for these peaks are 39 ± 6 mm at 288 mm and 14 ± 5 mm at 320 mm in the x profile. In the y profile the image FWHM values for these peaks are 7 ± 3 mm at 280mm and 2 ± 1 mm at 312 mm.

at 288 ± 1 mm and 320 ± 1 mm in the x profile and 280 ± 1 mm and 312 ± 1 mm in the y profile. The image FWHM values for these peaks are 39 ± 6 mm at 288 mm and 14 ± 5 mm at 320 mm in the x profile. In the y profile the image FWHM values for these peaks are 7 ± 3 mm at 280mm and 2 ± 1 mm at 312 mm. The two sources

cannot be clearly observed in the reconstructed image. With the segment split in a greater number of sectors there are a greater number of reconstructed cones, this leads to lower statistics for each reconstructed cone position. Therefore if a detector segment is to be split into more sectors then the statistics must be increased.

8.7.1 Compton image reconstruction using 3 positions through depth per segment

Figure 8.18 shows that increasing the number of interaction positions through depth in the segment improves the image however does not remove the ring effect. However, interactions that scatter directly behind when removed to account the for the ring effect results in a poor image with poor statistics. The reconstructed image uses 30254 counts. The image has an offset of 300 mm and there are two peaks seen in the x and y profiles. These are seen at 276 $\pm$ 1 mm and 397 $\pm$ 1 mm in the x profile and 272 $\pm$ 1 mm and 342 $\pm$ 1 mm in the y profile. The image FWHM values for these peaks are 71 $\pm$ 3 mm at 276 mm and 68 $\pm$ 5 mm at 397 mm in the x profile. In the y profile the image FWHM values for these peaks are 46 $\pm$ 2 mm at 272 mm and 44 $\pm$ 1 mm at 342 mm.

8.8 Conclusion

In conclusion, analysis of the Compton image reconstruction of the experimental data show that using more precise methods of locating the position of interaction increases the image resolution of the Compton image reconstruction of point sources. By increasing the number of cone axis variations it can be seen that the image resolution improves. This is due to a greater variety of reconstructed cones enabling the position of the projected source to become more accurate. However, increasing the number of cones decreases the statistics per reconstructed cone position. The position of the source is more accurately located but the lack of statistics means that the position of the source is not clear. The results also show that imaging with a gamma-ray energy

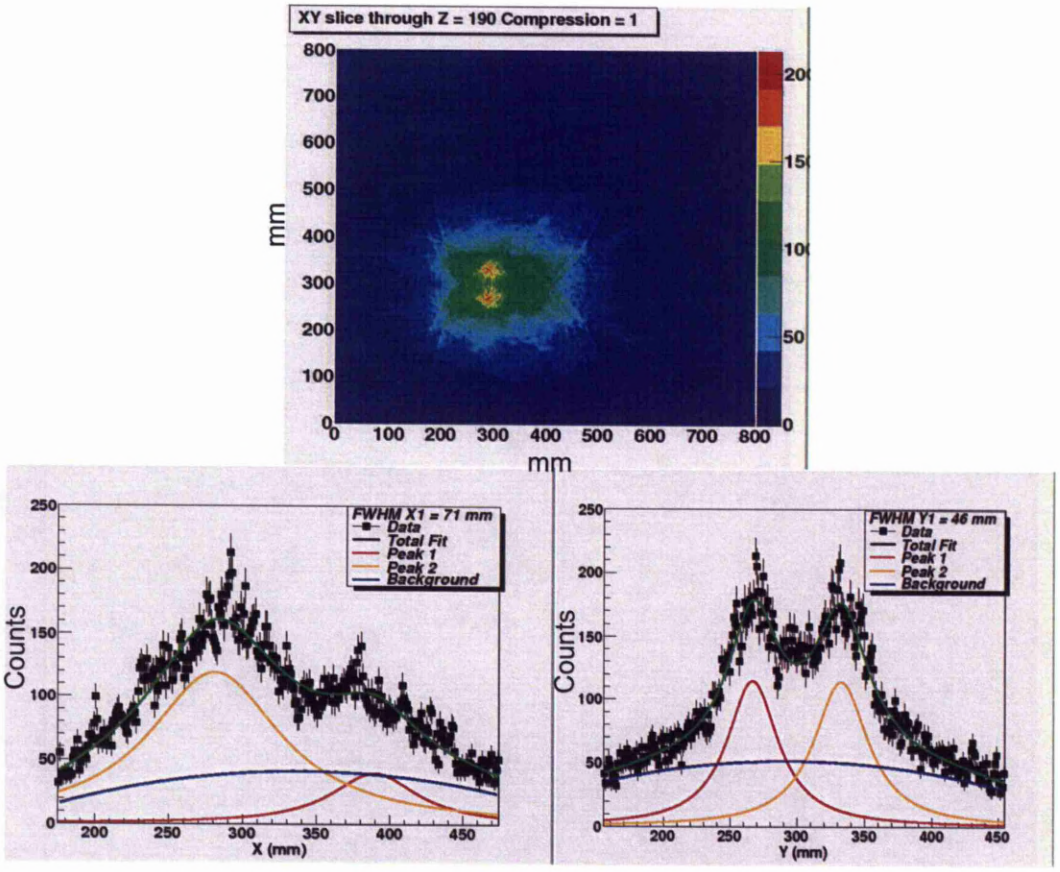

Figure 8.18: Image slice of two 1332keV ^{60}Co point sources located 100mm from the front face of the detector, with a Compton scatter from ring 1 to ring 3 using 3 positions of interaction through depth per segment. The image FWHM values for these peaks are 71 ± 3 mm at 276 mm and 68 ± 5 mm at 397 mm in the x profile. In the y profile the image FWHM values for these peaks are 46 ± 2 mm at 272 mm and 44 ± 1 mm at 342 mm.

source of 1332 keV results in a ring effect in a highly segmented coaxial detector but can be corrected by removing events that scatter into segments behind. This has been explained through comparision of the hit matrix and the Klien-Nishina distribution to the reconstructed image. It has been seen that 1332keV gamma ray is most likely to scatter forwards. This results in a large number of cones overlapping

in six reconstructed positions, creating a visible ring effect. The weighting field, a method of solving the instantaneous electric field can be used to explain the poor quality of some of the images seen especially in ring 2. Figure 2.6 shows the effect of the weighting field on a planar detector. However, the detector geometry in the front two rings of the detector is different to the rings further back, as explained in 8.11. This results in a more complex weighting field in rings 1 and 2 compared to rings further back. This will have a effect on the response of the pulse shape making it more difficult to interpret using parametric PSA methods, resulting in a greater uncertainty in the position of interaction.

Chapter 9

GEANT4 simulation

9.1 Introduction

The GEANT4 simulation package enables the simulation of the passage of particles through matter.[50] The ability to reproduce radiation interactions within matter using Monte Carlo simulation is an invaluable tool to produce realistic simulated data. Simulated data are essential in the design and optimisation of novel and existing systems to understand their potential and constraints. This chapter will focus on the potential of simulating the AGATA A006 detector. The AGATA Geant4 simulation package has been developed at the Istituto Nazionale di Fisica Nucleare (INFN). The code is well maintained and is in widespread use. It is C++ based and leaves the user with flexibility on the geometry definition, detector response and read out and event generation.

The AGATA implementation in the Geant4 simulation package is a command-line user interface. There are built-in commands to change simulation parameters without recompiling. Macro files can be used to automate command sequences and also graphics can be enabled when needed, which enables the running of the simulation to be sped up.

The AGATA GEANT4 simulation package contains mandatory user-defined classes such as the DetectorConstruction and PrimaryGeneratorAction classes and pointers

to standard user-defined classes.

The AgataDetector Construction class is used to define the material definition, the experimental hall and there are changeable scenarios to be selected at the start of the main program, from a single germanium detector through to a whole array.

The AGATA GEANT4 files have been adapted to replicate the experimental setup as shown in Figure 9.1.

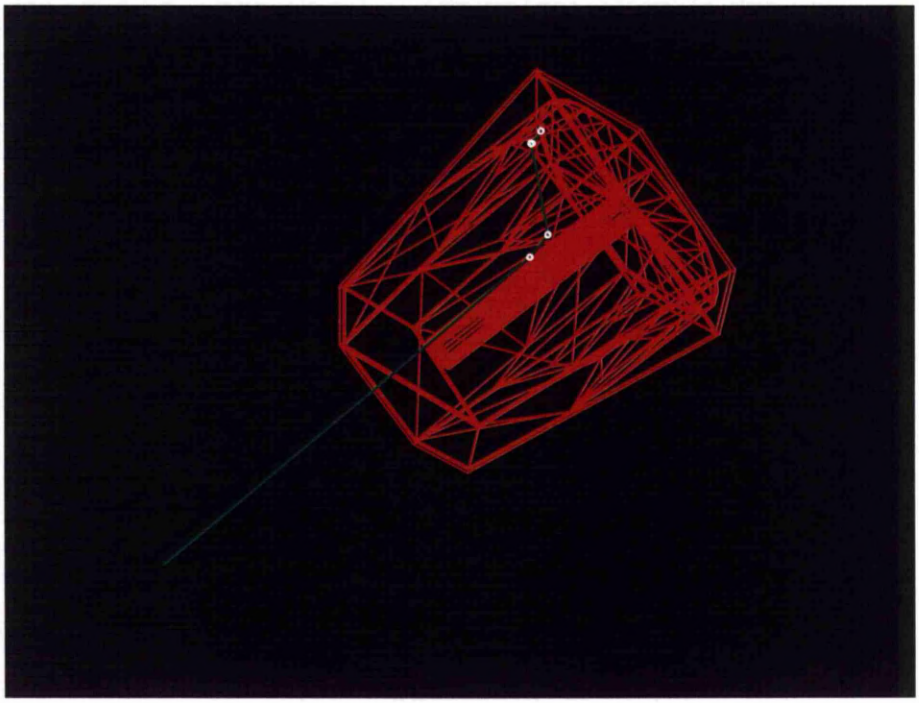

Figure 9.1: Model of the A006 AGATA detector utilising the HepRApp visualisation package

9.2 Model of the detector

A simulation of the detector was created using the simulation package GEANT4. GEANT4 is a Monte Carlo method, simulating physical and mathematical systems developed in the CERN community. The GEANT4 simulation package enable the

design and response of a detector to be understood. The package implements the following components into the simulation:

- the geometry of the system
- the materials involved
- the particles of interest
- the generation of primary particles of events
- the tracking of particles through materials and external electromagnetic fields
- the physics processes involved in particle interactions
- the response of the sensitive detector components

The code has been produced for configurations of the AGATA and GRETA arrays, namely arrangements of clusters of encapsulated coaxial detectors with irregular shapes, grouped into the same cryostat.

Five files are required to build the full geometry; the default names are the following:

1. asolid: description of the detectors
2. aclust: description of the clusters
3. awalls: description of the cryostat walls
4. aeuler: transformations needed to place the clusters
5. aslice: description of the segmentation

9.3 Data output

The information on the fired particle and its interactions with the active elements were listed in the following format:

- ndet, the detector number in which the interaction occurred
- edep (keV), energy released in the interaction
- Px Py Pz, the absolute position (laboratory reference frame, in terms of the unit of length) in which the interaction occurred
- nseg, segment of interaction encoded as 10*slice number + sector number
- nInt, The type of interaction

An example of the outputted data can be seen in table 9.1

Table 9.1: Example of outputted data from the AGATA GEANT4 simulation

ndet	edep	Px	Py	Pz	nseg)
0	681.72	-23.975	-18.34	135.829	24
0	179.18	-14.514	-21.305	145.353	34
0	113.489	-13.899	-24.021	146.912	34
0	125.382	-9.474	-25.931	158.632	44
0	230.074	-5.506	-29.184	159.611	44
0	1.255	-9.471	-25.935	158.622	44

The outputted data could then be analysed, the data needs to be sorted to output fold 2 events within the detector.

9.3.1 Data processing

Each gamma ray was assigned a unique event ID number this corresponds to n^{th} gamma ray generated, enabling each individual event to be tracked. If the gamma

ray underwent an interaction within the detector volume an interaction number i was assigned to it, that corresponded to the i^{th} interaction of that event, along with the segment number. A C++ program was developed to analyse the output of the GEANT4 program, to process the data for imaging:

- using the ndet value, if this value represents a value within the detector, then this event was further analysed.
- a calculation was carried out to calculate the fold of the event.
- if the event was a fold 2 event, i.e. in this case represented an interaction in two separate segments, the sum of energies for the segments was calculated.
- if there was more than two interactions per segment, the position at which the most energy was deposited was assumed to be the point of interaction.
- the energies and positions for the fold 2 events were then written out.

A C++ code was utilised to sort the outputted GEANT4 data, if an interaction was detected within the detector. Table 9.1 shows that there can be several interactions within one segment. The interactions in the first hit segment for an event were all added together and the second hit segment was written out along with the total of the remaining energies. An example of this can be seen in table 9.2.

Table 9.2: Example of the sorted simulated data read into the Compton Image Reconstruction code

Segment 1	Energy(keV)	Segment 2	Energy (keV)
21	175	27	1157.1
12	395.93	24	932.927
19	242.552	24	1070.43

9.4 Experimental setup geometry

The experimental setup was replicated utilising an adapted AGATA GEANT4 simulation code. A single A-type crystal was defined with two gamma-ray sources, with energy 1173 keV and 1332 keV, positioned 100 mm from the front face of the crystal, 60 mm apart.

The detector geometry was evaluated by running 5 million events, with the simulation model of the detector replicating the experimental setup, using the AGATA GEANT4 simulation code. The MATLAB programming environment was used to plot and evaluate the geometry of the detector and is discussed in 8.4.

9.5 GEANT validation

The AGATA GEANT4 simulation code was pre-validated during the development of the simulation code [51]. A validation between the simulation and experimental results is required to see if the two are comparable. This was carried out by comparing the peak to total value and the response compared to the experimental data. These two values are measurements that are commonly carried out to analyse the performance of radiation detectors.

9.5.1 GEANT4 energy spectrum

Figure 9.2 shows the total of all the segments added together for the GEANT4 simulation. The Figure shows a single photopeak, as explained in section 9.2. This photopeak is the 1332 keV ^{60}Co peak from a source located 250 mm away from the front face of the detector. In total there are $\sim$ 49567 events used to create this spectrum.

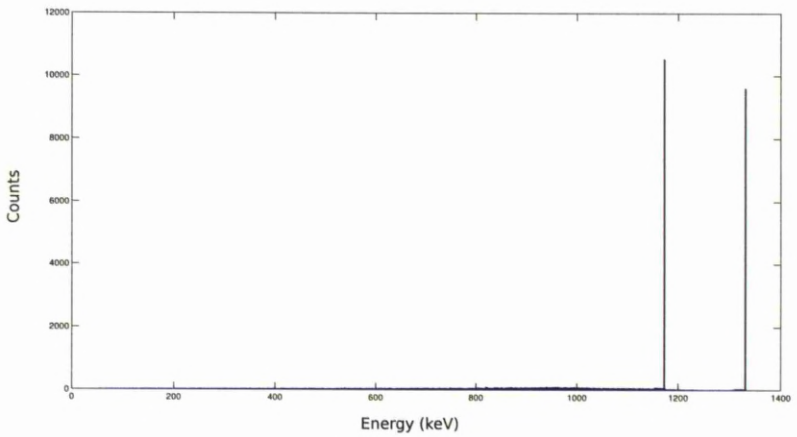

Figure 9.2: Spectrum to show the sum energy of a ^{60}Co source of all the segments from GEANT4 simulation of the detector.

9.5.2 Peak to Total

The peak to total calculation has been carried out using a ^{60}Co source placed at 100mm from the front face of the AGATA detector. The value has been calculated from the total spectrum in Figure 9.2 using equation 9.1

$$P : T = \frac{100 * N_p}{N_T} \tag{9.1}$$

The number of counts in the photopeak is defined as N_p and the total number of counts is defined as N_T. The peak to total value is measured to be 11.5±0.05%.

9.5.3 GEANT4 hit matrix

Figure9.3 shows the most likely scatter pattern of an incident gamma ray. The linear attenuation coefficient of a ^{60}Co gamma ray in Germanium is a 4 mm^{-}1. It is clear from the 2-D plots that the energy will be totally absorbed in the first interaction or will scatter and be absorbed within the nearest neighbour. The 2-D matrices are gated on fold two events only. The first hit, scatter segment, is the x-axis. With the

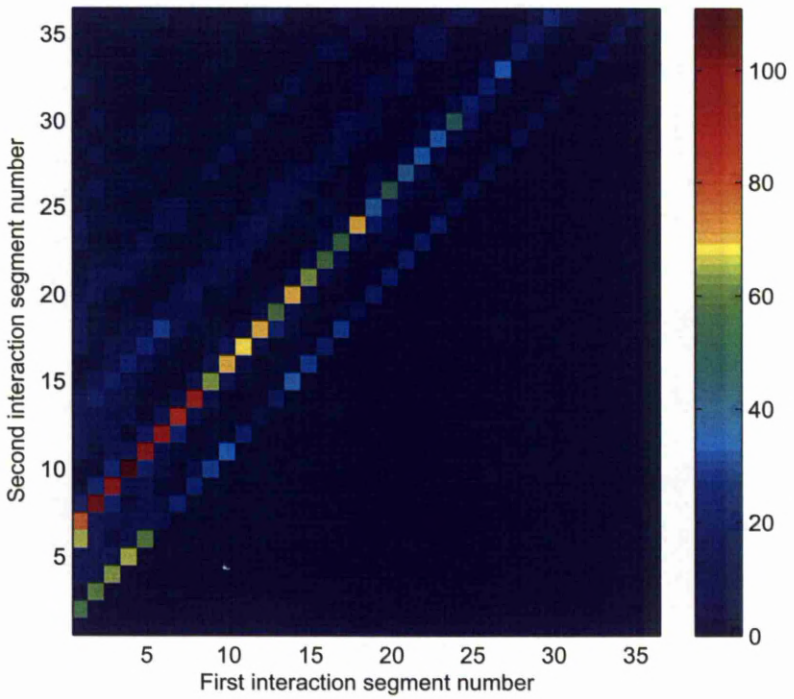

Figure 9.3: Figure to show hit matrix from the simulated data.

second hit, absorber segment being on the y-axis.

9.6 Compton imaging utilising the simulated data

Simulated data, unlike experimental data, do not have a finite energy and position resolution and will create a perfect environment. By using this perfect environment it is possible to assess the effects of position and energy resolution on the Compton image reconstruction. This section will discuss the effect of energy resolution on the resolution of Compton reconstructed images and the effect position resolution has on the Compton reconstructed image.

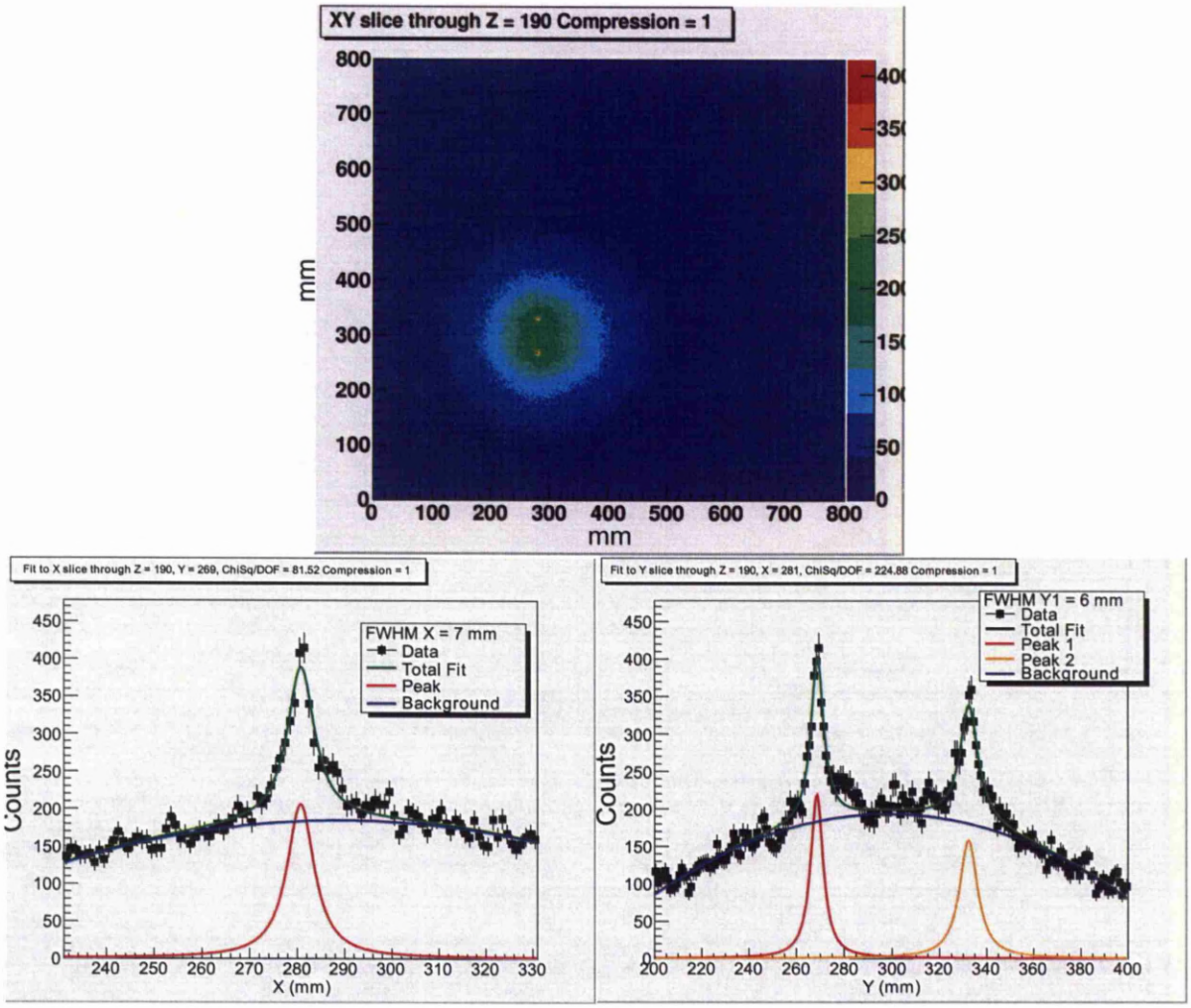

Figure 9.4: Image slice of two 1332keV ^{60}Co point source located 100mm from the front face of the detector, utilising an energy and position spread to compare with experimental PSA results

An image with precise energy and position resolution in a replicated experimental setup produces a reconstructed image for two ^{60}Co sources located 100 mm away from the front face of the detector, placed 60 mm apart.

The reconstructed image shown in Figure 9.5 has an offset of 300 mm and shows that the two sources are able to be distinguished. These can be seen to be $\approx$ 60

mm peak to peak away from each other. The x and y profile has been fitted using a Lorentzian peak fit and quadratic background fit utilising a least squares minimisation fit. There are is one major peak in the x profile, at 280 mm, with two major peaks in the y - profile. These correspond to point sources located at 268 mm and 332 mm. The image FWHM values for these peaks are 7 mm at 280 mm in the x profile. In the y profile the image FWHM values for these peaks are 6 mm at 268 mm and 9 mm at 332 mm.

9.6.1 Image reconstruction utilising segment centres

The ring effect seen in the previous chapter has been investigated using the GEANT4 simulation, the reconstructed Compton image utilising the segment centres as the position of interaction also results in this ring effect. This therefore shows that the reason for this ring is the scattering from the scatter segment into the segments behind dominating the reconstruction cones.

9.7 Image reconstruction utilising energy and position spread to calculate position resolution of the experimental data

9.7.1 Effect of Energy Resolution on the Image Quality

The effect of the energy resolution on the reconstructed image will be discussed in this section. As mentioned earlier the simulated data do not have the finite energy resolution that is seen in an experimental dataset.

Using simulated data therefore will enable an understanding of the effect the energy resolution has on the reconstructed Compton image to account for the finite energy resolution of a real experimental setup.

To evaluate this the simulated energy data was smeared using a Gaussian function

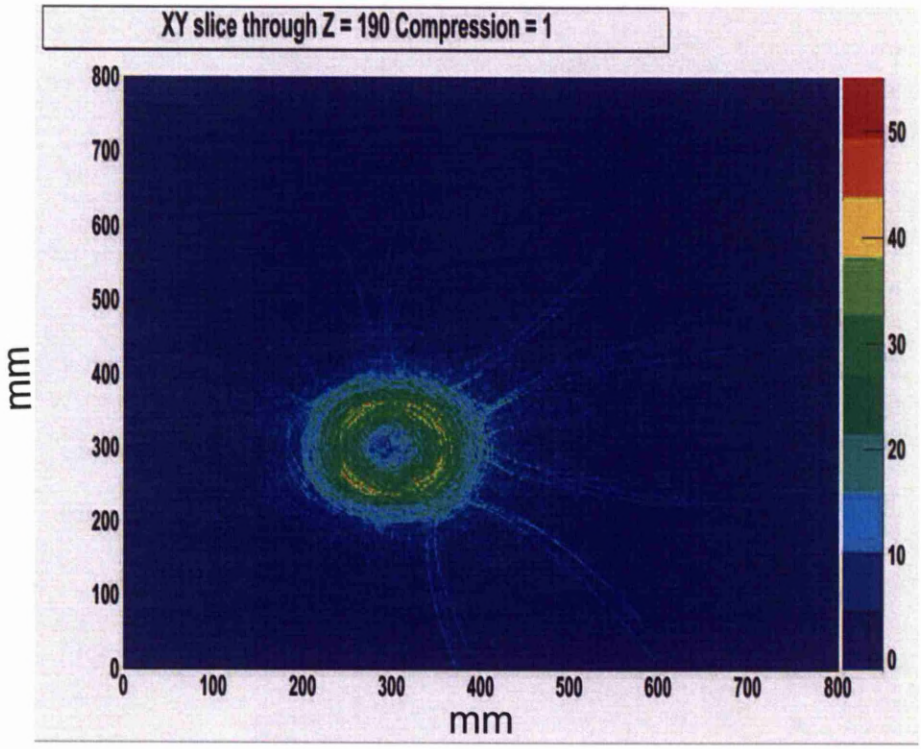

Figure 9.5: Image slice of two simulated 1332keV ^{60}Co point sources located 100mm from the front face of the detector, utilising the segment centre as the position of interaction

and the position information is left unchanged.

The energy was smeared using the ROOT tool kit [52], using the standard random number generator, *grandom*, using the following function:

$$E_{smeared} = gRandom \rightarrow Gaus(E, \sigma) \tag{9.2}$$

where $\sigma = \frac{FWHM_E}{2\sqrt{2ln2}}$

This energy smear was applied to the energy deposited in the scatter and absorber segments. This generated an array of random numbers following a Gaussian distribution with a mean that was equal to the deposited energy. The results of the energy smearing utilising an energy smear of 0 to 5 keV on the simulated data can be seen

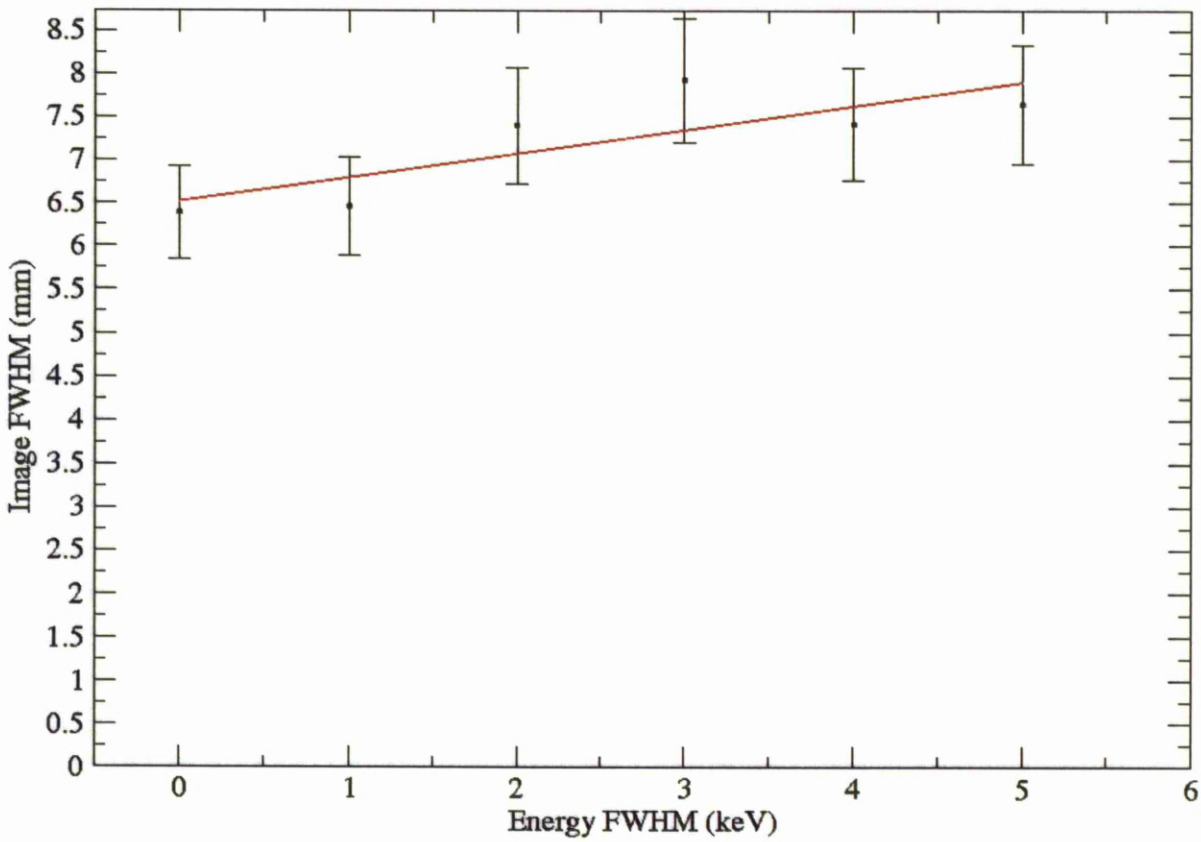

Figure 9.6: The simulated energy resolution vs. image resolution. With no energy smearing the reconstructed Compton image resolution in the x plane is 6.2 mm, increasing to 7.5 mm at 5 keV.

in Figure 9.6. With no energy smearing the reconstructed Compton image resolution in the x plane is 6.2 mm, increasing to 7.5 mm at 5 keV.

9.7.2 Effect of position resolution on the image quality

The experimental reconstructed Compton images gave information on the image resolution. A way to calculate the position resolution of the experimental Compton reconstructed images is to compare this known position smeared simulated values. To do this the simulated energy was smeared to a value that of the average experimen-

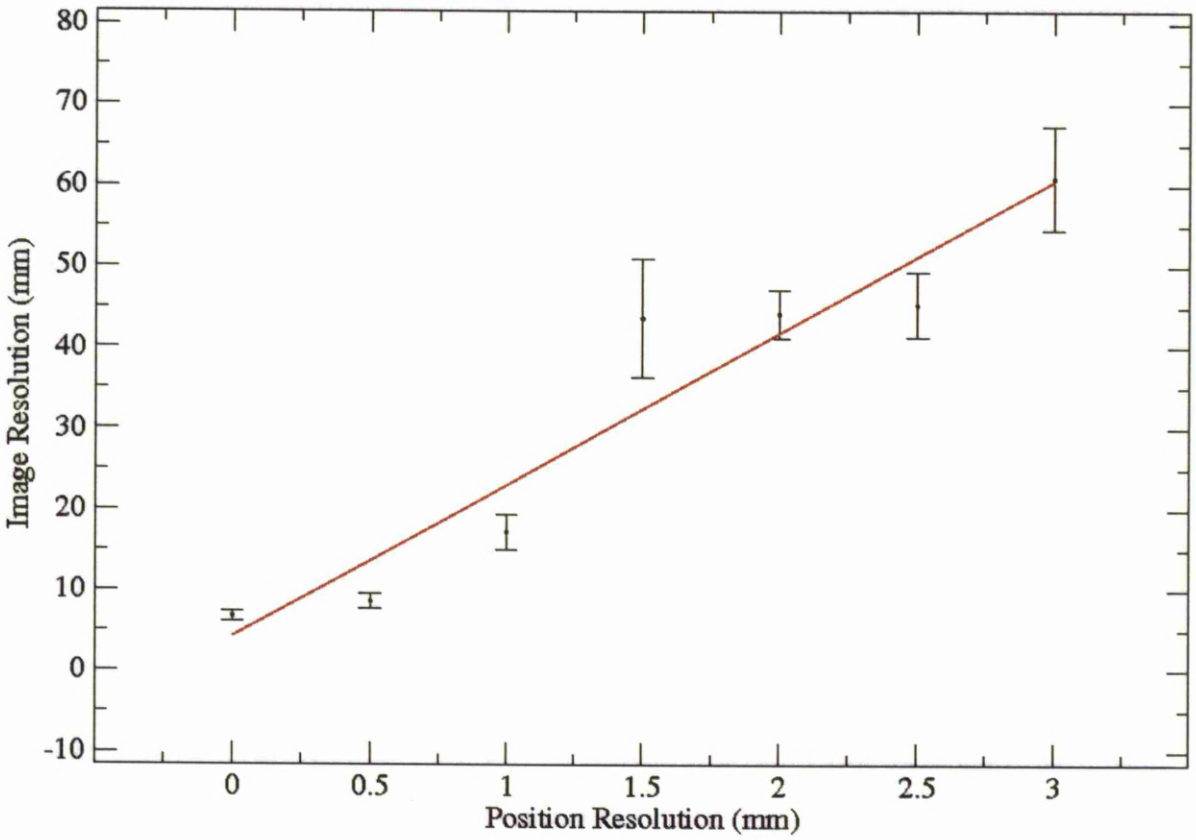

Figure 9.7: The simulated smeared position resolution plotted against the image resolution.With precise position resolution utilising an energy smear the image FWHM in the x profile is 7 mm. However as the position resolution increases to 3 mm the image resolution increases to 60 mm.

tal energy resolution, which was calculated to be 2.788 keV. The simulated position data were smeared using the method used in subsection 9.7.1. The position resolution plotted against the image resolution can be seen in Figure 9.7

The position resolution of the detector has a greater effect on the reconstructed image quality than the energy resolution. With precise position resolution utilising an energy smear the image FWHM in the x profile is 7 mm. However, as the position resolution increases to 3 mm the image resolution increases to 60 mm.

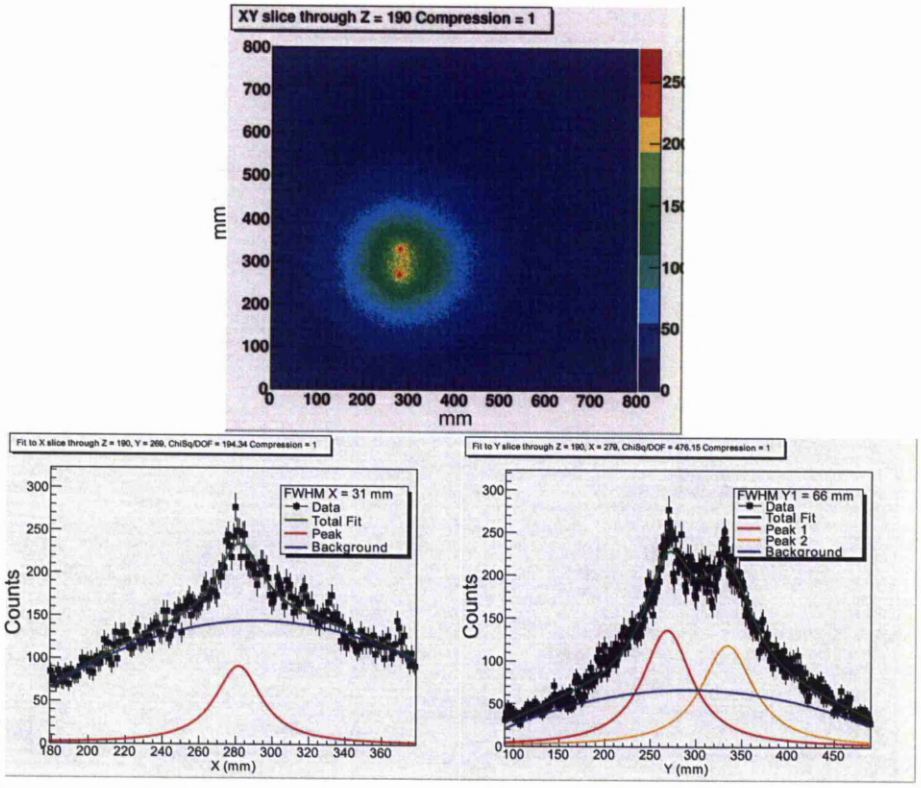

Figure 9.8: Image slice of two simulated 1332keV ^{60}Co point sources located 100mm from the front face of the detector, utilising an energy and position spread to compare with experimental PSA results. The image FWHM values for these peaks are 30 mm at 280 mm in the x profile. In the y profile the image FWHM values for these peaks are 65 mm at 268 mm and 69 mm at 335 mm.

Figure 9.8 is a reconstructed image of the experimental setup with a an energy spread of 2.7 keV and position resolution of 3mm. It has an offset of 300 mm, the two sources are able to be distinguished $\approx$ 60 mm peak to peak away from each other. The x and y profile has been fitted using a Lorentzian peak fit and quadratic background fit utilising a least squares minimisation. There are is one major peak in the x profile, at 280 mm, there are two major peaks in the y - profile these correspond to point sources located at 268 mm and 335 mm. The image FWHM values for these peaks

are 30 mm at 280 mm in the x profile. In the y profile the image FWHM values for these peaks are 65 mm at 268 mm and 69 mm at 335 mm.

9.8 Conclusion

The GEANT4 simulation has been utilised as a tool to assess the effect of energy and position resolution on the image resolution Compton reconstructed images. It has been shown that the effect of the energy resolution on the image resolutions causes an increase of $\approx$ 1 mm image resolution from 0 keV energy resolution to 5 keV energy resolution.

This can be compared to the effect of the position resolution on the image resolution wher the image resolution increases by $\approx$ 54 mm going from infinite position resolution to a position resolution of 3 mm. The energy resolution affects the opening angle of the reconstructed cone. It has been shown that for high gamma-ray energies the effect on the uncertainty on the scatter angle is minimal. However, for lower energies this would have a greater effect on the image resolution. The interaction position of a gamma ray depends on the ability of the detector to discriminate the position of interaction. It has been shown that the discrimination of interaction position can be improved by utilising this method of parametric PSA to 3.0 $\pm$ 0.5 mm, through the comparison of experimental data to simulated data.

Chapter 10

Summary and Further Work

This work has assessed the improvement that different position analysis techniques provided for Compton image reconstruction using a highly segmented large volume detector. The use of such a highly segmented large volume detector has enabled the effect of the determination of position to be investigated and the effect on the image quality of a reconstructed Compton image.

Two ^{60}Co point sources have been imaged simultaneously experimentally and through a GEANT4 simulation utilising different position analysis techniques. Both of these data sets have been analysed, sorted and reconstructed utilising a Compton image code developed by Judson.

The advantage of this reconstruction code is that it is quicker than existing Compton image reconstruction codes available for this investigation. It also incorporates a new fitting routine for a Lorentzian peak fit with a quadratic background fit utilising a least squares minimisation fit to give a total peak fit.

The simulated energy and position has been smeared using a C++ code. This data has been reconstructed and the image resolution has been compared with that of the experimentally reconstructed data. It has been found that the parametric PSA method developed in this thesis, will give a position resolution of 3.0 $\pm$ 0.5 mm within the segments of the crystal when compared to a 15.0 $\pm$ 0.5 mm position resolution for data reconstructed without utilising parametric PSA. The reconstructed images

show an improved image quality as the ability to locate the position of interaction increases. This has been investigated using a simulated model to assess the contributions of energy resolution and position resolution to the experimental Compton reconstructed images.

The GEANT4 simulation has been utilised as a tool to assess the effect of energy and position resolution on the image resolution. It has been shown that the effect of the energy resolution on the image resolution causes an increase of $\approx$ 1 mm on the image resolution from perfect energy resolution to 5 keV energy resolution.

This can be compared with the effect of the position resolution on the image resolution, which results in an increase of $\approx$ 54 mm, going from infinite position resolution to a position resolution of 3 mm.

The energy resolution affects the opening angle of the reconstructed cone. It has been shown that for gamma-rays with high energies the effect on the uncertainty on the scatter angle is minimal. However, for lower energies this would have a greater effect on the image resolution.

The deduced interaction position of a gamma ray depends on the ability of the detector to discriminate the position of interaction. It has been shown that the discrimination of the interaction position can be improved by utilising parametric PSA to 3.0 $\pm$ 0.5 mm at 100 mm, through the comparison of experimental data with simulated data.

At 1332 keV the results could be compared with simulated results, as the gamma rays were able to penetrate a greater distance within the detector. This overcomes the uncertainty in the position of interaction in the first two rings due to the different response of the electron and hole collection in these rings. This is in turn due to the more complex geometry, compared with the rings near the back of the detector that are more coaxial.

An ideal detector to use in the context of the GammaKEV project would be a coaxial shape without any tapering at the front. The tapering in the AGATA detectors introduces an electric field that is complex.

The use of CZT utilising an ASIC has been investigated for compton imaging, it has been found that at higher energies there is a greater charge sharing within neighbouring pixels. These cannot be recovered using the NUCAM II ASIC but the PorGamRays ASIC will allow for this. Compton image reconstruction has been carried out using a $^{1}33$Ba source with an energy of 80 keV 35 mm away from the front face of the detector. An image resolution of 20 mm was measured in both the x and y plane. The methods developed in this work can be used to improve Compton image reconstruction, through increased position discrimination for the GammaKEV project. This enables larger segmented materials to be considered, as this work has shown that parametric PSA has drastically improved the position resolution in large segments.

10.1 Future Work

The parametric PSA should be further be developed for this project and could be carried out through collecting scans across the front face and side of the detector, to enable the rise time reponse and image charge response to be understood as a function of position. This would enable more accurate conditions on the rise time pulse and image charge asymmetry to be applied.

It has been shown that the ability to locate the position of interaction is important for precise Compton image reconstruction. The work carried out in this thesis could be developed through the use of library PSA (BASIS). This requires a database of pulse shapes per position across the detector to be generated through a full electric field simulation of the detector. These algorithms provide a spatial resolution of $\approx$ 1mm from multiple hit events with the ability to distinguish multiple interactions occurring within a single pixel [18]. Whether improvements in performance resulting from the use of advanced PSA techniques translate to improvements in image quality is yet to be seen, as is whether or not the increased CPU requirements of database matching approaches are justified by improved imaging performance, especially for a proposed portable instrument. As this device would be implemented on a submarine it would

also be interesting to investigate what effects noise, heat and vibration would have on the reconstructed images further. The vibration tests carried out at Bae Systems show that the preamplifier is effected by vibration, it would be interesting to run these tests again to see if these effects are seen using an ASIC with CZT.

Bibliography

[1] STFC, Gamma-kev: Imaging the invisible, *pipss* proposal, 2008.

[2] Y. Yang, Y. Gono, S. Motomura, S. Enomoto, and Y. Yano, Nuclear Science, IEEE Transactions on **48**, 656 (2001).

[3] G. F. Knoll, *Radiation detection and measurement* (Wiley, New York, 1999).

[4] A. H. Compton, Phys. Rev. **21**, 483 (1923).

[5] G. Gilmore and J. Hemingway, *Practical Gamma Ray Spectrometry* (Wiley, New York, 2002).

[6] Radiation detection and measurements: Ix.scintillator detectors, http://inst.nuc.berkeley.edu/NE104/Lectures/Scintillation-DetectorsNE104Spring10.pdf.

[7] S. Sze, *Semiconductor Devices: Physics and Technology* (Wiley, New York, 2002).

[8] G. Ottaviani, C. Canali, and A. A. Quaranta, Nuclear Science, IEEE Transactions on **22**, 192 (1975).

[9] G. Lutz, *Semiconductor radiation detectors : device physics* (Berlin, Springer, 1999).

[10] L. Harkness, *A Design Study of the Semiconductor Sensor Head for the ProSPECTus Compton Camera*, PhD thesis, University of Liverpool, Oliver Lodge Laboratory,University of Liverpool,L69 7ZE, 2010.

[11] T. W. Raudorf and R. H. Pehl, Nuclear Instruments and Methods in Physics Research Section A: Accelerators, Spectrometers, Detectors and Associated Equipment **255**, 538 (1987).

[12] C. J. Solomon and R. J. Ott, Nuclear Instruments and Methods in Physics Research Section A: Accelerators, Spectrometers, Detectors and Associated Equipment **273**, 787 (1988).

[13] K. Pinkau and Z. Naturforsch, The measurement of solar and atmospheric neutrons, 1966.

[14] M. Wernick and J. Aarsvold, *The Fundamentals of PET and SPECT*Emission Tomography (Elsevier, 2004), chap. 19.

[15] P. Z. Klaus, Gamma-ray imaging spectrometry, Science and Technology Review, 1995.

[16] G. W. Phillips, Nuclear Instruments and Methods in Physics Research Section B: Beam Interactions with Materials and Atoms **99**, 674 (1995), Application of Accelerators in Research and Industry '94.

[17] J. Gillam *et al.*, Compton imaging using the smartpet detectors, in *Nuclear Science Symposium Conference Record, 2008. NSS '08. IEEE*, pp. 624 –628, 2008.

[18] L. Mihailescu, K. Vetter, M. Burks, E. Hull, and W. Craig, Nuclear Instruments and Methods in Physics Research Section A: Accelerators, Spectrometers, Detectors and Associated Equipment **570**, 89 (2007).

[19] C. Ordonez, Dependence of angular uncertainties on the energy resolution of compton cameras, in *Nuclear Science Symposium, 1997*, pp. 1122 – 1125, Dept. of Med. Phys., Rush-Presbyterian-St. Lukes Med. Center, Chicago, IL, 1997, IEEE.

[20] S. Webb, *The Physics of Medical Imaging* (Taylor and Francis, 1988).

[21] Y. Fukazawa *et al.*, Nuclear Instruments and Methods in Physics Research Section A: Accelerators, Spectrometers, Detectors and Associated Equipment **541**, 342 (2005), Development and Application of Semiconductor Tracking Detectors,Proceedings of the 5th International Symposium on Development and Application of Semiconductor Tracking Detectors (STD 5),Development and Application of Semiconductor Tracking Detectors.

[22] T. Schulman, *Si, CdTe and CdZnTe radiation detectors for imaging applications*, PhD thesis, University of Helsinki, ethesis.helsinki.fi/julkaisut/mat/fysik/vk/schulman/sicdtean.pdf, 2006.

[23] O. Limousin, Nuclear Instruments and Methods in Physics Research Section A: Accelerators, Spectrometers, Detectors and Associated Equipment **504**, 24 (2003), Proceedings of the 3rd International Conference on New Developments in Photodetection.

[24] S. Watanabe *et al.*, Nuclear Instruments and Methods in Physics Research Section A: Accelerators, Spectrometers, Detectors and Associated Equipment **567**, 150 (2006), Proceedings of the 4th International Conference on New Developments in Photodetection,BEAUNE 2005,Fourth International Conference on New Developments in Photodetection.

[25] T. Takahashi and S. Watanabe, Nuclear Science, IEEE Transactions on **48**, 950 (2001).

[26] T. Tanaka *et al.*, (2004), astro-ph/0410058.

[27] N. Clinthorne, Method for improving the spatial resolution of a compton camera, US patent 6323492, 2001.

[28] S. S. Gambhir and S. S. Yaghoubi, *Molecular Imaging with Reporter Genes* (Cambridge University Press, 2010).

[29] S. Wilderman, W. Rogers, G. Knoll, and J. Engdahl, Fast algorithm for list mode back-projection of compton scatter camera data, in *IEEE Transactions on Nuclear Science*, pp. 957 – 962, Dept. of Nucl. Eng., Michigan Univ., Ann Arbor, MI, 1998, IEEE.

[30] D. Judson, C++ analytical image reconstruction algorithm, 2011.

[31] M.J.Berger *et al.*, Nist standard reference database 8 (xgam), http://www.nist.gov/pml/data/xcom/index.cfm, 1998.

[32] G. Yang *et al.*, Journal of Electronic Materials **38**, 1563 (2009), 10.1007/s11664-009-0799-y.

[33] Andre,R., Bodin, C., Cibert, J., Dang, L. S., and Feuillet, G., Le Journal de Physique IV **03**, C5 (1993).

[34] D. Judson *et al.*, Nuclear Instruments and Methods in Physics Research Section A: Accelerators, Spectrometers, Detectors and Associated Equipment **652**, 587 (2011).

[35] P. Seller, A. Hardie, L. Jones, A. Boston, and S. Rigby, Nucam: a 128 channel integrated circuit with pulse-height and rise-time measurement on each channel including on-chip 12bit adc for high-z x-ray detectors, in *Nuclear Science Symposium Conference Record, 2006. IEEE*, volume 6, pp. 3786 –3789, 2006.

[36] A. Boston *et al.*, Nuclear Instruments and Methods in Physics Research Section A: Accelerators, Spectrometers, Detectors and Associated Equipment **604**, 48 (2009), PSD8, Proceedings of the 8th International Conference on Position Sensitive Detectors.

[37] A. Georgiev, W. Gast, and R. Lieder, Nuclear Science, IEEE Transactions on **41**, 1116 (1994).

[38] H. Spieler, *Semiconductor Detector Systems* (Oxford University Press, Oxford, 2005).

[39] D. Doering, Gretina digitizer specification, 2006, Rev. 1.7, GRETINA Report No. GRT-3-060815-60820.

[40] V. T. Jordanov and G. F. Knoll, Nuclear Instruments and Methods in Physics Research Section A: Accelerators, Spectrometers, Detectors and Associated Equipment **345**, 337 (1994).

[41] D. Radford, Radware, http://radware.phy.ornl.gov/.

[42] K. Vetter *et al.*, Nuclear Instruments and Methods in Physics Research Section A: Accelerators, Spectrometers, Detectors and Associated Equipment **452**, 223 (2000).

[43] E. Gatti, A. Geraci, G. Casati, S. Riboldi, and G. Ripamonti, Nuclear Instruments and Methods in Physics Research Section A: Accelerators, Spectrometers, Detectors and Associated Equipment **458**, 738 (2001).

[44] M. Descovich *et al.*, Nuclear Instruments and Methods in Physics Research Section A: Accelerators, Spectrometers, Detectors and Associated Equipment **553**, 512 (2005).

[45] L. Nelson, *The Spatial Resolution Achievable with Parametric Pulse Shape Analysis of AGATA Detectors and its Application to In-beam Data*, PhD thesis, University of Liverpool, Oliver Lodge Laboratory,University of Liverpool,L69 7ZE, 2008.

[46] F. Crespi *et al.*, Nuclear Instruments and Methods in Physics Research Section A: Accelerators, Spectrometers, Detectors and Associated Equipment **620**, 299 (2010).

[47] P. Twin *et al.*, Il Nuovo Cimento A (1971-1996) **81**, 219 (1984), 10.1007/BF02724166.

[48] G. Turk, *The characterisation of the first SmartPET HPGe planar detector*, PhD thesis, The University of Liverpool, 2006.

[49] http://npg.dl.ac.uk/MIDAS/.

[50] S. Agostinelli *et al.*, Nuclear Instruments and Methods in Physics Research Section A: Accelerators, Spectrometers, Detectors and Associated Equipment **506**, 250 (2003).

[51] E. Farnea, A monte carlo code for agata based on geant4, http://agata.pd.infn.it/documents/glp5152003/EnricoFarnea.pdf.

[52] http://root.cern.ch/drupal.